COUPLING PIEZOELECTRICS FOR HUMAN-SCALE ENERGY SCAVENGING & INTEGRATION OF MEMS ACCELEROMETERS IN FLEXIBLE ELECTRONICS

A Dissertation
Presented to
The Academic Faculty

By

Euiyoung Park

In Partial Fulfillment
of the Requirements for the Degree
Master of Science in the
School of Mechanical Engineering

Georgia Institute of Technology

December 2017

Copyright © Euiyoung Park 2017

COUPLING PIEZOELECTRICS FOR HUMAN-SCALE ENERGY SCAVENGING & INTEGRATION OF MEMS ACCELEROMETERS IN FLEXIBLE ELECTRONICS

Approved by:

Dr. Bassiri-Gharb, Advisor
School of Mechanical Engineering
Georgia Institute of Technology

Dr. Zimmermann, Advisor
Institute for Microintegration
University of Stuttgart

Dr. Stern, Co-advisor
ATAS Energy and Sustainability Lab
Georgia Tech Research Institute

Dr. Curcic
Max Planck Institute for Intelligent Systems
University of Stuttgart

Date Approved: September 8, 2017

To my family.

ACKNOWLEDGEMENTS

This thesis would not have been possible without the numerous people I've had the pleasure and honor of working with these past two years, both in Atlanta and Germany.

I would like to express my gratitude to Dr. Nazanin Bassiri-Gharb for her mentorship, providing valuable and constructive suggestions during my time at Georgia Tech. My grateful thanks are also extended to Dr. Ilan Stern for his guidance and support, as well as the opportunities provided by the institute to present my work in a conference.

I would also like to offer my special thanks to Dr. André Zimmermann for his constructive input into the project and advice given throughout my year in Stuttgart. I am particularly grateful for the assistance of Cristian Nagel at Bosch, whose insight and knowledge in the project provided me with guidance and encouragement.

My thanks are extended to Dr. Paul Neitzel from Georgia Tech and Dr. Oliver Sawodny from University of Stuttgart for overseeing the joint degree program and making this opportunity a possibility for us. I would also like to express my appreciation to Florian Morlock for resolving any issues we encountered during our time in Germany.

And finally, I would like to thank my family and friends for their unwavering support and motivation. A special thanks to the fellow students at Bosch, especially Thomas, Ben, Kain and Simon, and Hawmies in Atlanta, Caroline, Marius, Thomas, Xiaoshu, Ahmed and Chris, for making the past two years an unforgettable experience.

TABLE OF CONTENTS

LIST OF TABLES

LIST OF FIGURES

SUMMARY

This thesis is presented in two parts: the first project, titled ”Coupling Piezoelectrics for Human-Scale Energy Scavenging”, is completed at the Georgia Institute of Technology and explores the possibility of converting waste energy from human footsteps into usable energy. Mechanical energy exists almost everywhere there is movement–vibrations in bridges, wind spinning turbines and human steps onto the floor–and the direct piezoelectric effect inherent in piezoelectric materials converts the mechanical energy into electrical energy. Piezoelectricity can be advantageous in certain applications due to its chemical stability, scalability, and low dependence on environmental conditions. Two distinct excitation methods for energy harvesting optimization are discussed. First, a compressive system is studied through finite element analysis and experimentally with the goal of simulating human footfall. The second utilizes a plucking motion to couple high resonant frequencies inherent in piezoelectrics to low human scale frequencies.

The second project, titled ”Integration of MEMS Accelerometers in Flexible Electronics”, is conducted at Robert Bosch GmbH in Renningen, Germany, under the department of Microsystems and Nanotechnologies (CR/ARY). All figures and values are represented in arbitrary units due to the confidential nature of the project. The project aims to integrate silicon sensors into flexible electronics, as the field of electronics continues to grow, but a concrete integration and packaging method for flexible sensor technology is yet to exist. Advanced interconnect materials are studied as a method to mitigate stress concentration at interconnect level and allow for chip integration onto flexible boards. Embedding of thinned accelerometer structures into flexible molds is also explored, from designing of the system to optimization of manufacturing process through finite element analysis and experimental methods. Sensor performance of each system is measured to study the influence of mechanical stress through bending and thermal stress through manufacturing onto the MEMS core structure.

Part I

Coupling Piezoelectrics for Human-Scale Energy Scavenging

CHAPTER 1
INTRODUCTION

During the last century, the demand for energy has risen tremendously due to industrial development and population growth and only continues to rise. To meet the demand, there has been an increasing attention and research in the field of renewable energy. Existing renewable energy sources range from hydro, geothermal, solar, wind to tidal waves, accounting for about 20 % global energy generation [1]. Kinetic energy generators convert energy in the form of mechanical movement present in the application environment into electrical energy, typically through electromagnetic, piezoelectric, electrostatic, or magnetostrictive mechanisms [2]. Energy scavenging utilizes these mechanisms to convert ambient energy to power small electronic devices. For low-power applications, piezoelectric transducers are often utilized through direct and vibrational excitation.

1.1 Motivation and Objectives

The direct piezoelectric effect inherent in piezoelectric materials has the ability to convert mechanical energy, which exists almost everywhere there is movement, into electrical energy. The kinetic energy that is applied to the ground when a person steps onto it can be scavenged by converting the part of the kinetic energy that is linked to the normal force into usable electric energy through the self-generating and reversible nature of piezoelectric materials. By installing tiles with affixed piezoelectric units in areas of high foot traffic, such as stadiums, airports and hospitals, the system is able to transform energy from everyday walking into usable electricity that would otherwise be wasted.

Expanding from the scope of energy harvesting, utilization of piezoelectric materials in floor tiles hold the possibility for many applications. A self-powered occupancy sensor to achieve the concept of the smart building, or a building that is aware of occupancy

and power consumption, allows for reducing the overall power draw of the buildings [3]. Hospitals can use the tiles as a method to track accidental falls of patients from beds through signal generation from the impacts. It also allows for interactive systems in amusement parks or museums, where the guests can interact with their surroundings that respond to their footsteps [4].

The three basic vibration-to-electric energy conversion mechanisms are electromagnetic, electrostatic and piezoelectric transduction [5]. Compared to the other two mechanisms, the main advantages of piezoelectric materials in energy harvesting are their large power densities and ease of application [6]. As it can be observed in fig. 1.1, piezoelectric energy harvesting covers the largest area in the graph, with power density comparable to those of thin-film and thick-film lithium-ion batteries and thermoelectric generators. Due to this, piezoelectricity has received a great amount of attention in the field. The voltage output in piezoelectric materials emerges from the constitutive behavior of the material, eliminating the need for an external voltage input. It can also be fabricated in both macro-scale and micro-scale due to its well-established thick-film and thin-film fabrication techniques [7].

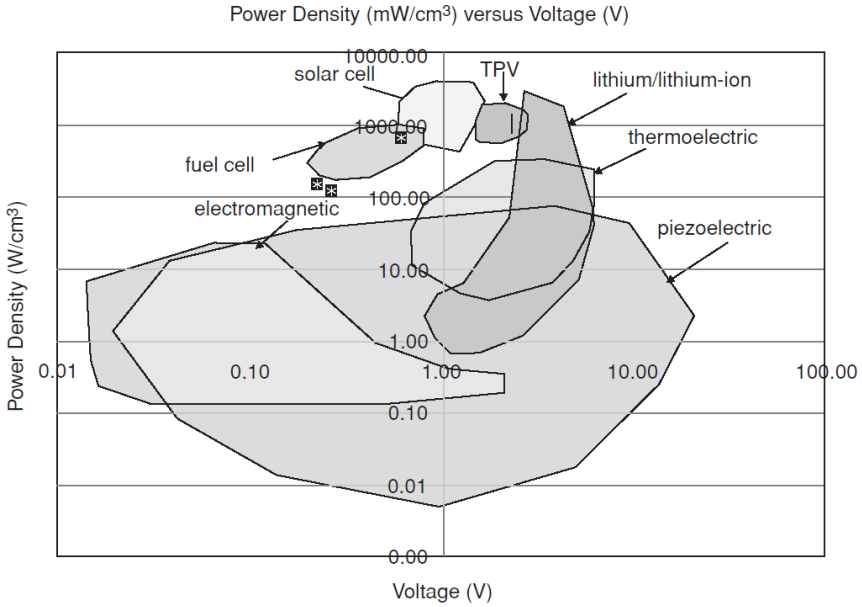

Figure 1.1: Power density and voltage comparison of energy generation mechanisms [6]

CHAPTER 2
THEORETICAL BACKGROUND

2.1 Fundamentals of Piezoelectricity

Piezoelectric effect can be classified into two types: (1) direct effect and (2) converse effect. Discovered by Pierre and Jacques Curie in 1880, the direct piezoelectric effect describes the electric polarization of a piezoelectric material when a mechanical strain is applied to it [6]. The inverse behavior, deduced mathematically from the fundamental principles of thermodynamics by Lippmann in 1881 [8] and confirmed experimentally by the Curie brothers, is the converse piezoelectric effect where the material becomes strained by the amount proportional to the polarizing field. In the same year, the term ”piezoelectricity” was coined by Henkel.

In discussing piezoelectricity, the topic of ferroelectricity and pyroelectricity cannot be avoided, due to their inter-relationships in terms of crystal structures. All crystals can be categorized into 32 different classes, determined by symmetry elements including center of symmetry, axis of rotation, mirror planes and combinations of them. In order to achieve piezoelectric effect, the material composition must be noncentrosymmetric and 21 classes out of the 32 point groups satisfy this condition. 20 of those groups are piezoelectric, and out of the 20 piezoelectric classes, 10 are pyroelectric [1].

Compared to the general piezoelectric polarization, the pyroelectric polarization is kept as permanent dipoles in the structures. The term pyroelectricity derives from the fact that the polarization varies with temperature. A subgroup within pyroelectricity is ferroelectricity, which has spontaneous polarization [9]. The polarization of the materials that belong to this group can be reversed by an external applied electric field, provided that the applied field is lower than the dielectric breakdown of the materials.

2.2 Material Composition

It was discovered in the first half of the last century that several natural crystals, such as Rochelle salt and quartz, exhibit piezoelectric effect [10]. In the second half, piezoelectric ceramics were developed to produce materials with larger electromechanical coupling compared to natural crystals. Until the discovery of barium titanate and lead zirconate titanate (PZT) in the 1940s and 1950s respectively, limited performance by piezoelectric materials inhibited commercialization [11]. PZT was developed at the Tokyo Institute of Technology and exhibited very high dielectric and piezoelectric properties. Various versions of it are the most commonly used piezoceramics to this date [12]. Several Japanese companies began developing new processes and applications in 1965, enabling a new market for piezoelectric devices [11].

PZT is the material of interest in our application. The material can be formed into polycrystalline form by being prepared into a fine powder and formed into any required shape. It is a solid solution of two oxides: (1) an antiferroelectric lead zirconante and (2) a ferroelectric lead titanate. The unit cell is a perovskite (ABO_3) as shown in fig. 2.1, with lead atoms at the corner, oxygen atoms at the face centers and Zr or Ti atoms at the body center. Above the Curie temperature, the structure is cubic and symmetric, but all compositions of the solid solution above 5% of lead zirconate is ferroelectric under the Curie temperature [13].

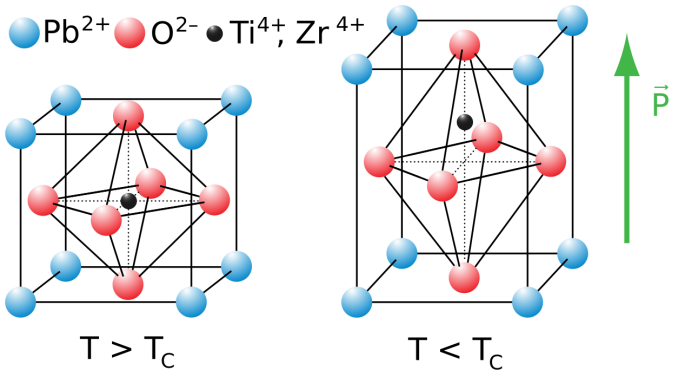

Figure 2.1: Crystal structure of PZT under and above the Curie temperature

In a ferroelectric composition, the displacement of the central ions is the reason for the reversibility of polarization. With the homogeneous areas of the material with the same polarization orientations being referred to as domains, the as-prepared piezoelectric ceramics have no piezoelectric effect due to the random orientation of the domains and resulting zero net polarization. Therefore, the polycrystalline piezoceramics must be poled at strong external DC electric fields of 10 to kV cm^{-1} [13]. This aligns the orientations of the randomly distributed domains within the grains to allow ferroelectric ceramics to behave like a single crystal with piezoelectric properties. While PZT is polycrystalline, it is poled in a specific direction to stimulate the piezoelectric effect.

2.3 Principle of Piezoelectric Effect

Piezoelectric materials produce electric charges when subjected to external mechanical loads. Variations of the stress and strain applied to the materials enable conversion from mechanical to electric energy, generating an alternating electric charge [14]. As observed in fig. 2.2, the magnitude and direction of the electrical current are determined by the magnitude and direction of the external mechanical stress and strain.

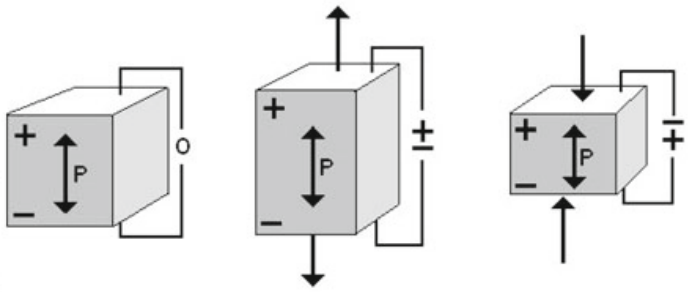

Figure 2.2: Response of piezoelectric ceramic to external mechanical stimulation [1]

Mathematically, the piezoelectric effect is described by the elastic Gibbs function in the case of a sample under isothermal and adiabatic conditions as

$$G_1 = -\frac{1}{2}(S^D_{ijkl}T_{ij}T_{kl} + 2g_{nij}D_nT_{ij}) + \frac{1}{2}\beta^T_{mn}D_mD_n \tag{2.1}$$

where g is the piezoelectric voltage coefficient, or the ratio of open circuit electric field and applied mechanical stress, s is the elastic compliance and β is the inverse permittivity [15]. The independent variables of the equation are the stress T and the electric displacement D. The superscripts of the constants refer to the independent variable held constant when defining the constant, and the subscripts define the orientation of the tensors. The linear equations of piezoelectricity, determined by the derivative of G_1 are

$$S_{ij} = -\frac{\delta G_1}{\delta T_{ij}} = s^D_{ijkl} T_{kl} + g_{nij} D_n \tag{2.2}$$

$$E_m = \frac{\delta G_1}{\delta D_m} = \beta^T_{mn} D_n - g_{nij} T_{ij} \tag{2.3}$$

where S and T are strain and stress tensors, respectively, and E is the electric field vector. The equations can be further simplified to a reduced form by noting the redundancy in the strain and stress variables. The constants of importance are dependent on the vibration modes of the elements. The different piezoelectric structures that are commonly utilized for the varying vibration modes are shown in fig. 2.3.

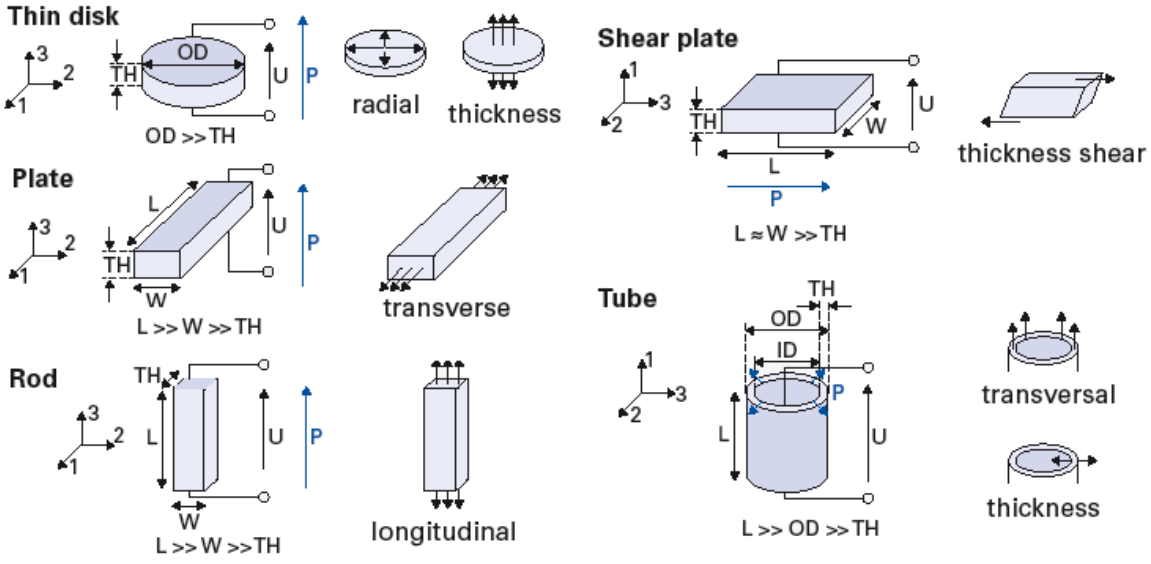

Figure 2.3: Vibration modes of piezoelectric elements [16]

2.4 Resonance of Piezoelectric Materials

Any body of mass has certain frequencies at which it prefers to resonate and the same holds true for piezoelectric materials. In the analysis of piezoelectric materials, the impedance of free piezoelectric vibrators can be modeled as lumped circuit models to predict the electrical behavior of the resonator. Fig. 2.4(a) shows the Van Dyke circuit model that represents the equivalent circuit of a piezoelectric vibrator at resonance. However, representing the losses of a capacitor or inductor by adding a frequency independent resistor in parallel is less general than representing the losses by the use of complex circuit components, as shown in fig. 2.4(b). C_0 in the circuit is the inherent static capacitance between the input and output electrodes, and due to the parasitic capacitance C_0, piezoelectric resonators have the frequency response as shown in fig. 2.5. [15]

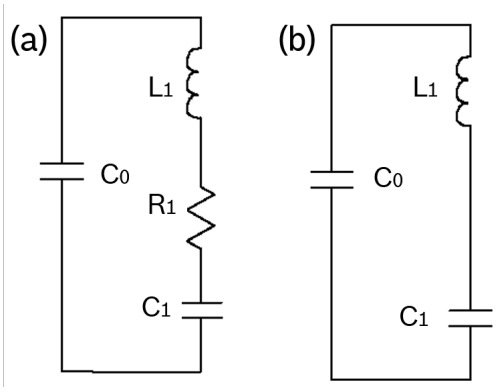

Figure 2.4: (a) Butterworth Van-Dyke resonator circuit [17] (b) Complex circuit with 3 complex parameters [15]

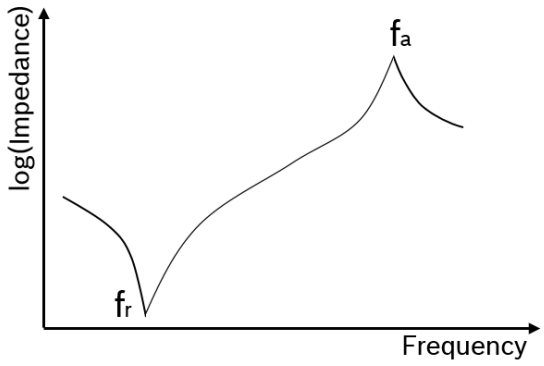

Figure 2.5: Frequency response of impedance of a piezoelectric element [18]

The resonant frequency, or series resonance, is reached when a short circuit between C_1 and L_1 is realized. This occurs when $X_{L1} = X_{C1}$, as the two reactances cancel each other out as they are opposite and equal to each other and the voltages representing V_{L1} and V_{C1} must also be opposite and equal, resulting in a zero voltage drop.

$$2\pi f L_1 = \frac{1}{2\pi f C_1} \tag{2.4}$$

$$f_r = \frac{1}{\sqrt{L_1 C_1}} \tag{2.5}$$

The anti-resonant frequency, also known as parallel resonance, is reached when the the reactances of the parallel LC circuit are equal to each other, resulting in an equal and opposite current in each branch. This leads to a zero reactive current, or an open circuit. The anti-resonant frequency is defined as

$$f_a = \frac{1}{\sqrt{L_1 \frac{C_1 C_0}{C_1 + C_0}}} \tag{2.6}$$

Utilizing the resonant and anti-resonant frequencies, effective electromechanical coupling factor k_{eff} and mechanical quality factor Q_M are defined as

$$k_{eff} = \sqrt{1 - (f_r/f_a)^2} \tag{2.7}$$

$$Q_M = 2\pi \frac{E_{stored}/cycle}{E_{dissipated}/cycle} \tag{2.8}$$

where f_r is the resonant frequency and f_a is the anti-resonant frequency [1, 19]. The coupling factor, k_{eff}, is often utilized to assess piezoelectric materials' transduction efficiency, and is defined as the ratio of the effective stored electrical energy to the total input mechanical energy. The mechanical quality factor, Q_M, which is the inverse of the mechanical loss, tan φ' is the amplification factor of vibration of a piezoresonator in resonance conditions. The high mechanical quality factor in PZT is achieved by acceptor doping the system, thereby generating internal field which suppresses domain wall motion. This is the main cause of mechanical loss in piezolelectric materials. [20]

The maximum efficiency of the piezoelectric devices can be estimated utilizing:

$$\eta = \frac{\frac{1}{2}\left(\frac{k^2}{1-k^2}\right)}{\frac{1}{Q_M} + \frac{1}{2}\left(\frac{k^2}{1-k^2}\right)} \tag{2.9}$$

This indicates that the efficiency can be increased by choosing materials with high k and Q_M properties, which are inherent to the material type [1].

Considering a piezoelectric material in the form of a disk with two electrodes plates on the two opposite sides, the material behaves as a dielectric medium. At frequencies far below resonance, piezoelectric materials are essentially capacitors. In general, a pair of electrodes separated by a dielectric material is a capacitor and piezoelectric devices behave much like a capacitor. The coefficient ϵ_r of a piezoelectric material is the ratio of the capacitance of the piezoelectric material, compared with the capacitance of a pair of plates of the same area and gap using vacuum as the dielectric material. The capacitance of piezoelectric materials increases with temperature and decreases with stress on the ceramic.

Accordingly, the sensor may be represented as a charge source q_s with a capacitance C_s in parallel, as shown in fig. 2.6. [21]

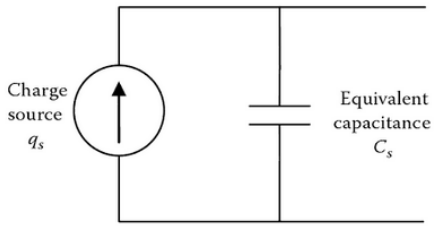

Figure 2.6: Vibration modes of piezoelectric elements [21]

The internal resistance in the piezoelectric elements between the electrodes, may be represented in series with the charge source, but will have no effect on the charge source (as it is in series) and is omitted, or considered as internal to the charge source. This circuit also omits the very high insulating resistance of the element in parallel with the charge source. The impedance from the capacitor is given by

$$Z_s = \frac{1}{j\omega C_s} \tag{2.10}$$

It is clear from eq. 2.10 that the impedance of a piezoelectric material can be particularly high at low frequencies. This is one of the limitations of piezoelectric materials at lower frequency, where the charge leakage cannot be neglected. In the charge source q_s of this circuit, the mechanical dynamics is hidden. The electromechanical equivalent circuit for inertial-based piezoelectric energy harvesters, with the mechanical model represented in an electrical equivalent model by representing the mechanical force as an electrical voltage and a mechanical velocity replaced by an electric current, is shown in fig. 2.7. The mass is modeled by an inductor with inductance $L_m = m$, the stiffness represented by a capacitor with capacitance $C_m = 1/k$, and the parasitic damping modeled by a resistor with resistance $R_m = d$. C_p denotes the piezoelectric output capacitance and Γ represents the generalized electromechanical coupling factor (GEMC), which depends on the geometry.

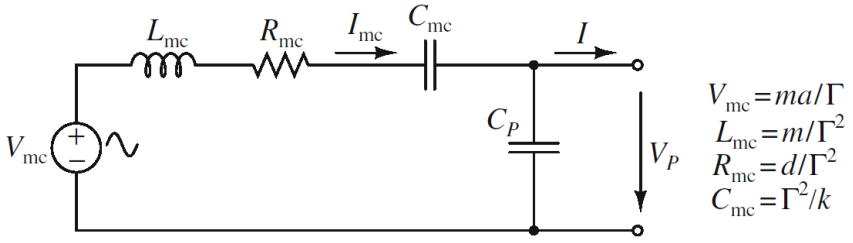

Figure 2.7: Electromechanical equivalent circuit of piezoelectric energy harvester [22]

The maximum power is extracted from a piezoelectric material if it is terminated by a load impedance equal to its conjugate complex impedance. Fig. 2.8 shows the equivalent circuit for the piezoelectric model with its conjugate complex load. The conjugate complex pair $C_p - \overline{L_p}$ represents an infinitely high impedance and the other pairs $C - \overline{L}$ and $L - \overline{C}$ create a zero impedance if the values of the load impedance components are set as follows:

$$\overline{L_p} = \frac{1}{\omega^2 C_p} \tag{2.11}$$

$$\overline{L}_{mc} = \frac{1}{\omega^2 C_{mc}} \tag{2.12}$$

$$\overline{C}_{mc} = \frac{1}{\omega^2 L_{mc}} \tag{2.13}$$

This results in the simplified circuit shown in fig. 2.9, which is a simple voltage divider. The maximum power dissipated at the load resistor occurs when the two resistors are equal.

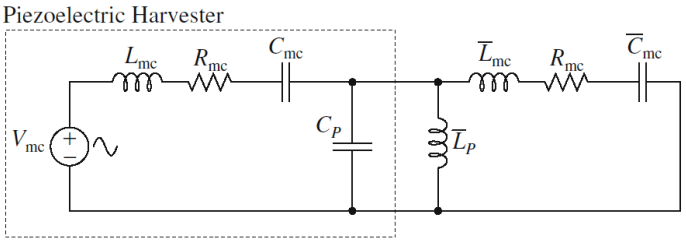

Figure 2.8: Piezoelectric model with impedance load [22]

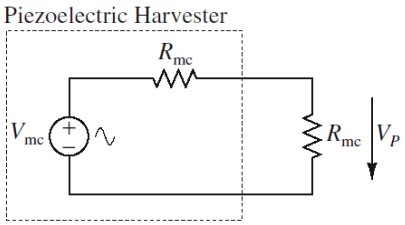

Figure 2.9: Simplified piezoelectric model [22]

CHAPTER 3

CURRENT DEVELOPMENT

3.1 Piezoelectric Structures

Most piezoelectric energy harvesters are in the form of cantilevered beams with one or two piezoelectric layers, located on a vibrating host structure. The dynamic strain induced in the piezoceramic layers by the vibrational excitation results in an alternating voltage output across their electrodes [6].

In an effort to reduce power consumption in structures under vibration and buildings with large foot traffic, the development of piezoelectric tiles has been widely studied. A typical design on a vibrating host structure is a cantilevered beam with piezoceramic layers, as seen in fig. 3.1. When a harmonic base motion is applied to the structure, an alternating voltage output is produced. This type of structure is favored because it allows for a more compliant structure than a stack-type device, especially for piezoelectric ceramics where the stiffness and matching the mechanical impedance of the transducer with the rest of the system is an issue [23].

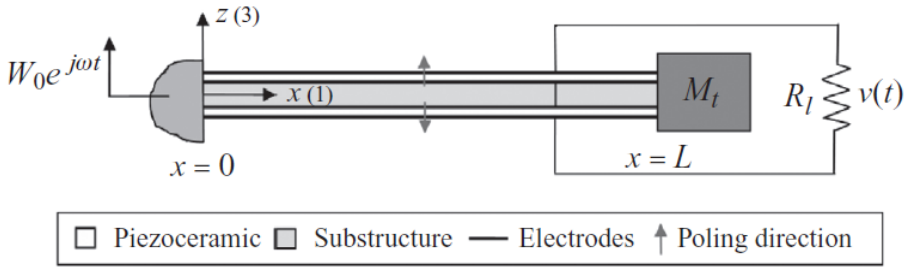

Figure 3.1: Cantilevered beam with piezoceramic layers [1]

While beam structures are preferred for low stress levels, ceramic-metal composites are utilized for high stress levels. These structures are generally designed with a metal faceplate that couples to both the ceramic and the surrounding medium to transfer the incident stress

to the ceramic or the displacement to the medium [1]. As shown in fig. 3.2, the Moonie utilizes moon-shaped spaces between the metal end caps and the piezoelectric ceramic to magnify the displacement in the piezoceramic [24]. The cymbal consists of a poled piezoelectric disk, sandwiched between two metal end caps with a truncated cone-shaped cavity [1]. Rainbow utilizes a curved surface, resulting in higher charge under a given stress level [25].

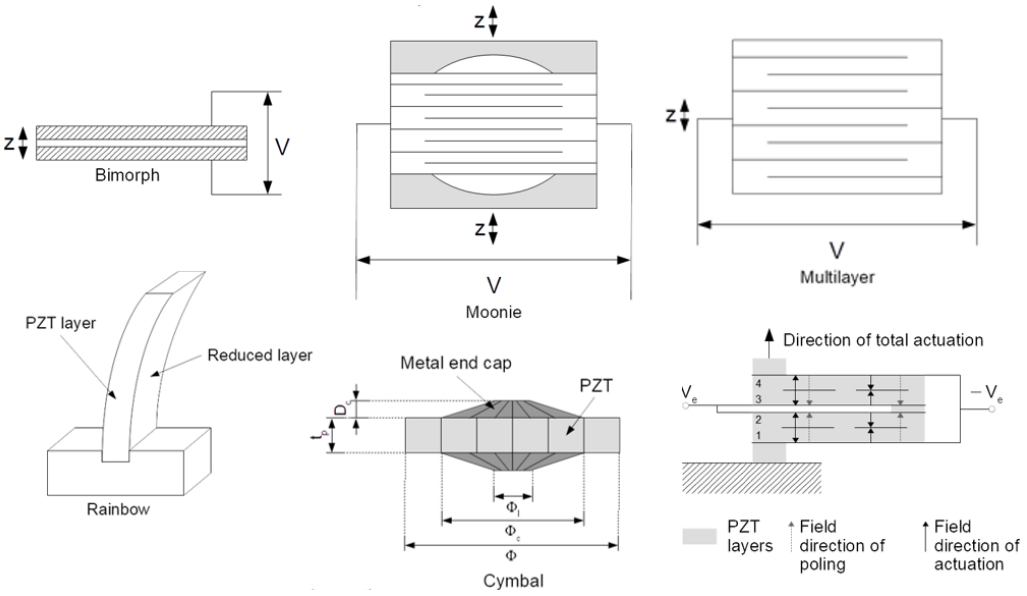

Figure 3.2: Piezoelectric structures commonly found in transducers

3.2 Human Activity Energy Scavenging

Piezoelectric harvesters mounted in shoes to convert mechanical energy from human walking or running to electrical energy have been extensively studied [26, 27, 28]. Methods of harnessing energy through a flexible polyvinylidene fluoride (PVDF) bimorph mounted under the insole and curved, pre-stressed spring metal strips laminated with a semiflexible form of PZT under the heel are explored. They have been used to power a radio frequency (RF) tag system to demonstrate the possibility of self-powering applications to enable a smart environment without the use of batteries. The most promising design for harvesting energy from foot traffic thus far is the use of cymbals that mechanically amplify the

stress and strain of piezoelectric materials [29]. While the power output of this set-up is promising, the overarching cost of such system is extremely high, as it requires high-quality piezoelectric materials and an extensive manufacturing process.

The main issue with human energy scavenging with piezoelectric materials stems from frequency mismatch between environment excitation and human motion. An up-conversion of the frequencies such that the piezoelectric elements vibrate at frequencies closer to the resonance even if the external excitation frequency is low was first presented in the form of a piezoelectric monomorph disk impacted by a steel ball falling from a known height [30]. As the ball bounces from the disk, the disk vibrates at its resonant frequency. A design for a heel strike generator, where a system composed of lead screw, gear train and cam produces a controlled sinusoidal deformation of PZT element, has also been proposed [30]. Piezoelectric harvesters that extract energy from human joint motion have also been designed, including knee-joint [31, 23] and elbow-joint [32]. The knee-joint energy harvester as shown in fig. 3.3 works through up-conversion of frequency with PZT bimorphs. The elbow-joint device works due to the bending and release of PVDF.

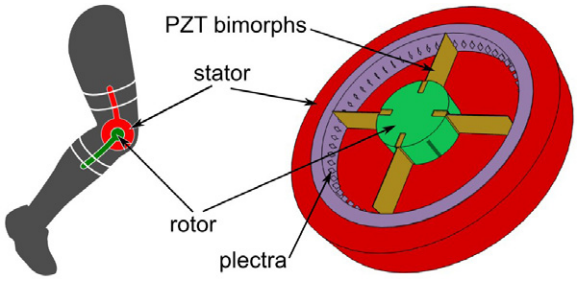

Figure 3.3: Knee-joint piezoelectric harvester [31]

CHAPTER 4
SIMPLE COMPRESSION

This chapter explores the simple compression method of piezoceramic disks, highlighting the effect of decreasing the frequency of excitation below the material resonant frequency of the transducers.

4.1 Finite Element Analysis

To simulate the results and compare between various PZT materials, a finite element analysis program ANSYS (ANSYS Inc., Canonsburg, PA, USA) was utilized in a simplified axisymmetric 2D analysis. Due to its anisotropic nature, it is important to consider the piezoelectric coefficient and elastic stiffness matrices of PZT. The material properties of interest are tabulated below in Tab. 4.1. Out of the five PZT materials, PZT-2, PZT-4 and PZT-8 are hard ceramics, while PZT-5A and PZT-5H are soft. Hard ceramics typically have much higher mechanical quality factors and lower dielectric losses. They also exhibit higher resistance to depolarization under high mechanical stress or electrical excitation [6].

ANSYS requires a specific format to input these coefficients into the program and there are three matrices of importance in a piezoelectric system [33]. The first is a permittivity matrix, ε, which describes the dielectric constants according to the relevant poling direction. The program requires the matrix to be evaluated at constant strain. The mechanical parameters of interest in piezoelectric materials are elastic compliance and stiffness constants which can be input into ANSYS as either the *s* or *c* matrices. Lastly, the piezoelectric coefficients are required in the form of *e*, which relates the polarization to strain. While manufacturers usually provide the *d* coefficients that relate the polarization to stress, but this can be converted to meet the ANSYS standards. Assuming polarization in the y-direction as the thickness, the material property matrices are mapped as shown below.

Table 4.1: Material specifications of generic PZT materials [34]

	Units	**PZT-2**	**PZT-4**	**PZT-5A**	**PZT-5H**	**PZT-8**
$\varepsilon_{33}^S/\varepsilon_0$		260	635	830	1470	600
$\varepsilon_{11}^S/\varepsilon_0$		504	730	916	1700	900
$\mathbf{e}_{31}$	N/m^2	-1.86	-5.20	-5.40	-6.55	-4.11
$\mathbf{e}_{33}$	N/m^2	9.0	15.1	15.8	23.3	14.0
$\mathbf{e}_{15}$	N/m^2	9.8	12.7	12.3	17.0	10.3
$\mathbf{C}_{11}^E$	F/m	13.5e10	13.9e10	12.1e10	12.6e10	14.9e10
$\mathbf{C}_{33}^E$	F/m	11.3e10	11.5e10	11.1e10	11.7e10	13.2e10
$\mathbf{C}_{44}^E$	F/m	2.22e10	2.56e10	2.11e10	2.30e10	3.13e10
$\mathbf{C}_{66}^E$	F/m	3.34e10	3.06e10	2.26e10	2.35e10	3.40e10
$\mathbf{C}_{12}^E$	F/m	6.79e10	7.78e10	7.54e10	7.95e10	8.11e10
$\mathbf{C}_{13}^E$	F/m	6.81e10	7.43e10	7.52e10	8.41e10	8.11e10
ρ	kg/m^3	7600	7500	7750	7500	7600
$\mathbf{Q}_M^*$		680	500	75	65	1000

$$\epsilon = \begin{bmatrix} \epsilon_{11} & 0 & 0 \\ 0 & \epsilon_{33} & 0 \\ 0 & 0 & \epsilon_{11} \end{bmatrix}$$

$$c = \begin{bmatrix} c_{11} & c_{13} & c_{12} & 0 & 0 & 0 \\ c_{13} & c_{33} & c_{13} & 0 & 0 & 0 \\ c_{12} & c_{13} & c_{11} & 0 & 0 & 0 \\ 0 & 0 & 0 & c_{44} & 0 & 0 \\ 0 & 0 & 0 & 0 & c_{44} & 0 \\ 0 & 0 & 0 & 0 & 0 & c_{66} \end{bmatrix}$$

$$e = \begin{bmatrix} 0 & e_{31} & 0 \\ 0 & e_{33} & 0 \\ 0 & e_{31} & 0 \\ e_{15} & 0 & 0 \\ 0 & 0 & e_{15} \\ 0 & 0 & 0 \end{bmatrix}$$

Simple disks of the five different PZT compositions and polarization in the thickness direction were utilized, as shown in fig. 4.1. The disks are of radius 15 mm and thickness 0.15 mm, subjected to 200 kPa pressure on the top side. Each side of the ceramic element is coupled to a common node and the nodes are used as electrodes to be connected to an electrical load. The bottom side is grounded as zero. For a simple compression analysis, where the direction of stress and the direction of polarization is the same, the coefficients in the 33 orientation is of importance.

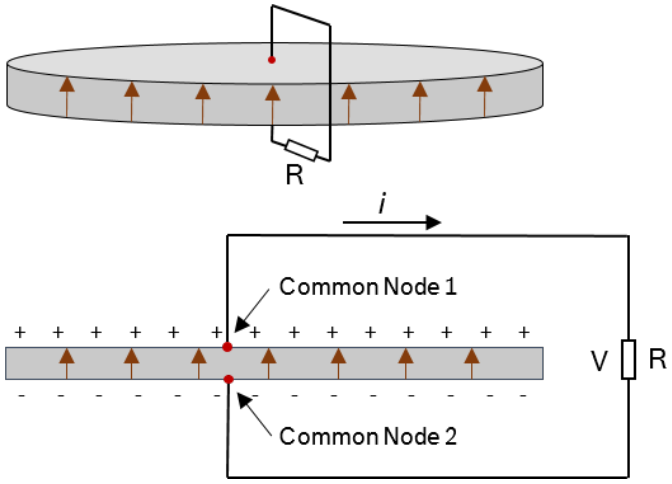

Figure 4.1: Piezoelectric thin disk with polarization in the thickness direction

To determine the resonant frequency of the various PZT materials, modal analysis was performed. The first eigenvalue frequency was found to be as listed in tab. 4.2. This is useful information for the harmonic analysis of the system, where a damping factor β must be accounted for by utilizing the mechanical quality factor, Q_M, and the resonant frequency [31]. In an off-resonance frequency, the amplitude of power output is decreased by a factor proportional to the damping factor [35]. The mechanical loss, C, affects the vibration amplitude and the resulting energy output significantly and it is expressed as:

$$C = \alpha M + \beta K \tag{4.1}$$

where M and K are mass and stiffness matrices, respectively, and α and β are the mass

and stiffness matrix multiplier. The mass damping, which accounts for friction damping, was ignored while the stiffness damping is included utilizing β as [36]:

$$\beta = 1/\omega Q_M \tag{4.2}$$

Table 4.2: Mechanical quality factors [34], resonant frequencies and damping factors of PZT

	PZT-2	**PZT-4**	**PZT-5A**	**PZT-5H**	**PZT-8**
f (kHz)	83.9	88.5	78.3	78.3	88.7
$\mathbf{Q}_M$	680	500	75	65	1000
β	2.79e-9	3.60e-9	2.71e-8	3.13e-8	1.80e-9

Harmonic analysis of PZT was performed to study the effect of varying frequency of excitation and electrical load on power generation. The geometry and material composition as shown above in the modal analysis were applied and the models were subjected to overall pressure of 200 kPa. The root-mean-square power output, P_{rms} of the system is calculated from the voltage amplitude V across the electrical load R as

$$V_{rms} = V/\sqrt{2} \tag{4.3}$$

$$P_{rms} = V_{rms}^2/R = V^2/2R \tag{4.4}$$

In fig. 4.2, it can be observed that at around the resonant frequencies specified above, the output power of the disk is maximum. The resonant frequency, or the frequency where the power reaches maximum, is seen to be increasing as the electrical load increases. This is to be expected as the overall damping of the system increases as the electrical load increases. Comparing the PZT materials under resonant excitation, it can be seen that the hard ceramics exhibit a much higher energy output at resonant frequency at about an order of magnitude higher than that of soft ceramics. The resonant power output is proportional to the mechanical quality factor for resonant application.

However, at low frequency and off-resonant application as expected in human footsteps, soft ceramics display a higher power output. While soft ceramics have lower mechanical quality factors, they are more mechanically compliant and possess higher piezoelectric strain constants. Moreover, a higher mechanical quality factor translates to a narrow bandwidth in the electromechanical spectrum, resulting in a sharp drop in voltage output at an off-resonance frequency [36].

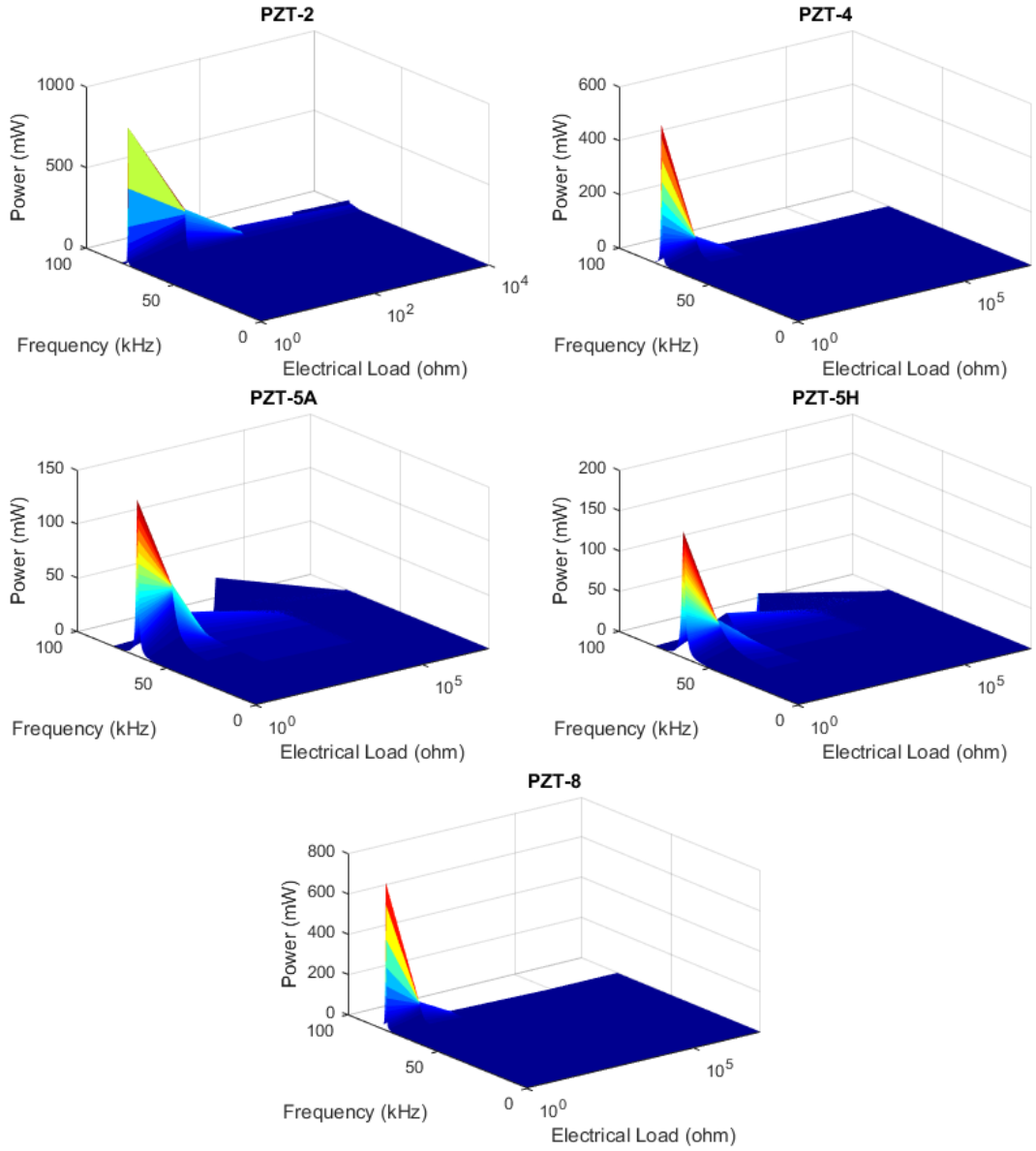

Figure 4.2: Harmonic analysis results of simple compression of PZT

The effect of lowering the frequency of excitation can also be seen here. The power output at lower frequency is much lower than that at around the resonant frequency. As it can be seen for PZT-5A thin disk, the output power is about 0.003 mW at 80 Hz and 10 kΩ of resistance, which is only about 0.02 % of the power generated with the same resistance at the resonant frequency. The efficiency of utilizing this material decreases considerably when the frequency is lower than that of the resonant frequency.

Closing in on the lower frequency range of 0 to 10 Hz for the PZT-5H element as shown in fig. 4.3, it can be seen that the matching impedance load increases due to the higher overall damping of the system.

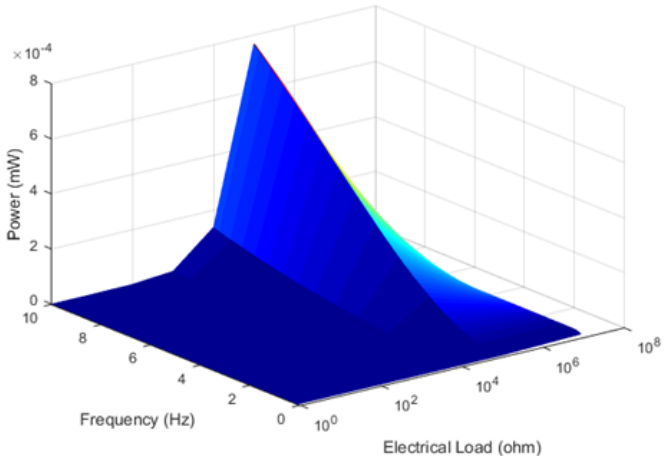

Figure 4.3: Harmonic analysis of PZT-5H thin disk at low frequency

4.1.1 Geometry Comparison

Fig. 4.4 is a comparison of varying the geometry of the PZT-5A disks with the aspect ratio of the radius and thickness varying from 1 to 100. As the thickness is increased by a factor of 10, the power output of is increased by the same factor. This is to be expected as this is a simple compressive force applied on the disk, and therefore a higher thickness will result in a higher energy generation within the material. This is at a low-frequency range and the energy output is higher as frequency increases. It can be observed that the matching impedance load increases along with the thickness, due to higher overall damping.

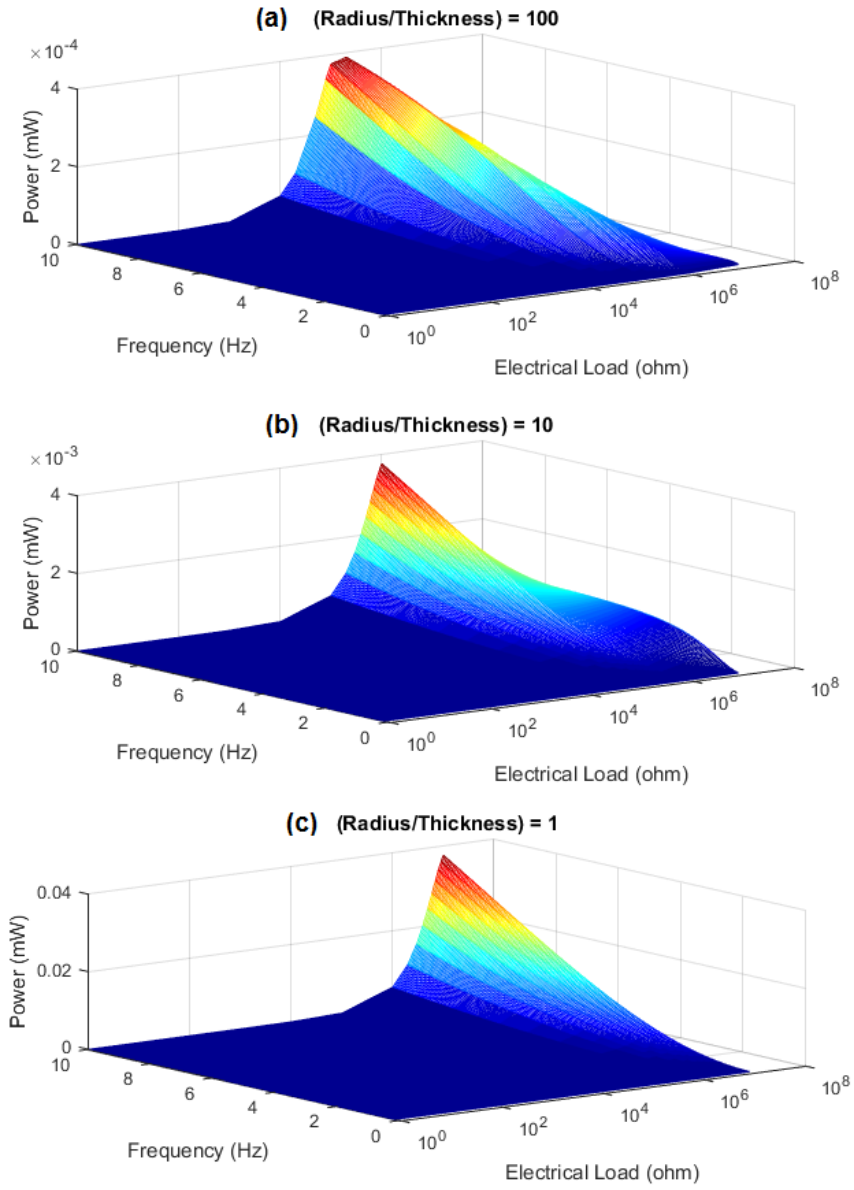

Figure 4.4: Geometry comparison of PZT-5A disks (a) (Radius/Thickness) = 100 (b) (Radius/Thickness) = 10 (c) (Radius/Thickness) = 1

4.1.2 Spatial Analysis

To determine the optimal location of the piezoelectric elements affixed under a stepping tile, the electrical and mechanical output of the elements were simulated with varying location of the stepping force onto the tile as shown in fig. 4.5. Piezoceramic disks were placed between stepping tile and solid surface in a 2D approximated simulation. Utilizing the

symmetric nature of the design only half of the system is modeled. While the system is symmetric in quarters in terms of geometry the force is only applied on one side of the system–in which case the quarter symmetry is no longer fulfilled.

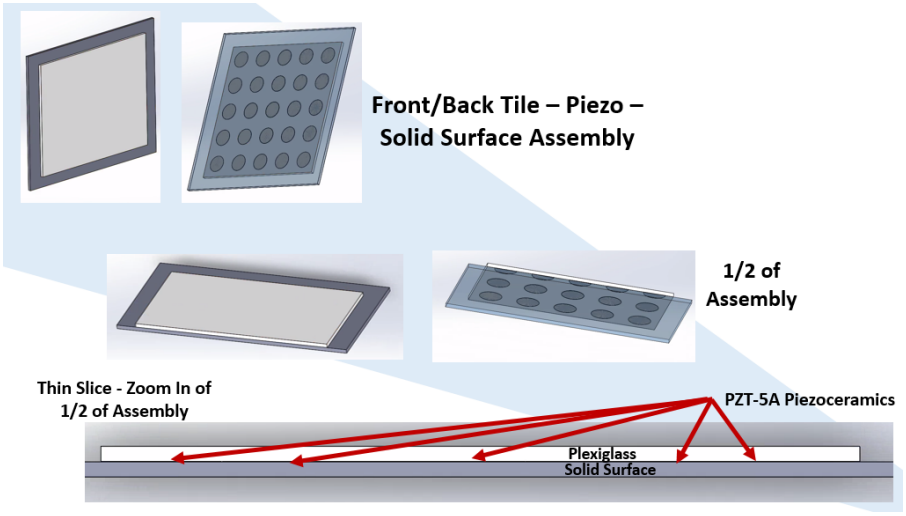

Figure 4.5: Configuration of 2D simulated piezoelectric elements under stepping tile

The 2D piezoelectric assembly modeled for analysis in ANSYS is composed of 3 main parts: (1) the piezoelectric unit, (2) the stepping tile, and (3) the concrete slab. The piezoelectric unit is comprised of one type of material: one circular layer of PZT-5A piezoceramic poled in the thickness direction with a radius of 14.8 mm and thickness of 0.15 mm. The stepping tile is a 5 mm thick square (500 mm x 500 mm) piece of plexiglass. The concrete is a 10 mm thick square slab (600 mm x 600 mm). The piezoceramics consist of PLANE223 elements and the plexiglass and concrete slab are PLANE183 elements. The areas where the plexiglass and solid surface meet are subjected to CONTA172 and TARGE16 elements to account for the contact behavior.

The applied force is equivalent of 688 N or 1 MPa pressure onto an area the same diameter as the element, varied from the center to the edge of the stepping tile, as shown in fig. 4.6. The top and bottom areas are coupled electrically, with the bottom grounded. The results of the coupled voltage output is shown in fig. 4.7, with significant output shown until about 3 cm away from the center.

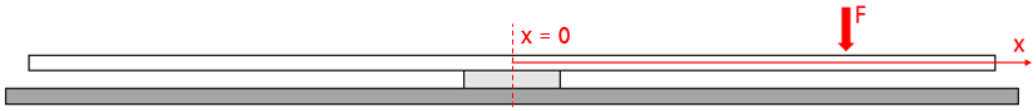

Figure 4.6: Schematic of stepping tile with piezoceramic element in center

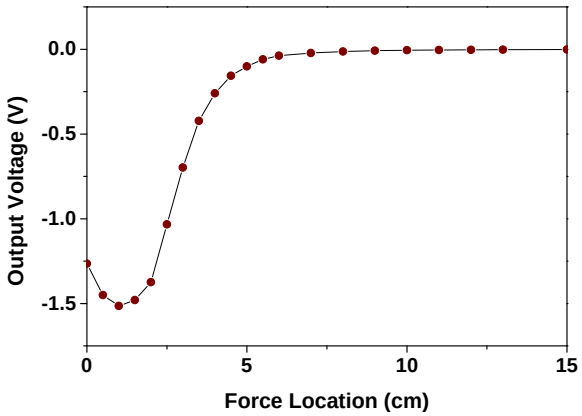

Figure 4.7: Voltage output of PZT-5A element under applied force of varying location from center

The spatial analysis was then extended to a three ceramic case where the force was again varied in location from the center to the edge of the tile, as can be seen in fig. 4.8. Here, x-poled ceramic indicates poling in the length direction, while y-poled means poled in the thickness direction. Fig. 4.9 indicates that when the force is located in between the first and second ceramics, the ceramic is in compression in the x-direction at the location of maximum stress and in tension at the location of maximum stress when the force is in between the second and third elements. This behavior in the x-poled ceramics, compared to the behavior of y-poled ceramics shown in fig. 4.9, is not desirable because it can cancel out the effect of stress in different locations, resulting in a lower total electric potential.

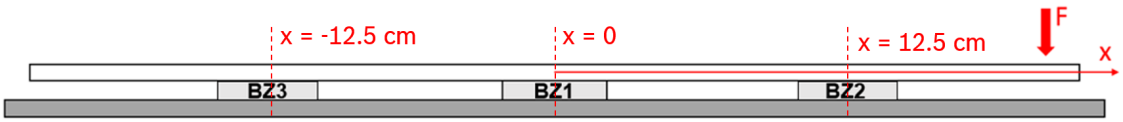

Figure 4.8: Schematic of stepping tile with three underlying piezoceramic elements

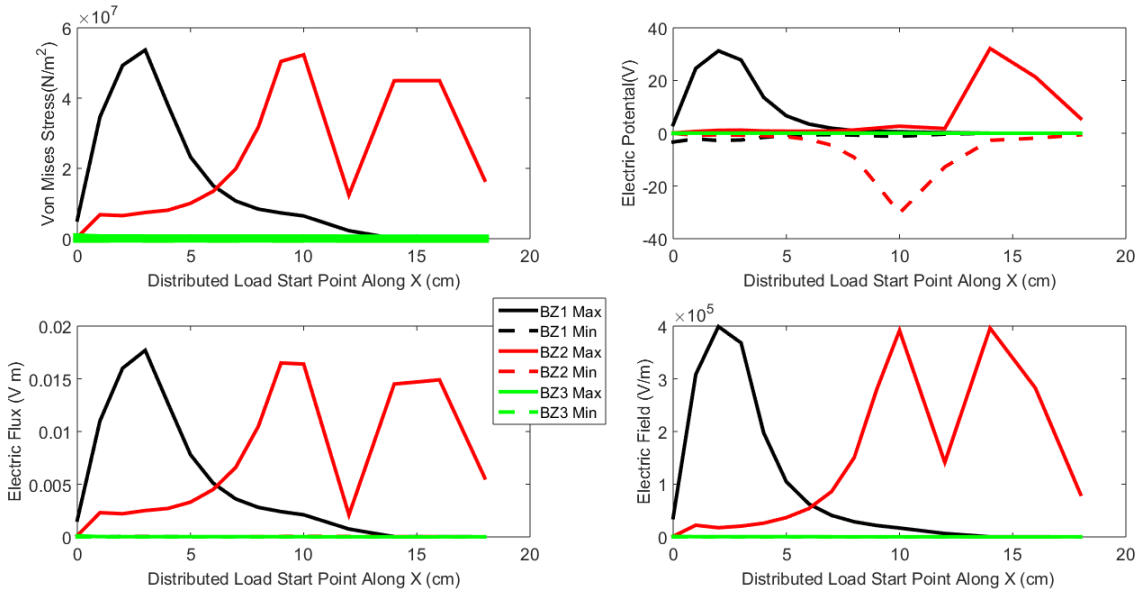

Figure 4.9: Spatial analysis of three x-poled ceramics under distributed force

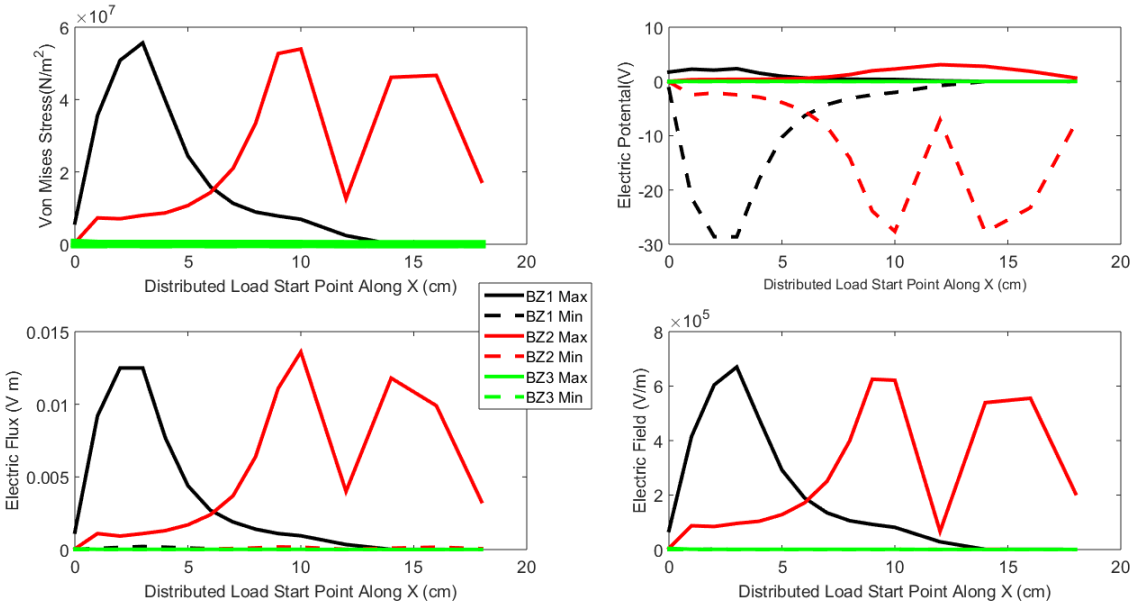

Figure 4.10: Spatial analysis of three y-poled ceramics under distributed force

4.1.3 Experimental Validation

To verify the results of the simulations, a testing mechanism as shown in fig. 4.11 was constructed to mimic the forces of human steps. Because a person simply stepping onto tiles is not a repeatable and trusted method of testing, a pneumatic piston controlled by a

solenoid valve attached to a flow meter and pressure regulator was utilized. The regulator can be controlled to adjust the applied force onto the materials from weight equivalents of a child (35 kg) to an NFL player (115 kg). The flow meter allows for adjustment of the air flow speed and along with the Arduino controlled solenoid valve, the extend and retract time of the piston, and ultimately the frequency of the applied force, is controlled. The pressure sensor measures the pressure input into the piston, which can then be calculated into the applied force utilizing the geometry of the piston.

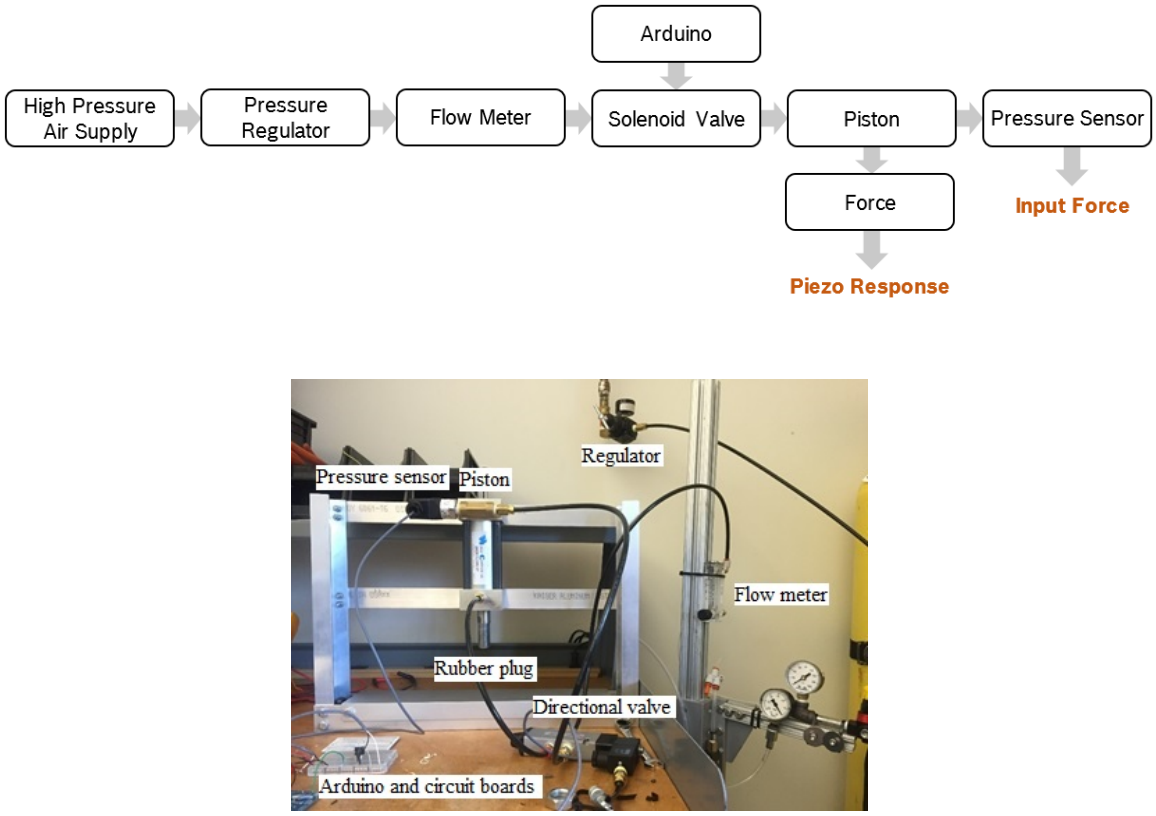

Figure 4.11: Testing mechanism utilized for human footstep generation

Measurements of the voltage output of a PZT-5A ceramic sheet at varying applied force were completed to compare to the results of the simulations in ANSYS and verify the results of the simulations. The voltage amplitudes listed in the experimental result are the peak voltage values that occur when the force is first applied onto the piezoceramic. The voltage is measured through a 10 MΩ probe, and it is assumed that the resistance internal to

the system is much lower than the probe resistance. It can be seen in the simulated results of fig. 4.12 that there is a linear relationship between the applied force and the output voltage. The experiment shows a comparable result, but the discrepancy at the lower force is high as seen in tab. 4.3 due to the piston needing a certain input of pressure to operate in a smooth continuous motion.

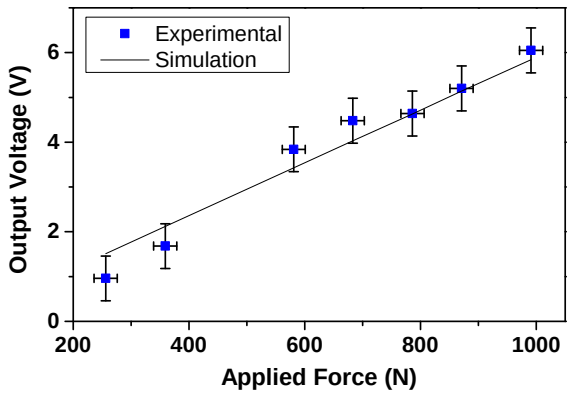

Figure 4.12: Output voltage comparison between experiment and simulation for varying input force

Table 4.3: Values of applied force and output voltage for simulated and experimental results

Applied Force (N)	**Output Voltage (V)**		**Percent Difference (%)**
	Simulation	**Experimental**	
256	1.51	0.96	36.4
359	2.12	1.68	20.8
581	3.43	3.84	12.0
683	4.03	4.48	11.2
786	4.63	4.64	0.22
871	5.14	5.20	1.16
991	5.84	6.05	3.60

A typical behavior of the electrical response of a piezoceramic material for a step force is shown in fig. 4.13. The pressure is adjusted to apply a force of 1000 N and the piston is extended for 1 s, then retracted for 2 s. As the force is first applied on the material, there is a spike in the output voltage and an equal but opposite spike in the negative voltage when the force is released. The behavior is much like a capacitor being charged and discharged, as expected from the material characteristics of a piezoceramic disk.

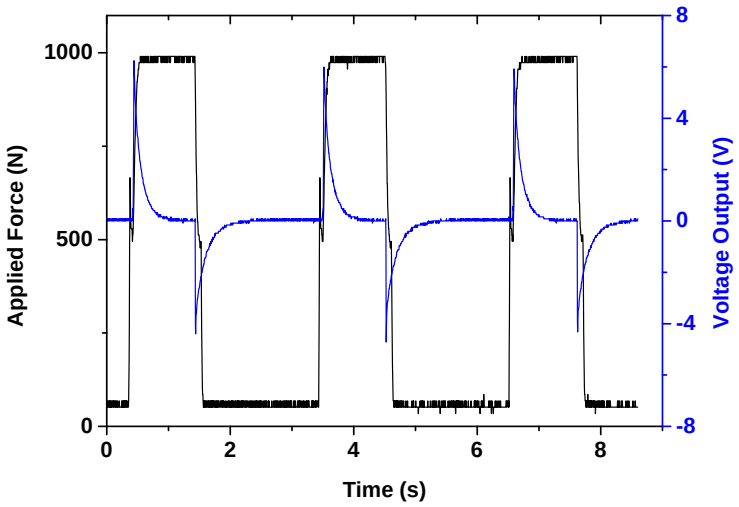

Figure 4.13: Voltage response of PZT-5A ceramic for a step input force

CHAPTER 5
PLUCKING TILE

As an effort to bridge the gap between the inherently high resonant frequency of piezoelectric materials and the input of low frequency human footsteps, a plucking tile was designed and 3D printed. Inspired by the idea of knee-joint energy harvester utilizing piezoelectric bimorphs [31], the plucking tile aims to maximize the vibration of the bimorphs with each step through frequency up-conversion.

5.1 Design

The tile consists of top and bottom layers as designed in fig. 5.1. The bottom layer holds piezoelectric bimorphs anchored on one end as cantilever beams as can be observed in fig. 5.2, while the top pushes down on the edges of the bimorphs with a protrusion in the center of the tile as a person steps onto the tile. The weight is removed when the person steps down, and the springs between the top and bottom tiles will allow for the top layer to return to its original position, leaving the bimorphs to freely vibrate and essentially ”plucking” them.

The two possible configurations of piezoelectric bimorphs include series and parallel operation, as shown in fig. 5.3. For the series operation, the two plates are polarized in the same direction with respect to the center shim and the leads are attached to the two outer electrodes. The parallel operation has plates polarized in the opposite directions with respect to the center and one lead is attached to the center shim, while the other lead is attached to both the outer electrodes. The parallel configuration has the possibility to generate twice the charge of the series connection, but the series connection has the advantage of easier wiring.

Figure 5.1: 3D rendered parts for the plucking tile

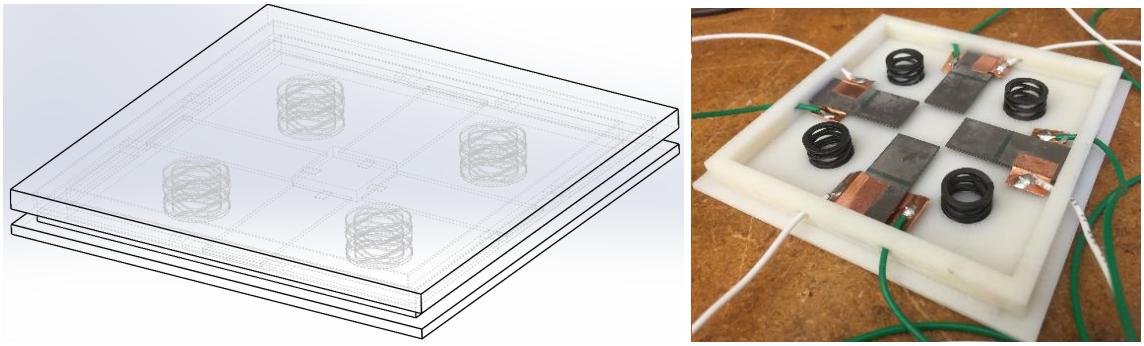

Figure 5.2: Assembled plucking tile bottom with bimorphs and springs attached

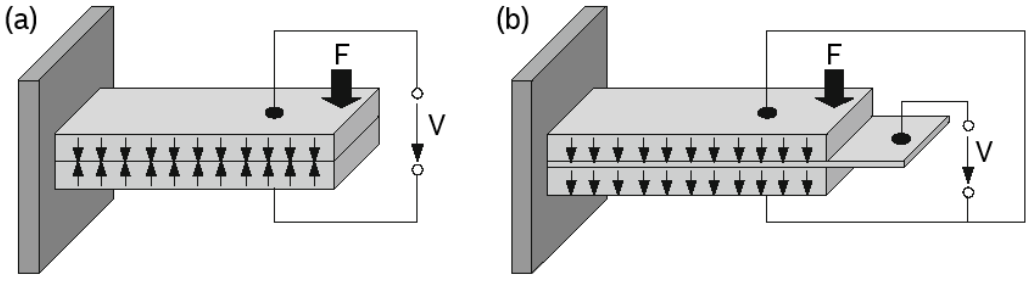

Figure 5.3: (a) Series and (b) parallel configurations of piezoelectric bimorphs [22]

5.2 Finite Element Analysis

To study the effect of frequency and electrical loads in power generation of the bimorphs, finite element analysis through ANSYS was utilized. The analysis is divided into modal and harmonic analysis for the two possible configurations of piezoelectric bimorphs. The simplified model is a cantilevered beam with elements SOLID226 for the piezoceramics, SOLID186 for the brass shim and CIRCU94 for the attached electrical load and subjected to a load of 10 mN at the free end as observed in fig. 5.4.

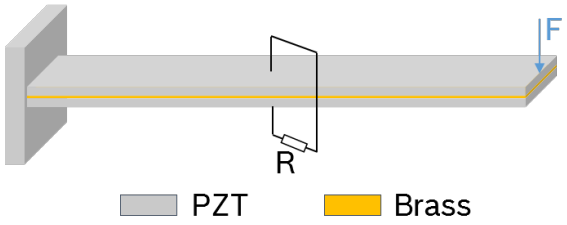

Figure 5.4: Mechanical configuration of the bimorph model for FEM

Fig. 5.5 depicts the electrical configuration of the series bimorph cantilever model. The top and bottom surfaces each had coupled electric potentials to common nodes 1 and 2, which served as the electrodes. The load resistors were connected to the two nodes to create a closed circuit and the resistance was specified in a range of real constants. The electric potential of the brass layer was coupled and constrained to zero.

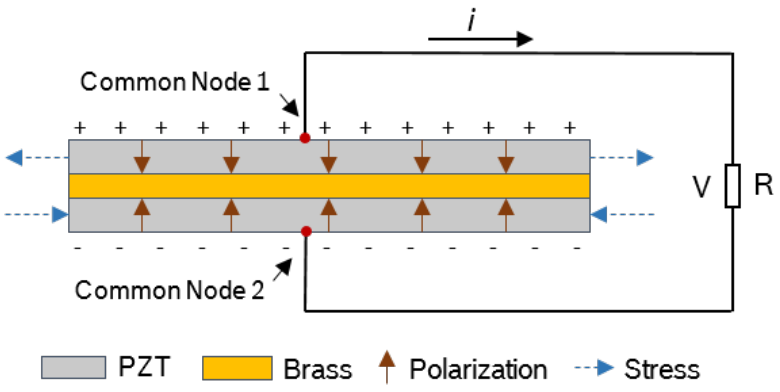

Figure 5.5: Electrical configuration of the series bimorph model for FEM

Because the direction of stress applied to the system and the direction of polarization are different, the coefficients of interest in the bimorph configuration is piezoelectric coefficients in the 31 mode. In tab. 5.1 are the mechanical quality factor and density of the PZT bimorphs used in this tile: material types PSI-5A4E and PSI-5H4E from Piezo Systems, Inc. (Piezo Systems Inc., Woburn, MA). The modal analysis results, or the resonant frequencies of PZT bimorphs of dimensions of thickness 0.38 mm, width 12.7 mm and length 31.8 mm revealed that the resonant frequency is 189.6 Hz and 189.4 Hz, respectively for PSI-5A4E and PSI-5H4E. For the harmonic analysis, the model has to include viscous damping with the damping matrix given by

$$C = \beta_{PZT} K_{PZT} + \beta_{brass} K_{brass} \tag{5.1}$$

where β refers to the damping factor and K refers to the structure stiffness matrix [31]. The damping factors were then calculated accordingly as shown previously as

$$\beta = 1/\omega Q_M \tag{5.2}$$

Table 5.1: Material properties of piezoceramics and brass

	PSI-5A4E	**PSI-5H4E**	**Brass**
Q_M	80	30	2500
ρ (kg/m^3)	7800	7800	8700
$\varepsilon_{33}^T/\varepsilon_0$	1800	3800	
d_{31} (m/V)	-190e-12	-320e-12	
g_{31} (m^2/C)	-11.6e-3	-9.5e-3	
k_{31}	0.35	0.44	

Then, harmonic analysis is utilized to study the effect of varying the load impedance on the electrical output. For each bimorph, a load of 10 mN is applied to the edge of the beam, which is then subjected to harmonic analysis at frequencies in the range close to

the resonant frequency show above. It can be observed in fig. 5.6 and fig. 5.7 that there is an increase in voltage amplitude, as the impedance load increases. This is as expected since the impedance load and the resistance of the piezoelectric bimorph, due to damping and parasitic capacitance, work as a voltage divider. As the impedance load increases, there is a higher voltage extracted through the load. At off-resonant frequencies, PSI-5H4E displayed higher amplitudes of voltage due to its higher coupling coefficient. However, it can be observed that the peak voltage amplitude of PSI-5A4E is higher, or at the resonant frequency. This is due to the higher mechanical quality factor of PSI-5A4E, which is the amplification factor of vibration of a piezoelectric resonator in resonance conditions [37].

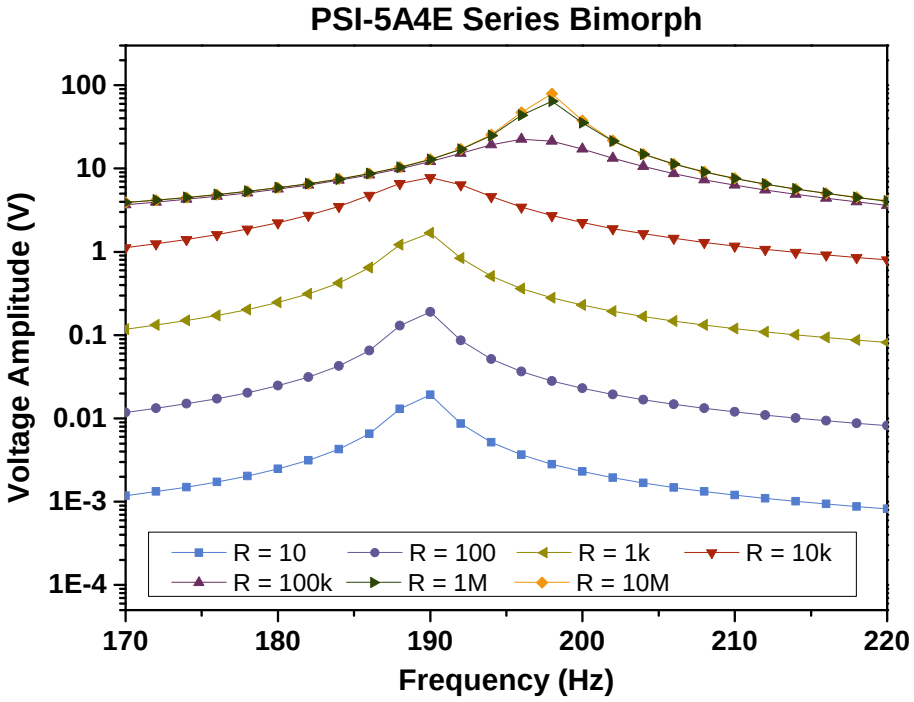

Figure 5.6: Output voltage of PSI-5A4E bimorph according to electrical load

The RMS power is calculated utilizing eq. 4.4. It can be observed that for both the PSI-5A4E and PSI-5H4E bimorphs, the highest power output is at 10 kΩ, as seen in fig. 5.8 and 5.9. While this value may be estimated using the capacitance given in the data sheets for the bimorphs, the capacitance given in the data sheet is measured at zero loading and it changes as stress is applied.

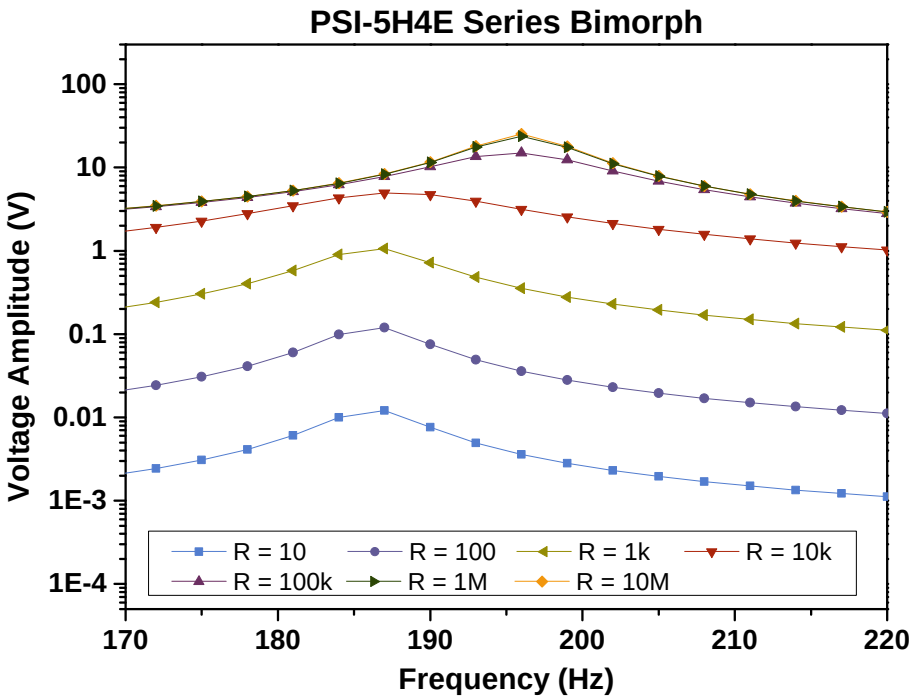

Figure 5.7: Output voltage of PSI-5H4E bimorph according to electrical load

It is also noted that the electrical loads with higher power are also related to larger deflection. The resistance values with the lowest deflection amplitudes, 100 kΩ for PSI-5A4E and 10 kΩ for PSI-5H4E, as seen in figs. 5.10 and 5.11, correspond to the highest electrical damping. These values also correspond to the curves that are the broadest with the largest area under the curves. This indicates the most efficient power transfer from the piezoelectric bimorph to the resistor.

However, excessive strain in the bimorphs can lead to reduced operation life or failure. Especially in the case of stepping tiles where users deflect the tiles, the displacement of the tiles should be minimized for user comfort. To determine the resistor value that yields maximum power whilst limiting the strain of the material, a figure of merit should be considered. Ratio of the voltage to deflection is not suitable because the voltage and deflection are linearly related. Ratio of power to deflection is not suitable because the power depends on the square of the displacement, as given by the voltage. Therefore, the quantity as defined below is utilized:

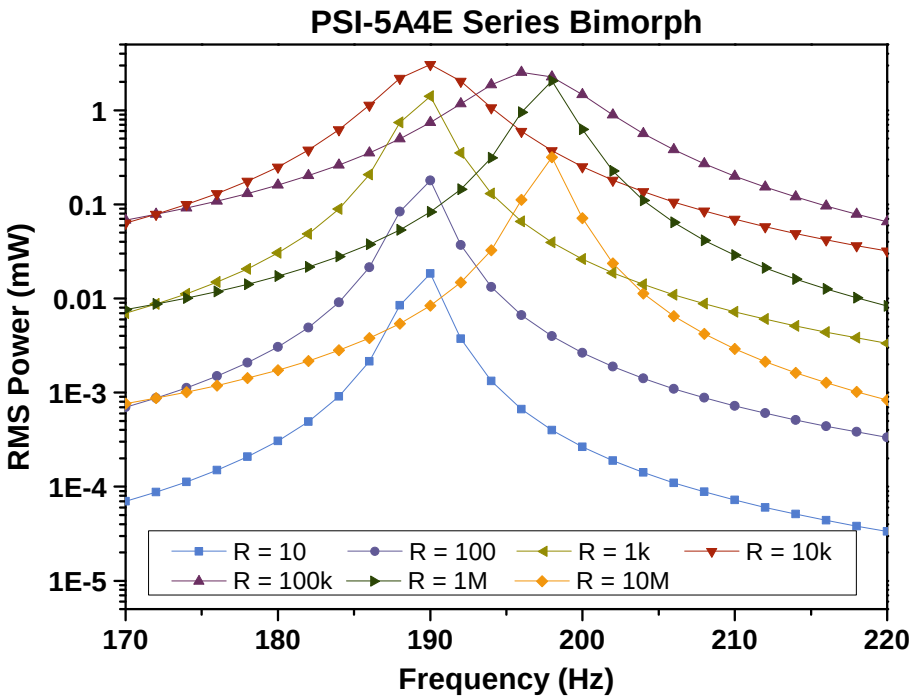

Figure 5.8: RMS power of PSI-5A4E bimorph according to electrical load

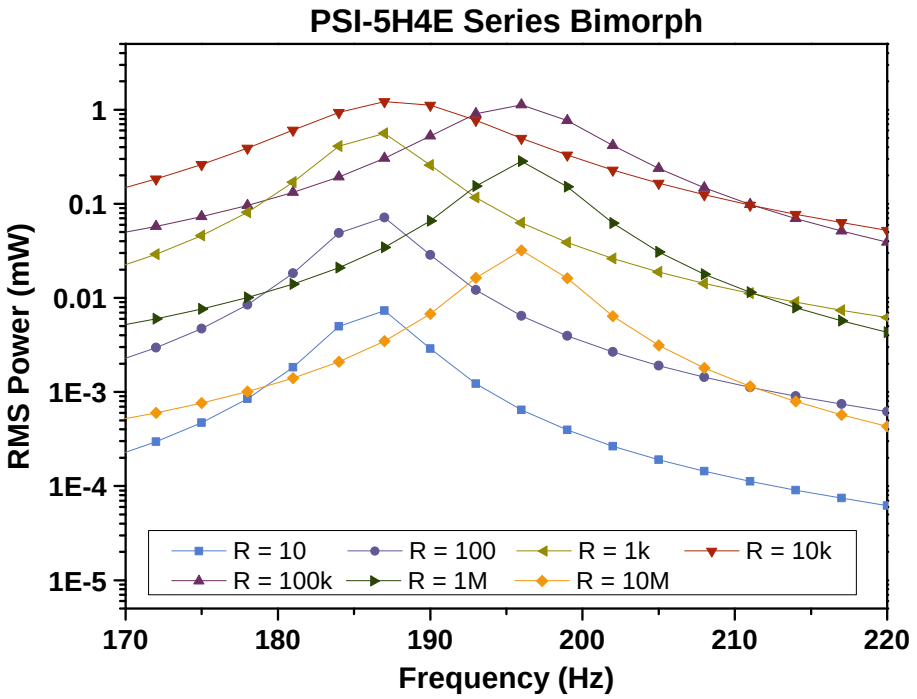

Figure 5.9: RMS power of PSI-5H4E bimorph according to electrical load

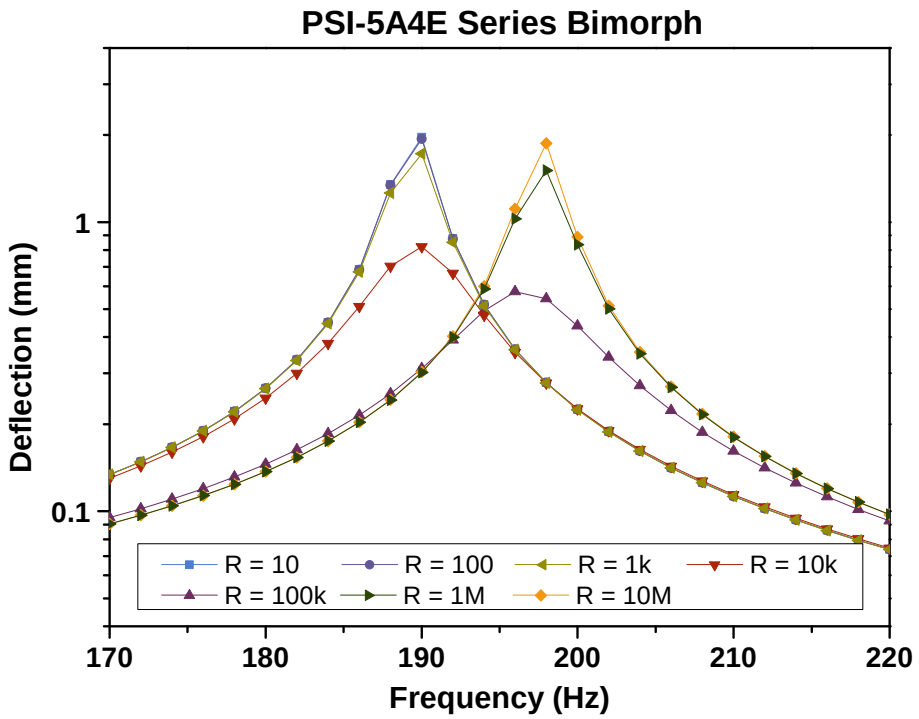

Figure 5.10: Deflection of PSI-5A4E bimorph according to electrical load

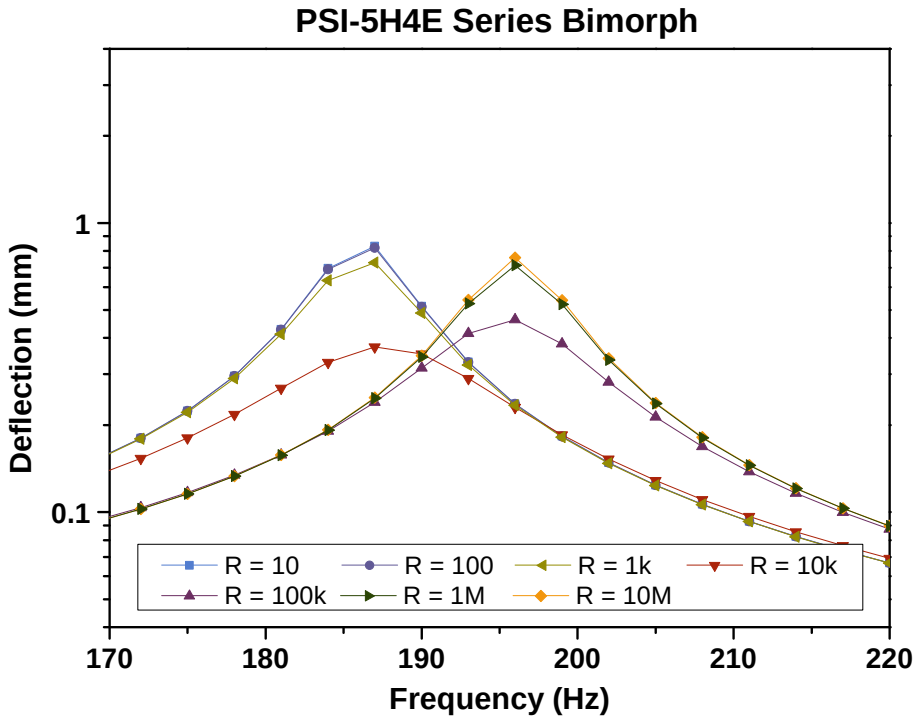

Figure 5.11: Deflection of PSI-5H4E bimorph according to electrical load

$$z = \frac{\sqrt{P}}{\delta} \tag{5.3}$$

where P is the power output and δ is the deflection [31].

As can be seen in fig. 5.12, the highest figure of merit is seen for the PZT-5H bimorph at 10 kΩ of resistance. Although the PZT-5A exhibited higher power output, the deflection related to the value is higher, which is not a desirable factor for a stepping tile.

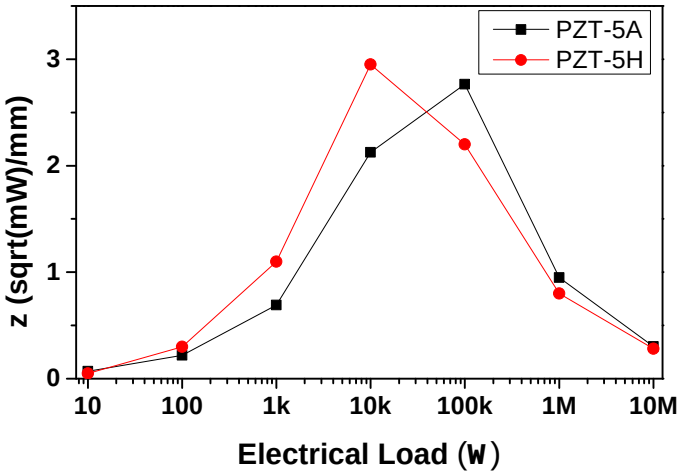

Figure 5.12: Figure of merit comparison for PZT materials according to electrical load

5.3 Experimental Results

A stepping tile was assembled using four bimorphs T215-H4-303Y from Piezo Systems, Inc. The bimorphs are of series configuration and geometry of width 12.7 mm, length 31.8 mm and thickness 0.66 mm. Bimorphs of larger thickness than the one chosen for the simulations were available and therefore chosen to maximize the power output. The tiles were designed to have a deflection of 1 mm, based on the simulation results. To measure the performance of the tiles, they were placed under the testing mechanism and the piston exerted a force equivalent of 440 N for 0.5 s, retracted for 1 s and repeated three runs. The signal is rectified through a full-wave rectifying bridge to convert the resulting negative voltage into positive signal. A potentiometer is attached in parallel to the signal and the

total electrical load of the probe and potentiometer is measured with a multimeter before conducting each cycle.

For the first configuration, the bimorphs were attached electrically in parallel, essentially giving the output of just one bimorph. Fig. 5.13 shows the output voltage of each run and it can be observed that as electrical load increases, the dampening effect of the bimorphs reaches the point where the remaining voltage of the bimorph is not completely drained by the time that the load is lifted. The highest instantaneous power output achieved for this configuration is 7.01 mW.

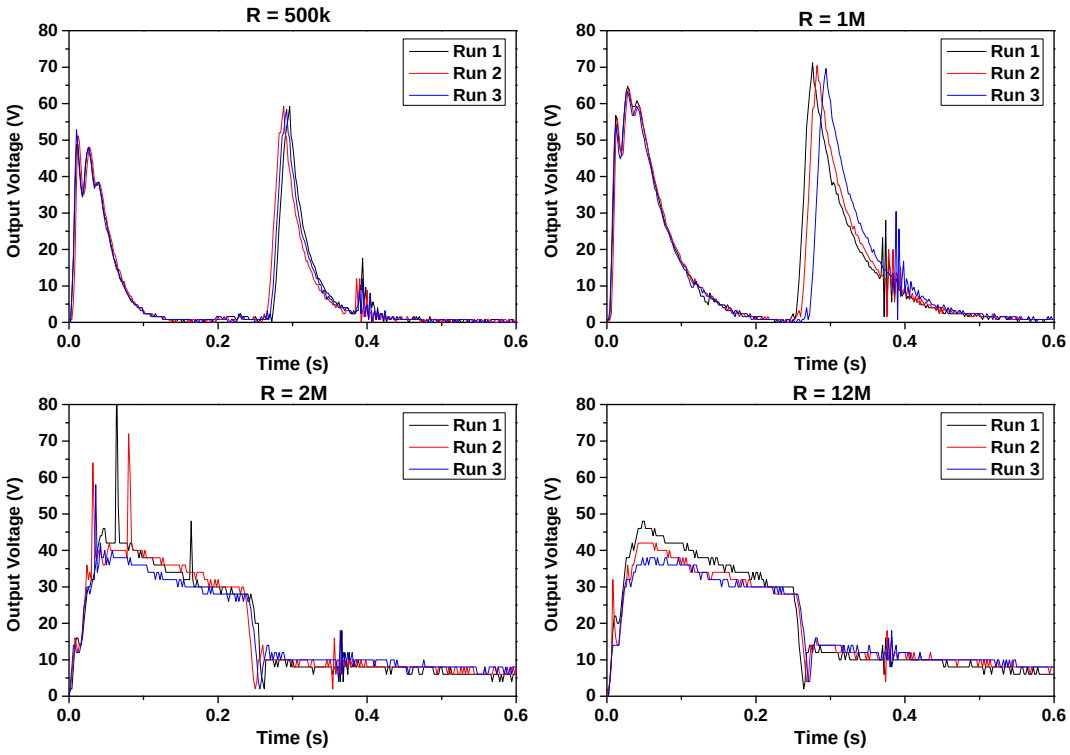

Figure 5.13: Voltage output of a plucking tile with four PSI-5H4E bimorphs of series configuration connected in parallel and rectified with a full-wave rectifying bridge

Fig. 5.14 shows the output voltage when the bimorphs are connected electrically in series instead. The resulting voltage is significantly lower, indicating that the piezoelectric effect of each bimorph is canceled out by one another. Theoretically, electrically connecting the bimorphs in series should result in higher output, but this may be due to slight offset in each cantilevered bimorph resulting in cancellation in total output.

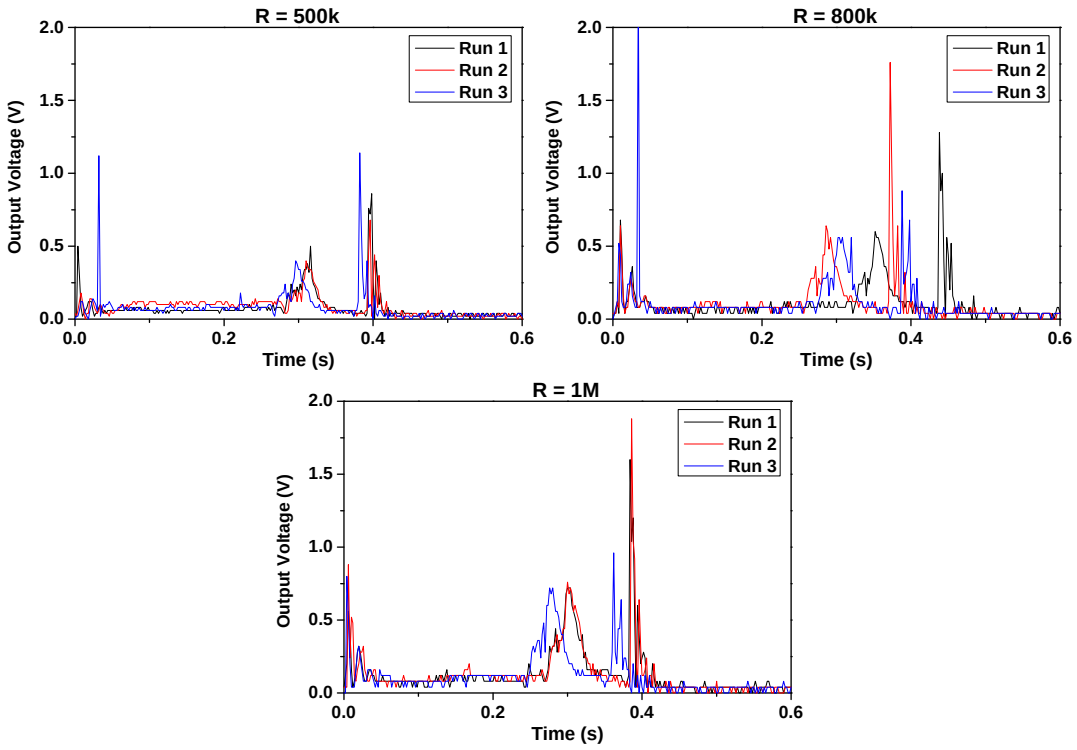

Figure 5.14: Voltage output of a plucking tile with four PSI-5H4E bimorphs of series configuration connected in series and rectified with a full-wave rectifying bridge

Another tile was constructed using four bimorphs supplied by Noliac (Noliac, Kvistgard, Denmark), with dimensions length 45 mm, width 10 mm and thickness 0.5 mm. The material is similar to that of Piezo Systems Inc. as previously used, but it has a higher mechanical Q factor of 80 and a parallel configuration. For this design of the tile, the bimorphs are allowed an initial deflection of 1.5 mm, but it is only fixed on the exposed brass layer and has larger springs in the tile. Again, equivalent force of 440 N is applied by the piston for 0.5 s, retracted for 1 s and repeated for three runs in each cycle. The bimorphs are rectified in signal and attached to an electrical load to measure instantaneous power. Fig. 5.15 shows the results when the bimorphs are connected in parallel with each other.

Fig. 5.16 is the result for the same plucking tile as above, but in electrically series connection. It can be observed that the series connection yields a much higher output for this plucking tile, adding the output of each bimorph into a higher overall power output. The highest instantaneous power seen in this configuration is 2.46 mW, which is still lower

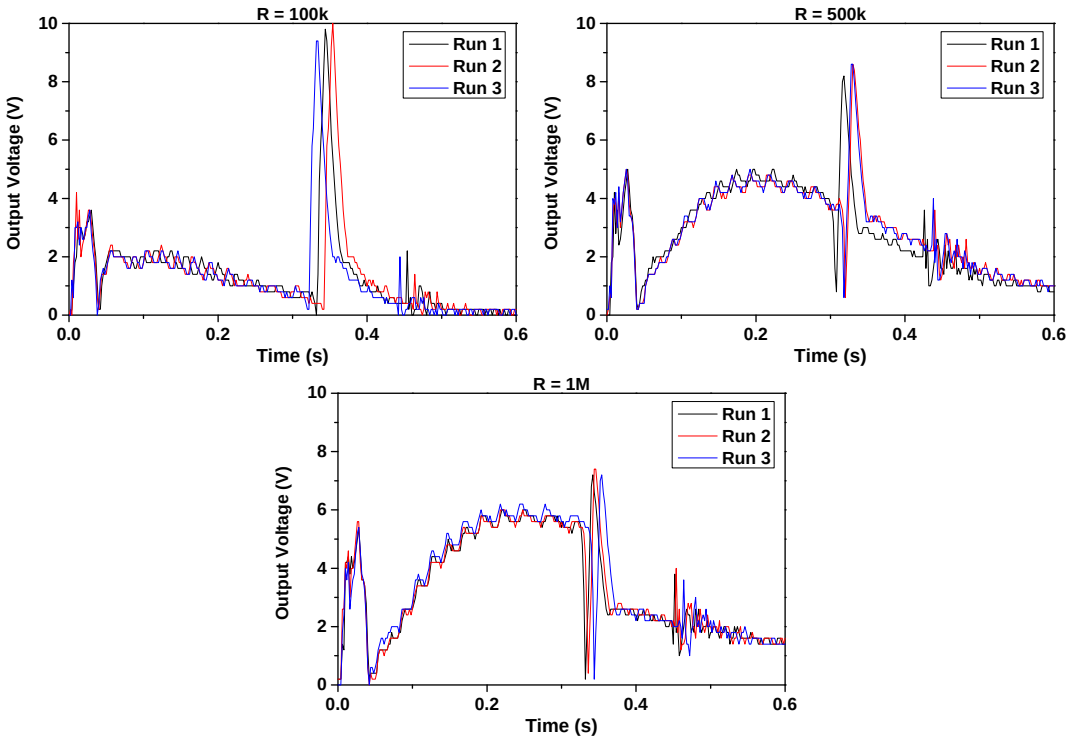

Figure 5.15: Voltage output of a plucking tile with four Noliac bimorphs of parallel configuration connected in parallel and rectified with a full-wave rectifying bridge

than the first tile, but it should be taken into consideration that it is composed of thinner bimorphs.

It can be observed that the impedances used in the experimental results are higher than the matched values in the simulations. This is due to the fact that while plucking leads to a higher frequency, it is not quite the harmonic frequency. Due to this, a higher impedance is needed as shown in fig. 2.5. Although a direct comparison of the simulation is not viable, the results of the simulation, such as deflection and material type, were reflected in designing the tiles.

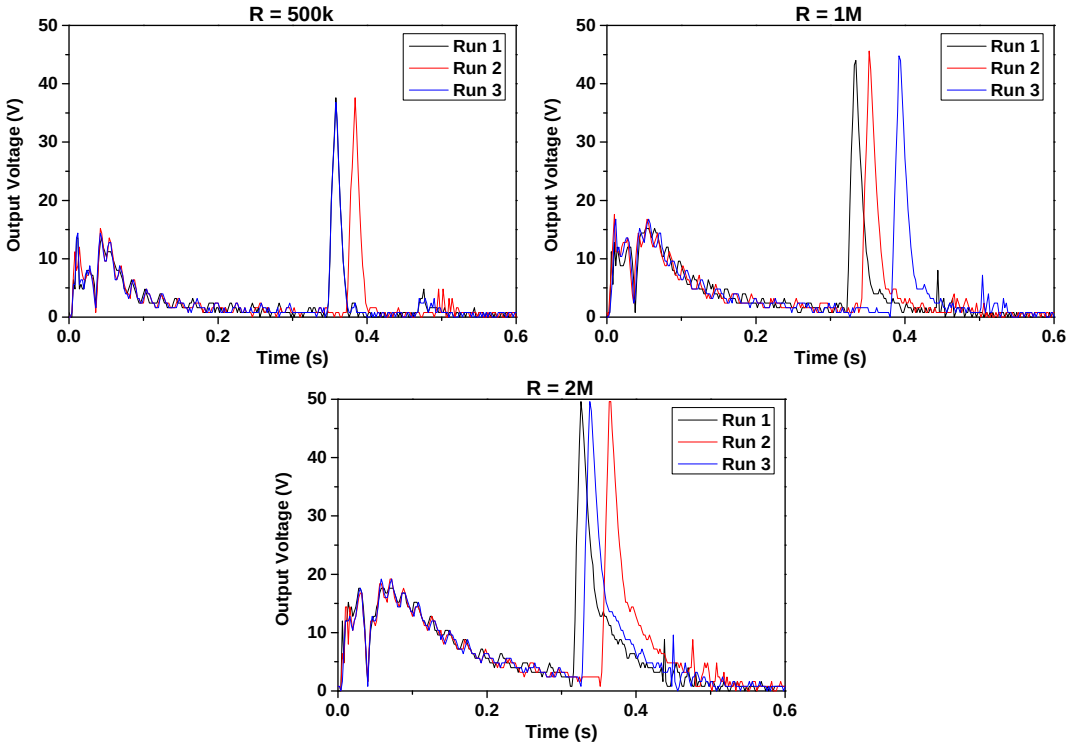

Figure 5.16: Voltage output of a plucking tile with four Noliac bimorphs of parallel configuration connected in series and rectified with a full-wave rectifying bridge

CHAPTER 6
CONCLUSION

Two methods of piezoelectric energy scavenging in the human scale were explored. The first was a simple compressive method, where piezoelectric elements affixed under stepping tiles are subjected to people stepping onto the tiles. While it was revealed that at the frequency of human scale motion, the power generation is significantly reduced compared to the range closer to the resonant frequency, this method is useful in applications that require low power generation and ease of manufacture, such as sensing through passive RFID tags. By comparison of various piezoceramic materials, geometry and spatial analysis through simulation and experimental methods, the system can be optimized.

The second method aimed to bridge the gap between the inherently high resonant frequency of piezoelectric materials and the low frequency of human scale motion. Finite element analysis was utilized to predict the power output and resulting deflection of bimorphs under resonant frequency. The results of the analysis were reflected in the design of the tiles and the experimental results revealed that the output power of this method is far more promising. While this method is still being explored, the preliminary results show potential for further increasing the power generation through human scale motion.

Part II

Integration of MEMS Accelerometers in Flexible Electronics

CHAPTER 7

INTRODUCTION

Flexibility implies many qualities, including bendable, stretchable, conformally shaped, elastic lightweight, nonbreakable, roll-to-roll manufacturable and large-area [38]. Anything thin is flexible and the field of flexible electronics has a longer history than one might imagine. Dating back to the 1960s, the first flexible solar cell arrays were developed by thinning single crystal silicon wafer cells to about 100 μm for application in extraterrestrial satellites [39]. The roll-to-roll fabrication of solar cells on flexible steel and organic polymer substrates were introduced in the early 1980s [40, 41].

Another driving force was the growth of displays, which started with the active-matrix liquid-crystal display industry in Japan in the mid-1980s. This led to the development of rollable plastic electrophoretic display by Phillips [42], flexible liquid crystal panel by Samsung and organic light-emitting diode (OLED) display with full-color made on steel foil by Universal Display Corporation [43]. Most recently, the quantum dot LED (QLED) technology was introduced by Samsung, utilizing a film of quantum dots in front of a LED panel [44]. With possible applications in wearable devices, e-textiles and flat-panel displays as shown in fig. 7.1, the field of flexible electronics continues to grow.

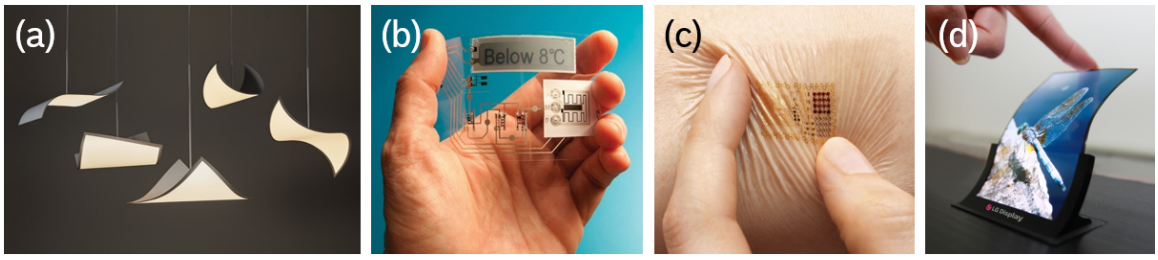

Figure 7.1: Areas of application for flexible electronics (a) OLED lighting [45] (b) Smart packaging [46] (c) Wearable health [47] (d) Flexible display [48]

7.1 Motivation and Objectives

Compared to its rigid counterparts, foil-based systems offer a high level of packaging density with thin components, as well as the additional advantage of mechanical flexibility [49]. Currently, the technology has advanced such that wafers can be prepared into thin dies, allowing them to be flexible [50]. Foils can serve as the substrates. However, the flexibility aspect does not only refer to the foil or component, but also implies compatibility of the components onto foil with stable mechanical and electrical interconnections [49]. With the lack of appropriate technology to package these devices, the system remains only partially flexible.

7.2 Scope of Work

In this thesis, two methods of packaging are studied in parallel as outlined in fig. 7.2. The first is the direct mounting of sensors onto foils, also referred to as chip-on-flex. Methods of decoupling the stress between rigid components and flexible board are discussed. The second is chip-in-flex, or the embedding of sensors into foil and mold, allowing complete integration and flexibility.

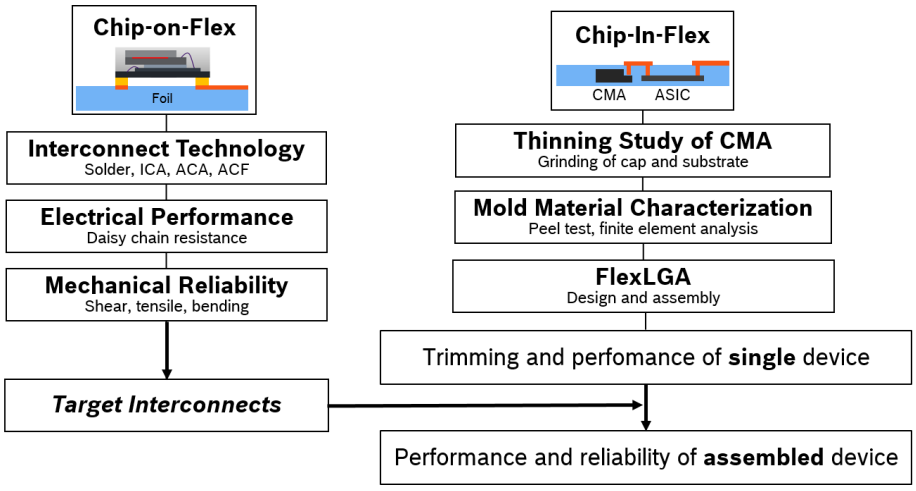

Figure 7.2: Overview of topics covered in thesis

CHAPTER 8
THEORETICAL BACKGROUND

8.1 MEMS Technology

MEMS, or microelectromechanical systems, are a collection of transducers and actuators that can sense its environment and react with the use of a microcircuit control [51]. The loosely defined term is used to describe systems with mechanical components characterized by small size [52], while the direct translation refers to systems with both mechanical and electrical structures in the micron-scale.

MEMS technology is made possible by silicon micromachining, or fashioning microscopic mechanical parts out of or on a silicon substrate. Micromachining dates back to as early as 1960s, when researchers experimented with using integrated circuit (IC) fabrication technologies to build mechanical structures [52]. Micromachining techniques are utilized to produce microstructures including cantilevers, beams and membranes [53]. With the possibility of batch fabrication, which allowed for simultaneous processing of thousands of identical devices on a single wafer, MEMS devices began replacing their larger counterparts.

8.2 MEMS Accelerometers

A MEMS device interacts with a physical, chemical or optical quantity and communicates with the outside world with an electrical interface inside an application-specific integrated circuit (ASIC) [54]. For MEMS sensors, the electrical output signal correlates with the input quantity that is sensed and inertial sensors detect acceleration and rotational rate. Since numerous types of inertial sensors with varying mechanisms exist, BMI160 from Bosch (Bosch Sensortec GmbH, Reutlingen, Germany) is presented as a primary example.

The BMI160 as shown in fig. 8.1(a) is a small, low power 16-bit inertial measurement unit with accelerometer and gyroscope capabilities. The sensor has a 14-pin (fig. 8.1(b)), 2.5 x 3.0 x 0.8 mm^3 land grid array (LGA) package. Fig. 8.1(c) shows the schematic of the inner structure of the system. The sensor combines two essential components in its housing: ASIC and MEMS components. The components are stacked vertically with the ASIC on the bottom, MEMS component on the top and a spacer between them. The MEMS component is composed of the substrate, structure and cap, where structure is located in a gas cavern and protected by a top-mounted cap. The MEMS structure is suspended at certain anchor points on the substrate and the substrate is connected to the ASIC by wire bonds. The spacer allows for wire connection between the ASIC and printed circuit board (PCB). The system is packaged by a hard epoxy mold material. The MEMS sensor is composed of a gyroscope (CMG) and an accelerometer (CMA) with the locations of each component as shown in fig. 8.1(d).

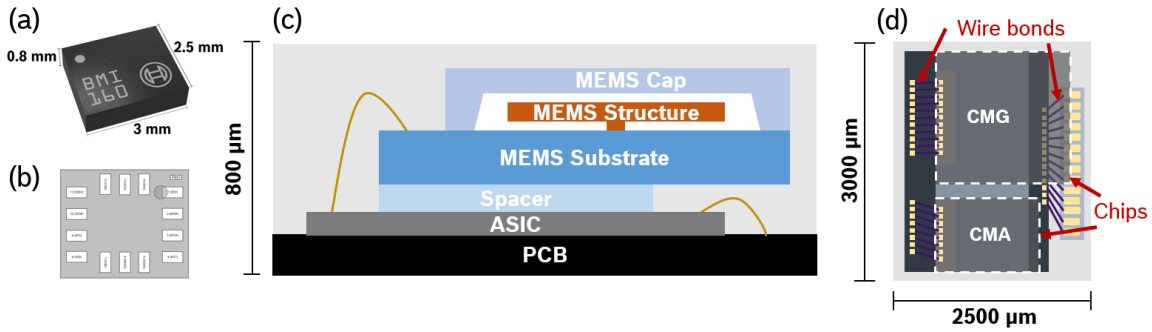

Figure 8.1: (a) BMI160 [55] (b) Bottom view of BMI160 [55] (c) Schematic of structure inside BMI160 [56] (d) Location of components and pads of BMI160

A micromachined accelerometer consists of a proof mass of mass M, suspended by compliant beams with spring factor of K and anchored to a fixed frame. Governed by spring law of $F = Ma = Kx$, the displacement, x is used to measure the force caused by external acceleration, a [57]. Vibrations are commonly damped by introducing gas inside the package to prevent excessive ringing [52]. The damping factor, D, affects the dynamic movement of the mass and the resulting mechanical transfer function is [57]:

$$H(s) = \frac{x(s)}{a(s)} = \frac{1}{s^2 + \frac{D}{M}s + \frac{K}{M}} \tag{8.1}$$

BMI160 is realized through capacitive sensing with a comb structure as shown in fig. 8.2(a), where only the yellow part is free to move [58]. During acceleration or deceleration, this movable mass is deflected by $\Delta x \propto a_{in}$ and the electrical capacitance between the measuring fingers or electrodes changes, as shown in fig. 8.2(b). The capacitance change is defined by the eq. 8.2, where ϵ_0 is the dielectric permittivity, A is the electrode area of overlap, x_0 is the initial distance between fingers, and Δx is the deflection of the mass. The change in capacitance is detected by the ASIC and converted into an acceleration measurement value.

$$C_{12} = \frac{\epsilon_0 A}{x_0 \pm \Delta x} \tag{8.2}$$

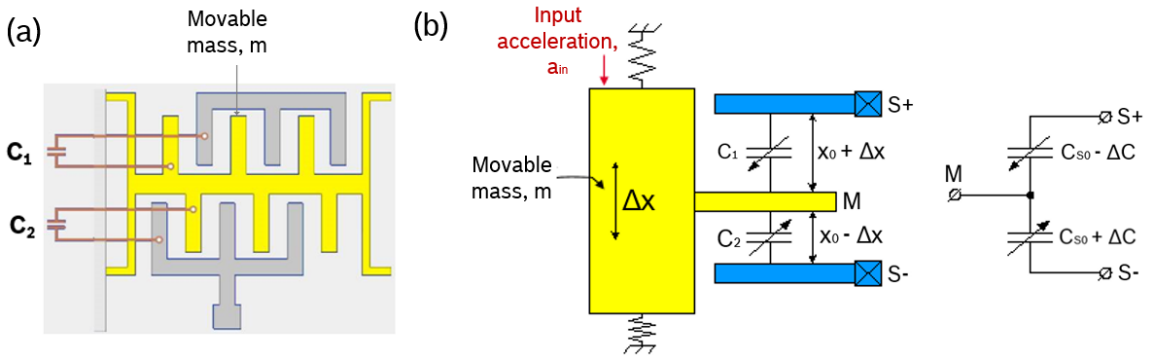

Figure 8.2: Working principle of a capacitive accelerometer [58] (a) Comb structure (b) Capacitive transduction

The critical device performance parameters for accelerometers include full scale range, sensitivity, zero-g offset, cross-axis sensitivity and noise. The measurement range is the level of acceleration supported by the sensor, or the greatest amount of acceleration that the part can measure and accurately represent as an output. The sensitivity is the ratio of change in acceleration to change in output signal. Zero-g offset specifies the output level when there is no acceleration. Cross-axis sensitivity measures the output on one axis when

acceleration is imposed on a different axis. Noise is the random deviation of the ideal output and power consumption. [59]

8.3 Packaging and Mounting Technology

Electronic packaging is the bridge that interconnects the MEMS and signal conditioning components into a system-level board to form electronic devices. Packaging has four main functions: (1) signal distribution, (2) power distribution, (3) heat dissipation, (4) and protection of components and interconnections. There are two main types of interconnection technology used between components, wire bonding and flip chip attachment. Wire bonding is the process of connecting the chip and external leads using fine bonding wires [60].

Flip-chip bonding as shown in fig. 8.3 refers to the process that involves face down bonding of chips to substrates [61]. Metal bumps are formed on the chip pads on the top side of the wafer and the chip with bumps is flipped over, so that its top side faces down. Metal bumps are aligned with matching pads and the chip is joined to the substrate. This provides low joint resistance, low parasitic capacitance and inductance and high density interconnections [62]. It is commonly assembled by solder bumps between the chip and substrate by reflowing solder.

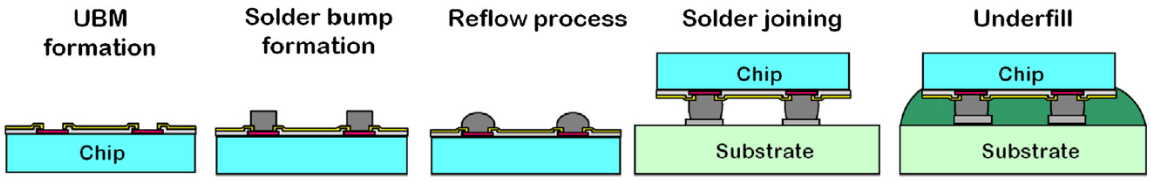

Figure 8.3: Flip chip bonding technology [61]

To enable the MEMS accelerometer to perform useful functions, the electrical interface is realized through ICs that provide the system with the necessary intelligence. The ASIC provides signal conditioning functions such as analog-to-digital conversion, amplification, temperature compensation and storage or filtering. The general approach in integration is the multi-chip solution where MEMS and IC components are manufactured on separate

substrates and subsequently hybridized in the final system. As seen in fig. 8.4, the chips are integrated (1) two-dimensionally side-by-side or (2) three-dimensionally through vertical stacking, utilizing wire bonding and/or flip chip bonding [54].

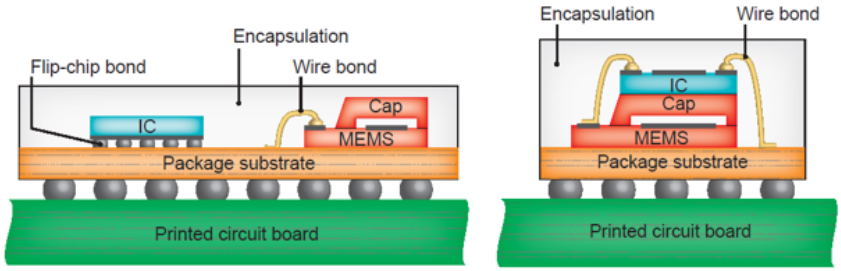

Figure 8.4: Multi-chip solution in integration of MEMS and IC [54]

8.4 Advanced Interconnects

Interconnection technology is vital in discussion of packaging. As seen in the overview of categories in the technology in fig. 8.5, there are two primary categories of electrically conductive adhesives. Adhesive interconnections offer multiple advantages over traditional tin-lead solders including low temperature processing, compatibility with a wide range of substrates, no flux pretreatment or postcleaning procedures required [63].

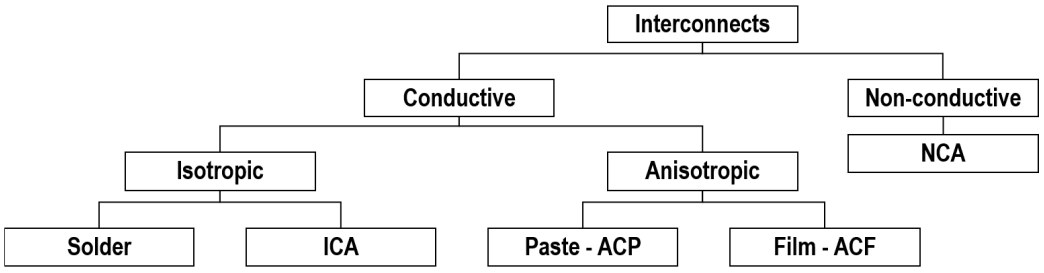

Figure 8.5: Outline of interconnect technology

Isotropic conductive adhesives, or ICAs, are electrically conductive in all directions. Non-filled ICAs are intrinsically conductive, whether they may be inherently conductive or doped. These materials are extremely brittle, sensitive to oxidation and therefore not a useful solder replacement. Another type of ICAs is composed of a polymer binder filled with

20 – 35 vol% metal loading [63]. This is based on the percolation theory, which predicts the amount of filler concentration at which a 3D network is established and conductivity of the composite increases suddenly by several orders. The percolation threshold refers to the point where the polymer is effectively transformed from an insulator to a conductor. The metal particles are uniformly distributed and form a network for electrons to flow across the particle contact points when the adhesive is cured. Common applications for this material include dies to lead-frames and attachment of surface mount devices to flexible circuits [61, 64, 65].

Anisotropic conductive adhesives, or ACAs, are produced either in paste or film form and provide unidirectional electrical conductivity in the vertical or z-axis. The directional conductivity is achieved by filling the polymer binder with a relatively lower percentage of the conductive filler, well below the percolation threshold. Common conductive particles include Au, Ag, Ni and Au/Ni metal balls or metal coated polymer balls, with diameter ranging from 3 to 10 μm. The low volume loading of the filler, usually between 5 to 10 %, is insufficient for inter-particle contacts and prevents conductivity in the x-y plane. As heat and pressure are simultaneously applied, the particles begin to bridge the surfaces, creating an electrical connection between the device and the substrate's metalization pads, as shown in fig. 8.6. Once continuity is produced, the polymer binder is hardened by a thermally initiated chemical or by cooling. This technology is commonly used for attaching chips to package lead frames and to connect flip-chips. While this material sacrifices ease of application, it has the possibility of achieving extremely fine pitch connections at a low process temperature and low cost. [61]

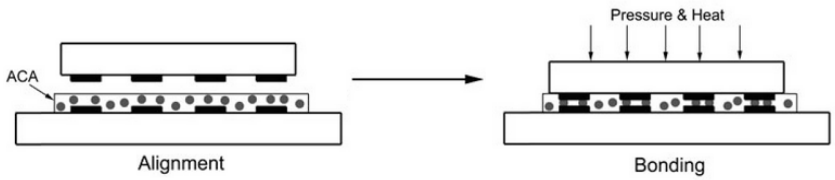

Figure 8.6: Bonding of anisotropic conductive materials [63]

CHAPTER 9
CURRENT DEVELOPMENT

As the field of flexible electronics continues to grow, there have been numerous studies in improving interconnect technology and embedding of sensors [66, 67]. However, there still exists a large gap between the established state of the art technology and the current state of research, which has not been developed enough for market production.

9.1 State of the Art

Electronics based on conventional printed circuit boards (PCB) is an established technology engineered to a high reliability level. The technology is based on metallic interconnections, mainly soldering, for which there are well-defined surface mount and through hole processes defined by industry-wide standards as well as technical specifications from entities such as the International Electrotechnical Commission [49]. For flexible electronics, reflow soldering is commonly utilized, where solder powder and flux are preblended to form a solder paste [68]. The paste is deposited onto the board onto the pads where the components are placed. The populated boards are heated above the liquidus temperature of the solder to reflow the paste.

9.2 Current State of Research

The development of micromachined sensors on flexible substrates began with microbolometers, which are thermal optical detectors whose electrical resistance changes as a result fo the heating from the absorbed optical radiation [69]. Early work included fabricating microbolometers on Kapton sheets bonded on Si carrier wafers, but the sheets were prone to distortion due to high thermal cycling [70]. The process was adapted to use polyimide

substrates formed by spin casting onto a Si carrier wafer and curing at the beginning of the microfabrication process, resulting in no distortion and allowing for precise alignment of the device features [71]. In terms of developing MEMS accelerometers on flexible substrates, conventional microfabrication equipment has been utilized in combination with low temperature processing techniques [67, 72].

Printed electronics industry developed a number of processes to print devices on an array of polymeric substrates, including polyethylene terephthalate (PET), polyethylene naphthalate (PEN), and polyimide (PI) [73]. This made screen printing of sacrificial and structural layers possible, allowing for new technology such as creation of motion sensors on fabric [74], capacitive gas sensors on PET [75], and large arrays of silver microbridges on PET [76]. Efforts in research were also focused on achieving MEMS and IC integration on flexible substrates through monolithic process to improve implementation process and system reliability [66].

While there is an ongoing development in organic electronics, it is still necessary to incorporate silicon technology in flexible system-in-foil products. Si chips become increasingly flexible at a thickness below approximately 150 μm, as shown in fig. 9.1, and are highly suitable for incorporation in flexible systems [50]. Processes of achieving thin chips include subtractive processes such as backgrinding and additive methods by the means of epitaxial growth [77]. Current technology of thinned bulk Si wafers suffers from thickness variations and topology, limiting the thickness to $>$ 30 - 50 μm, but lower thicknesses can be achieved through additive methods.

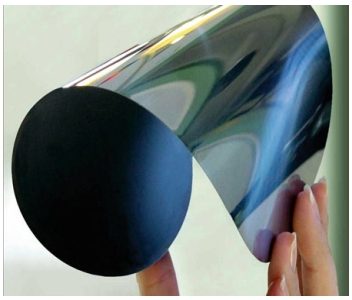

Figure 9.1: Flexible Si wafer of 50 μm thickness [50]

CHAPTER 10

CHIP-ON-FLEX

Chip-on-flex, or COF, packaging refers to surface mounting of sensors onto flexible boards. As our first approach in achieving integration of accelerometers in flexible electronics, methods of mounting the sensors onto flexible boards were explored. For a COF package, any stress applied on the flexible boards can cause mechanical stress on the sensors, especially if a rigid interconnect like solder is used. In order to decouple the stress between the sensors and flexible boards, various interconnect technologies have been explored and characterized.

10.1 Electrical Characterization

To characterize the electrical performance of the interconnect materials, dummy sensors made out of standard PCB material with the dimensions of a BMI160 sensor and a PCB with daisy chain design were utilized, as shown in fig. 10.1. Utilizing materials including solder, ICA, ACA and ACF, the dummy sensor assemblies were fabricated according to the processing temperature and time listed in fig. 10.2.

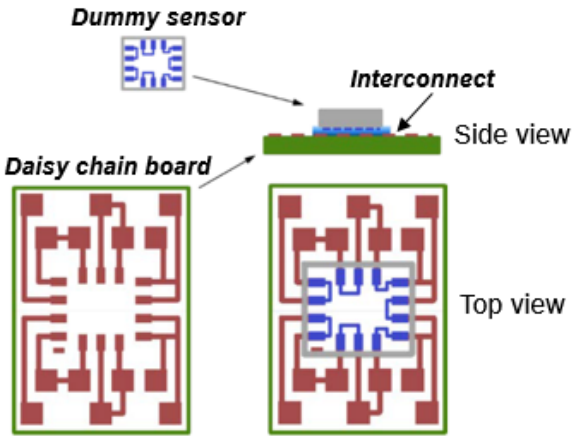

Figure 10.1: Dummy sensor with daisy chain board for resistance measurement

In comparing the electrical reliability of the interconnects, it is important to consider the required process parameters. While some may provide smaller resistance, they may require a higher processing temperature or a longer processing time, which can cause damage to the components and flexible mold. The processing temperature varies from 140 °C to 270 °C with the highest being solder, and the processing time is as short as five seconds and as long as 20 minutes.

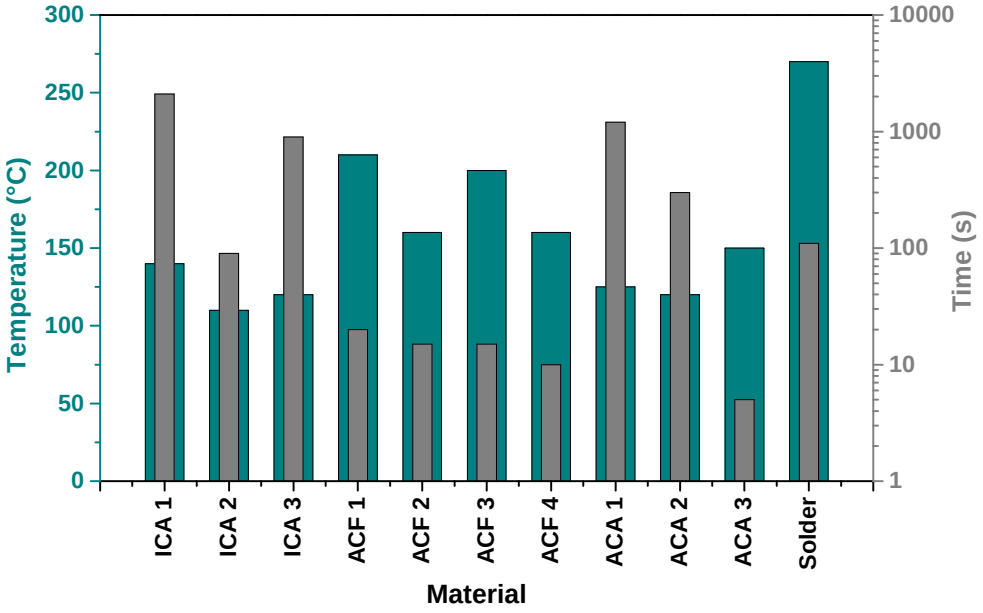

Figure 10.2: Process parameters of chosen interconnect materials

Fig. 10.3 shows the resistance of the longest daisy chain, as measured by Keithley 2400 Sourcemeter. The ICAs performed with lower resistance values than solder. For anisotropic materials, a range of processing pressures was used to study the influence of applied pressure on the electrical performance. As it is with the processing temperature and time, the processing pressure should be minimized to avoid damaging the flexible mold, fragile chips and wire bonds. It can be observed that ACF 1, 3, 4 and ACA 3 show stable electrical connection over the range of processing pressure, while the resistance values of ACF 2, ACA 1 and 2 increase noticeably as the applied pressure is decreased.

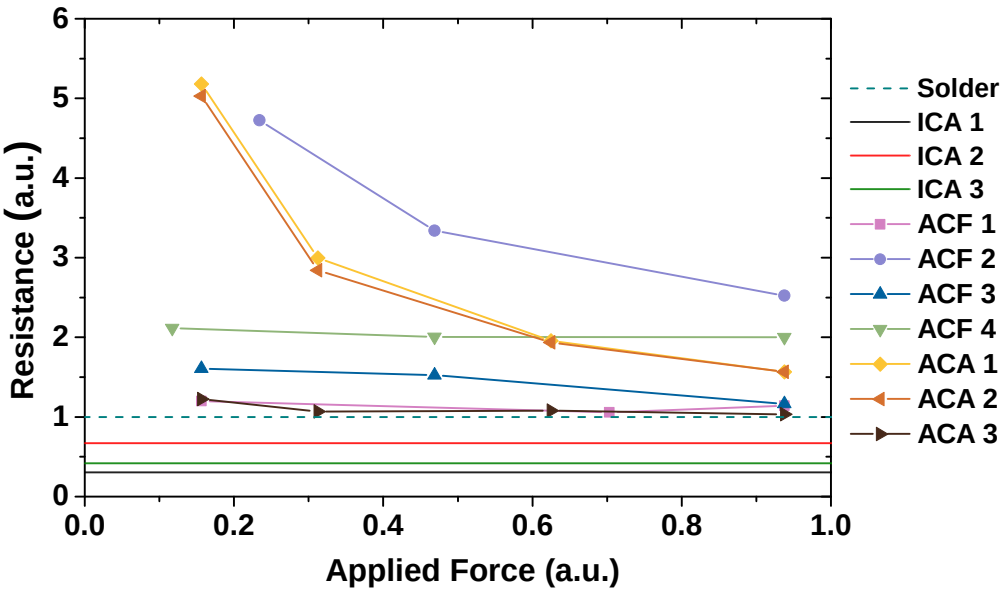

Figure 10.3: Resistance measurements of various interconnect materials

10.2 Mechanical Characterization

In flexible electronics, the mechanical reliability of the interconnects is vital in order to maintain stable connection as the system goes through stress while bending or stretching. For mechanical characterization of the interconnect materials, shear test, tensile test and bending test were performed.

10.2.1 Shear Test

As a method to directly compare the mechanical strength of the interconnects under stress, a simple shear test was conducted utilizing the dummy sensors from the electrical performance test. Fig. 10.4 shows the setup where the dummy sensors are placed on a fixture block and a shear load is applied onto the dummy sensor until fracture of the interconnect. As shown in the results in fig. 10.5, most of the anisotropic materials performed comparably with the solder, with ACA 3 and ACF 1 displaying the highest shear strength. The ICAs performed poorly at shear forces at break much lower than that of solder.

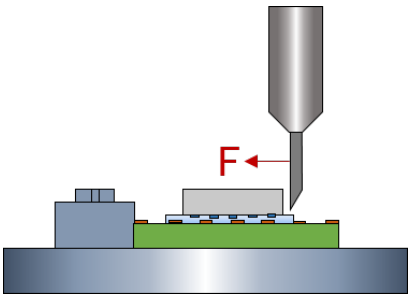

Figure 10.4: Shear test setup

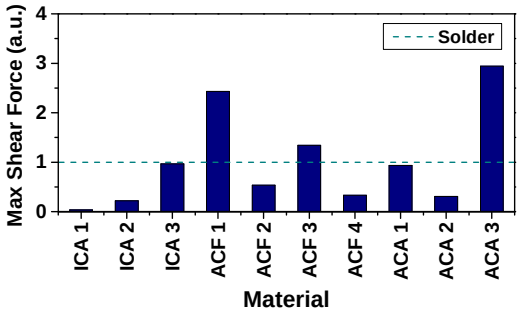

Figure 10.5: Maximum shear force of chosen interconnect materials

10.2.2 Tensile Test

A tensile test was conducted to observe the behavior of BMI160 sensors under an applied external tensile force on the foil. When an external tensile force is applied onto the foil, the stress is transferred to the interconnect material and the sensor, ultimately into the MEMS core. Any stress and strain of the MEMS core results in an offset or change in sensitivity in measurements of the accelerometer, leading to measurement deviations.

A BMI160 sensor is soldered onto a PI foil rotated at 135° angle. The rotation angle was chosen from a previous simulation conducted that revealed the load angles at which the offsets were the most prominent (see Appendix B for simulation boundary conditions and results). The foil was fixed at the ends and a slowly increasing tensile force is applied, as shown in fig. 10.6. For the measured offset, the deviation at the beginning of the measurement is high due to the sample specimen not being completely taut. It can be observed in fig. 10.7 that as the applied tensile force increases, the offset increases as well. The relationship between the tensile force and the resulting offset is linear. The influence of the applied tensile force is significant, but still comparable and within limits of the specified zero-g offset of BMI160 except the y-offset.

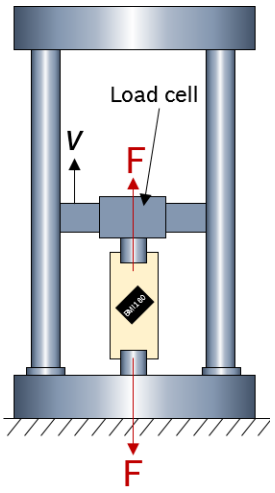

Figure 10.6: Tensile test setup

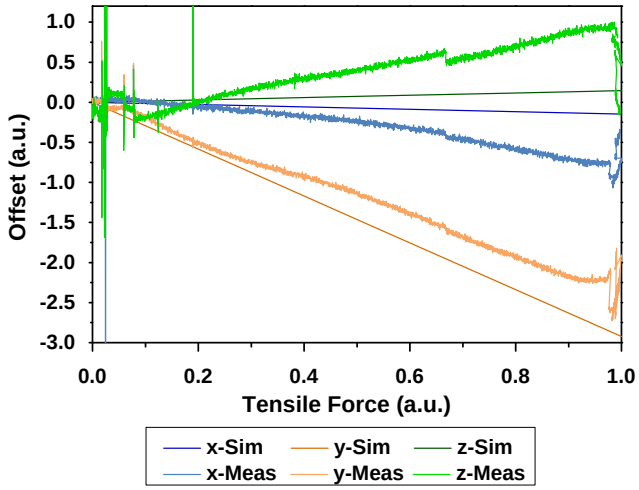

Figure 10.7: Simulated and experimental offset of BMI160 soldered onto a foil with external tensile force

10.2.3 Bending Test

To study the reliability during bending for each adhesive material on COF, a bending test of BMI160 sensors assembled onto a flexible PI foil was conducted. The flexible boards were designed via Altium PCB design program (Altium Limited, San Diego, California) as shown in fig. 10.8. Eight BMI160 sensors were attached at one end at four different orientations. A multiplexer enabled communication with multiple sensors. Communication with the sensors was achieved through SPI (serial peripheral interface) with a Raspberry Pi, according to the master-slave principle. The three common lines are SCLK (serial clock), MOSI (master output slave input), and MISO (master input slave output). The fourth line is CS (chip select), which is forwarded by the multiplexer to one of the eight sensors. The BMI160 communicates with the master if there is a falling edge on the CS line and communication is terminated on the rising edge.

To study the reliability of the interconnects under bending stress, a flex measurement system shown in fig. 10.9 was utilized. The machine is composed of a cylinder onto which the flex-boards are attached to and the cylinder is rotated, subjecting the boards to bending stress. The cylinder is rotated 360° and the process is repeated until the interconnects are

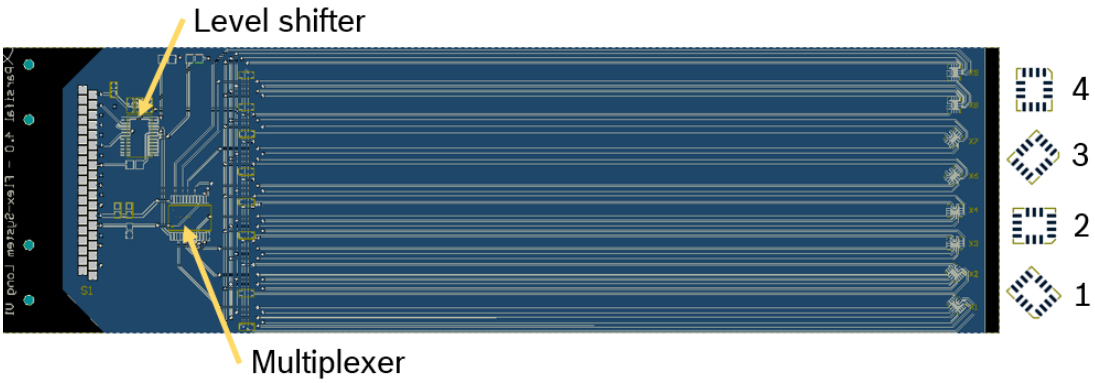

Figure 10.8: Flexboard design layout

broken, resulting in loss of signal from the sensors. With each cycle, a sine curve is fitted as seen in fig. 10.11, from which the offset and sensitivity of the sensors are calculated. The resulting values are compared to observe any drift in the measurement results, which may occur due to stress inflicted onto the MEMS core. Fig. 10.12 is an example of a BMI160 soldered onto a PI foil. The BMI160 is not expected to show any significant drift in offset or sensitivity due to its rigid packaging, but for a flexible embedded sensor, this effect may be more noticeable.

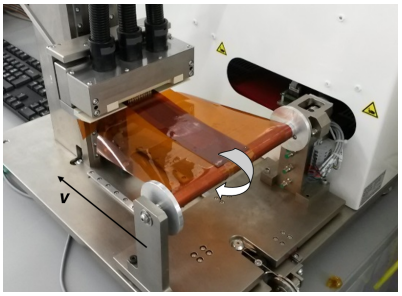

Figure 10.9: Flex measurement system for bending test

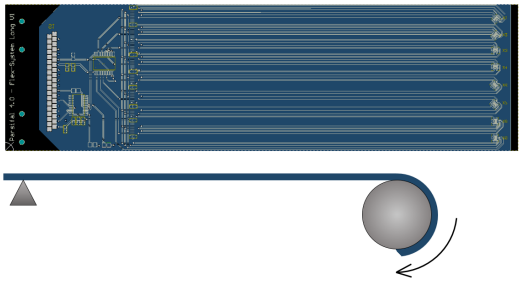

Figure 10.10: Schematic of direction of rotation of a board on flex measurement system

Fig. 10.13 shows the number of bending cycles until failure with sensors assembled with solder and ACF at four different orientations. For each interconnect material, two flexboards were assembled, translating to four sensors for each orientation. ACA 1 and 2 were not analyzed due to their excessive processing time. ACF 4 was assembled, but the reliability was too low, with 78% of the sensors not giving valid signals. ICAs performed

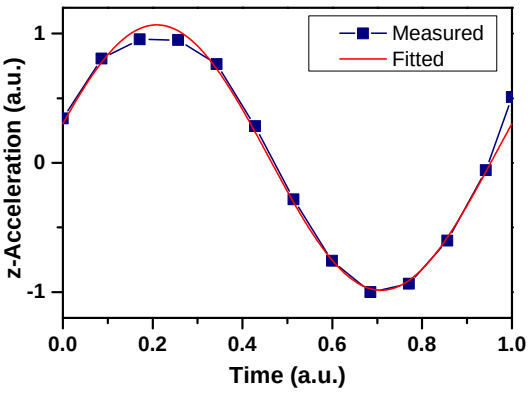

Figure 10.11: Sine fit curve of acceleration in z-direction for one cycle

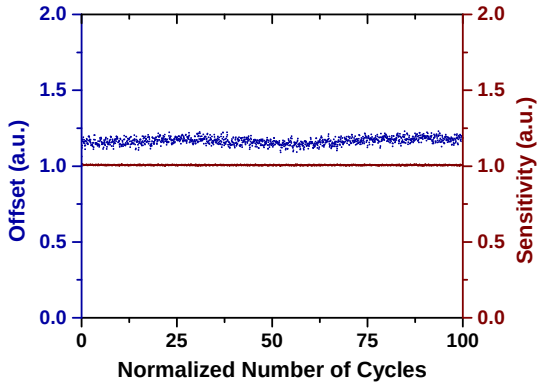

Figure 10.12: Offset and sensitivity of a soldered sensor over cycles

poorly, possibly attributed to their poor adhesion to the boards and brittleness due to their high composition in conductive particles.

The number of bending cycles given in fig. 10.13 and fig. 10.15 are normalized to the average number of bending cycles until failure for solder, as solder is used as our reference. As it can be observed in fig. 10.13, the influence of orientation is clear on solder and ACF. Sensors with a tilted orientation with respect to the board results in a higher reliability and the lowest reliability is shown in the second orientation for all materials. The pads on the outer edges of the sensor in orientation 2 have the longest distance from the bending axis, resulting in higher deformation of the pad area and earlier failure. Comparing orientations 1 and 3 in fig. 10.14(a) and (b) respectively, it can be observed that the improved performance in orientation 1 is due to the function of pads on the outer edge. For orientation 1, pads 4 and 11 lie on the outside and fail the earliest. These correspond to INT1 and OSDO pads, which are not used during communication with sensor. Orientation 3 has pads 1 and 8 on the outer edge, which are SDO and VDD respectively and are essential for sensor communication. This exemplifies that the location of pads with essential functions with respect to the bending axis should be taken into consideration when designing sensors for chip-on-flex technology. By simply placing the pads with essential functions close to the bending axis and the dummy pads on the outer edge, reliability of sensors can be improved.

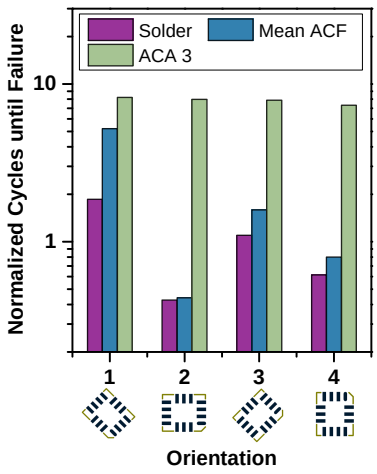

Figure 10.13: Bending reliability of solder and ACF according to orientation

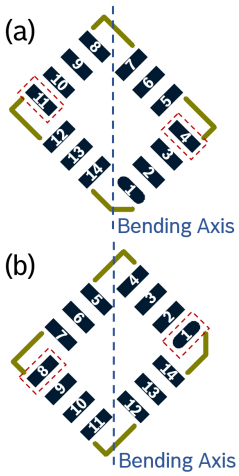

Figure 10.14: Pads for BMI160 (a) Orientation 1 (b) Orientation 3

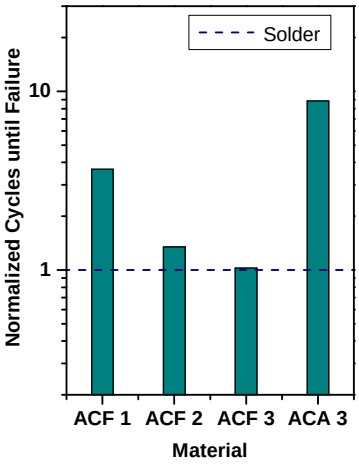

Figure 10.15: Bending reliability of chosen interconnect materials

ACA 3 showed no significant influence of orientation on the bending reliability and also displayed the highest number of cycles until failure, about a factor of 10 higher than that of solder, as seen in fig. 10.15. This may be attributed to the higher flexibility of the adhesive and the meniscus around the sensor as seen in fig. 10.16, leading to a higher area of contact in all directions compared to film or solder. This allows for higher deformation in all directions without losing connection.

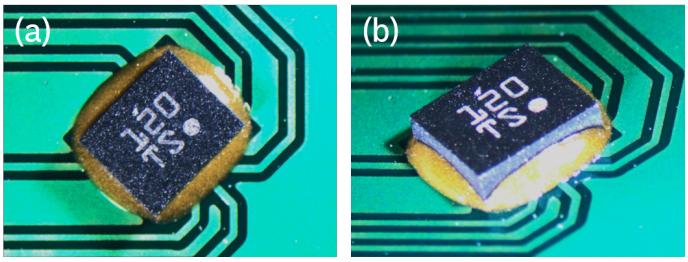

Figure 10.16: Sensor assembled with ACA 3 (a) Top view (b) Side view

For the anisotropic interconnects, processing pressure was varied to detect any influence of pressure on mechanical reliability. Boards were assembled with the lowest and highest recommended processing pressure given by the material data sheets. For ACA 3, reliability improved by a factor of 2.74 with higher pressure, and ACF 1's reliability also increased by a factor of 1.84. ACF 2 and 3 showed no improvement in bending reliability with higher

processing pressure.

After the bending tests, a few of the flexboards were cut into cross sections to analyze failure modes. The process of sectioning the boards was done by RoodMicrotec (RoodMicrotec GmbH, Stuttgart, Germany). Two flexboards with solder and two flexboards with ACA 3 were analyzed. The location of lines onto which the cross sections were sliced are shown in fig. 10.17. Observing pads 1 to 4 in fig. 10.19(b), where pad 1 is located on the center of the sensor, pad 1 remains as a reliable connection and the cracks become more visible, until the largest crack in pad 4. It can be observed that the pads on the outer edges with respect to the axis of rotation are the most strained, confirming the influence of orientation seen in 10.2.3. Voids in solder, as seen in pad 3, can be a cause of early failure.

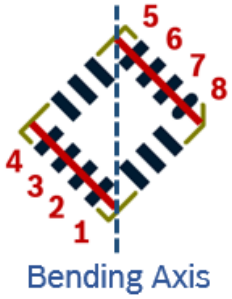

Figure 10.17: Location of slice for cross section views of sensors on flexboars

The cross sections of the sensors adhered with ACA 3 are shown in fig. 10.20, and it can be observed that the effect of orientation is not as significant. The metal particles within the adhesive matrix are visible and connection is lost when the adhesive is stretched far enough for the metal particles to lose connection with the pads. Effects of delamination, as seen in fig. 10.18, will lead to an earlier failure.

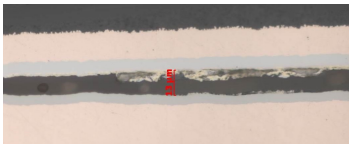

Figure 10.18: Cross-section view of delaminated ACA from pad [78]

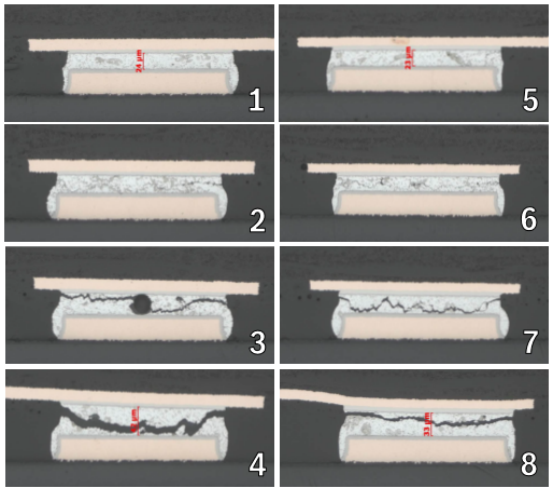

Figure 10.19: Cross-section view of soldered pads [78]

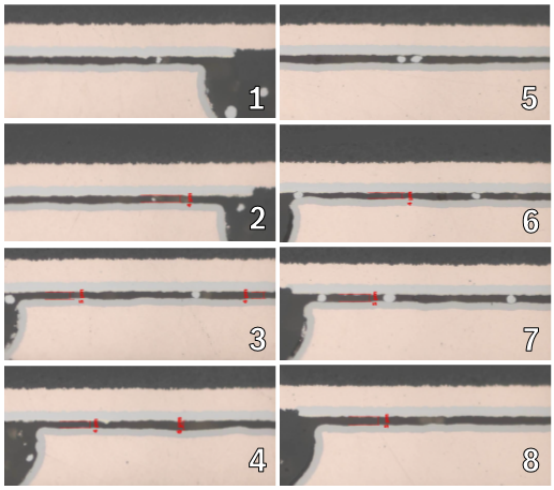

Figure 10.20: Cross-section view of pads assembled with ACA 3 [78]

CHAPTER 11

CHIP-IN-FLEX

Chip-in-flex, or CIF, is the technology of embedding sensors directly into flexible mold or foil. We explored the option of using flexible molds to package ASIC and CMA attached to a flexible board. The ASIC and CMA are connected to each other and the board via wire bonds and the system is molded in a flexible material as shown in fig. 11.1(a). The system has a LGA package and layout as can be seen in fig. 11.1(b) and will be referred to as FlexLGA. The process for fabrication is outlined in fig. 11.2, which will be described in detail in the coming sections.

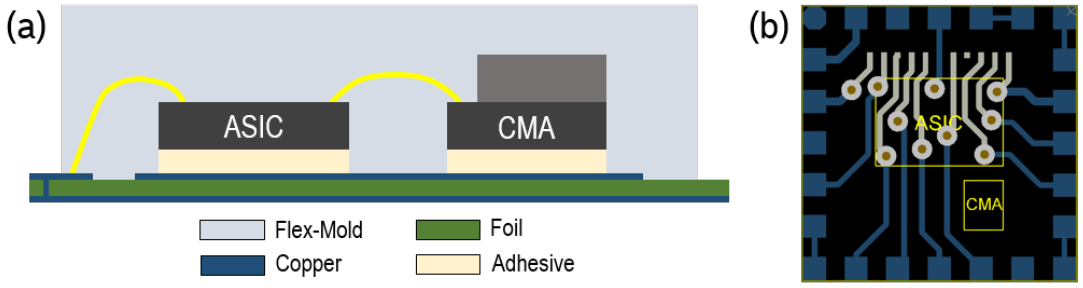

Figure 11.1: (a) Schematic of FlexLGA assembly (b) FlexLGA board circuit layout

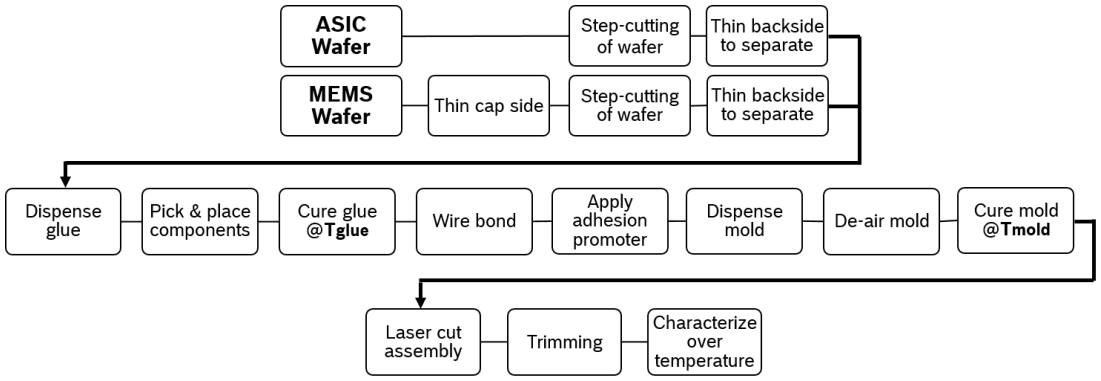

Figure 11.2: Outline of FlexLGA fabrication process

11.1 Sensor Performance of Thinned Chips

The first step of achieving FlexLGA is to thin down the components to achieve flexibility. The wafers are step-cut in rows and columns at the size of the individual chips, then the chips are backgrinded to be thinned and release the pieces. The ASIC undergoes back-grinding, while the CMA is ground at the cap and substrate. As can be seen in fig. 11.3, CMAs of various cap and substrate thicknesses have been characterized to study the effect of stress due to grinding and possible chipping of the chips.

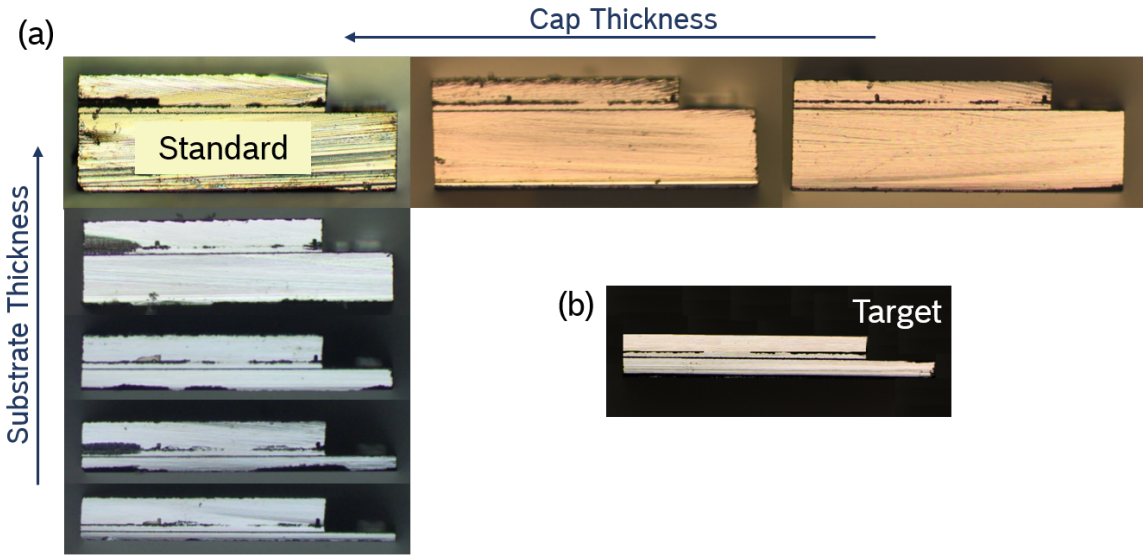

Figure 11.3: (a) Side views of thinned CMAs with a range of cap and substrate thicknesses (b) Side view of a CMA with target cap and substrate thickness

The chips were characterized with the rotary chamber measurement system (RCMS), as shown in fig. 11.4(a). The boards as shown in fig. 11.4(b) are placed on sides of a cube inside an oven and the cube is rotated at three different orientations at temperatures cycled from -40 to +85°C. With each orientation, the offset and sensitivity are calculated from the measured data versus the known acceleration from the Earth's gravitational field. The performance of the sensors is characterized through offset and sensitivity drift according to temperature.

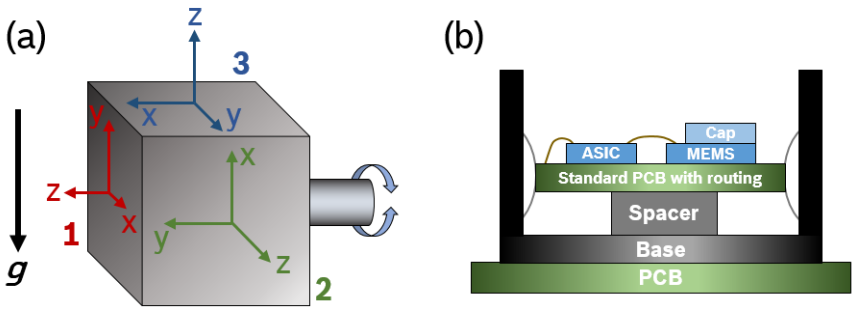

Figure 11.4: (a) Working principle of RCMS (b) Schematic of board to be placed inside RCMS for analysis

The offset and sensitivity temperature drift measurements for varying cap and substrate thicknesses are as reported in fig. 11.5. The thicknesses are normalized by the standard CMA thicknesses. The maximum change in offset and sensitivity over the change of temperature is measured for each axis to find the temperature drift in offset (TCO) and sensitivity (TCS). There exist large deviations in offset in each axis due to chipping and placement of the components onto the substrate, which may be not completely planar, therefore it was decided that the mean value of all axes is a better measure of comparison.

$$TCO = \Delta O/\Delta T \tag{11.1}$$

$$TCO_{mean} = \sqrt{TCO_x^2 + TCO_y^2 + TCO_z^2} \tag{11.2}$$

$$TCS = \Delta S/\Delta T \tag{11.3}$$

$$TCS_{mean} = \sqrt{TCS_x^2 + TCS_y^2 + TCS_z^2} \tag{11.4}$$

The TCO and TCS of BMI160 is specified as 1 mg/K and 0.3 mg/(g*K) respectively for each axis [55], translating to 1.73 mg/K and 0.520 mg/(g*K) mean TCO and TCS through equations 11.2 and 11.4. The substrate thickness has a much more significant effect on the performance of the sensors, which is as expected since it leads to a direct application of stress onto the MEMS structure, compared to the cap. At the target substrate thickness, the mean TCO increased by a factor of 8.90 compared to the BMI160 specified value and the mean TCS by a factor of 1.16. At the target cap thickness, the mean TCO is a factor of

2.02 higher than specified and the mean TCS is smaller than the specified value, at a factor of 0.373. All sensors are found be functional, but there is a strong influence on sensor performance, especially the offset drift.

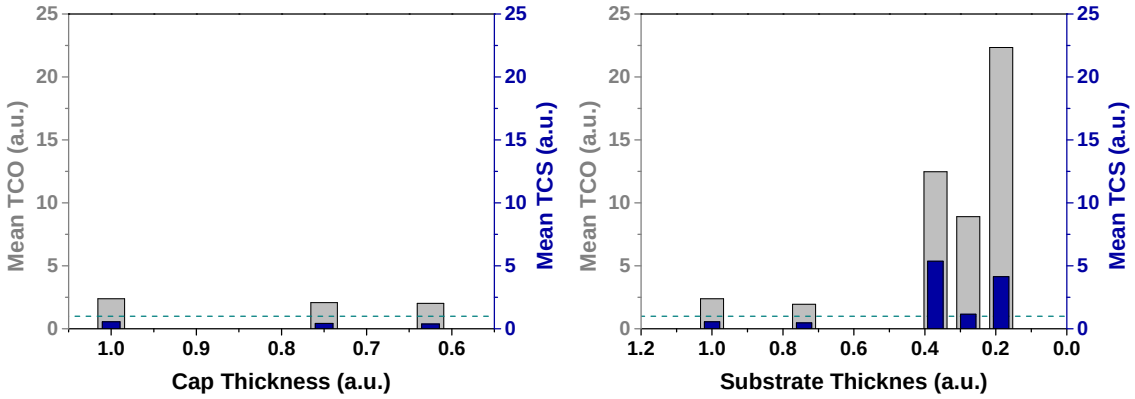

Figure 11.5: Influence of cap and substrate thicknesses on offset and sensitivity

11.2 Development of Embedding Process

The FlexLGA foil circuit layout is first produced on a larger foil with layout of 7 x 14 sensors, as shown in fig. 11.6. As previously shown in fig. 11.2, adhesive is first dispensed onto the areas where the components are placed. The single dies are picked and placed, then the glue is cured. The CMA and ASIC are wire bonded to each other and the pads on the foil, then an adhesion promoter is applied onto the foil. The molding is achieved through a dam and fill process, which consists of building a boundary around the chip and filling the volume with a material. A dam is placed around the whole foil into which the mold material is dispensed. The final steps are laser cutting the large foil into individual pieces. The black area surrounded by a red dashed box in fig. 11.6 is an area for one individual sensor. For the purpose of developing a robust embedding process of dam and fill, we explored a range of dam, foil and mold materials and their compatibility with each other.

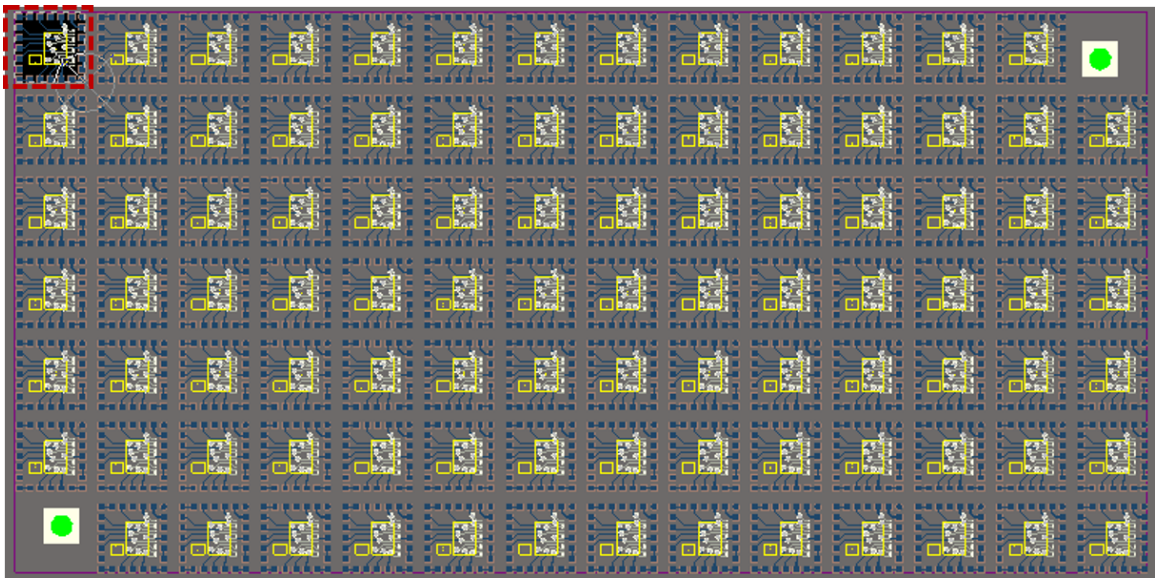

Figure 11.6: Large foil layout utilized for assembly of FlexLGA

11.2.1 Mold Material Characterization

A benzocyclobutene (BCB) and three silicone encapsulant materials were considered for the flexible mold. The ideal materials would be soft enough to be flexible, while being hard enough to maintain shape and durability, and have a coefficient of thermal expansion similar to the silicon components, foil and adhesives in order to minimize issues with thermal mismatch. The material properties of the encapsulants are as listed below on tab. 11.1. BCB was chosen for its low coefficient of thermal expansion (CTE), as well as low moisture absorption, excellent planarization and applicability with semiconductor processes. However, the high Young's modulus of the material will not allow absorption and compensation of stress caused by CTE mismatches inside the package. Three silicones were chosen, and the first had the advantage of being able to achieve a range of hardness by adjusting mixing ratio and relatively low CTE compared to the other silicones. The second silicone has a relatively higher CTE, but it has a low moisture absorption and the curing temperature is adjustable to be lower as low as room temperature given a 48-hour curing time. The last silicone boasts the lowest processing temperature, but the low hardness may be a concern for protection of the components inside the mold.

Table 11.1: Material properties of flexible mold encapsulants

Material	Shore Hardness A	Equivalent Young's Modulus (MPa)	CTE (ppm)	T_{mold} (°)
BCB		2900	42	250
Silicone 1 (1:1)	48	2.279	260	150
Silicone 1 (2:1)	33	1.294	260	150
Silicone 2	43	1.899	340	150
Silicone 3	12	0.4721	342	100

Two types of foil materials were considered: polyimide (PI) and liquid crystal polymer (LCP). PI foil is the established technology most widely used in flexible electronics at the moment. LCP film is increasingly becoming the alternative for the traditional PI films due to several advantages, as listed below. [79]

1. LCP has a lower dielectric constant and dissipation factor than PI, allowing for a larger range of functional frequency range from 1 kHz up to 45 GHz. LCP films can have metal trace signals places closer together with minimal crosstalk.
2. LCP films are less prone to moisture absorption issues associated with high temperature, such as evaporation, blistering, delamination, metal corrosion and via oxidation.
3. LCP films hold dimensional stability better in high humidity environments.
4. LCP is suitable for aggressive environments due to their high levels of solvent and chemical resistance.
5. Unlike PI, LCP is a thermoplastic material, which means that it does not cure or set when heated. It can be melted and laminated directly to copper foil and stiffeners, allowing for more methods of circuit construction.
6. The thermal expansion of LCP is linear to temperature, while PI foil changes its coefficient of thermal expansion below and above glass transition temperature.
7. LCP has a unique internal stress relief mechanism, undergoing a rapid ester interchange between chains at high temperature, limiting the interfacial stress build-up.

However, PI film possesses certain advantages, such as higher mechanical strength and

toughness, as well as a higher temperature resistance.

To compare the adhesion of encapsulant materials on the foils, a T-peel test was conducted. T-peel test is typically used to measure the peel strength of two flexible materials that have been bonded together. A flexible adhesive bond in this case refers to one that bends through 90° without breaking or cracking [80]. Flexible mold materials were cured onto equal bonding areas between two layers of PI or LCP foil with the FlexLGA layout shown in fig. 11.1(b). The specimen is placed into a tensile force tester, with one substrate pointed up while the other points down so that the bonded area sticks out horizontally and the entire setup forms a T-shape, as shown in fig. 11.7. Fig. 11.8 shows the raw data of a peel test conducted with silicone 2 on PI foil and the peel strength is determined as the average load per unit width of bond line required to separate the bonded layers. It can be observed that there are sudden jumps in the curves, which correlate to the location of the copper traces across the layer.

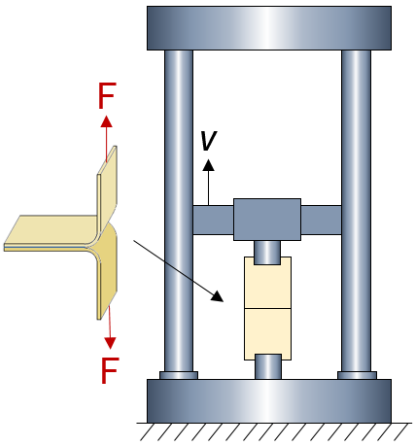

Figure 11.7: Peel test setup

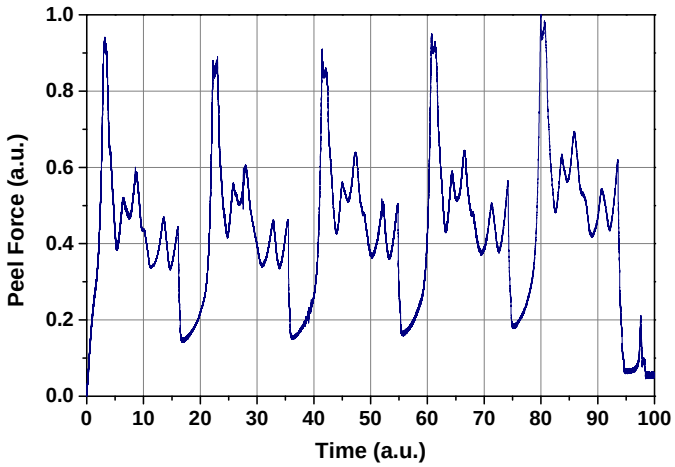

Figure 11.8: Peel test results for silicone 2 on PI foil

Fig. 11.9 shows the mean peel strength for each material, and it can be observed that the materials overall have a higher adhesion to the LCP foil than the PI foil. BCB showed the highest adhesion on LCP foil, while silicone 2 performed better on PI foil. The mean peel strength of silicone 2 on PI foil with and without an adhesion promoter can be seen in fig. 11.10, and it is revealed that the peel strength can be increased by a factor of 1.61 by

applying an adhesion promoter to the surface.

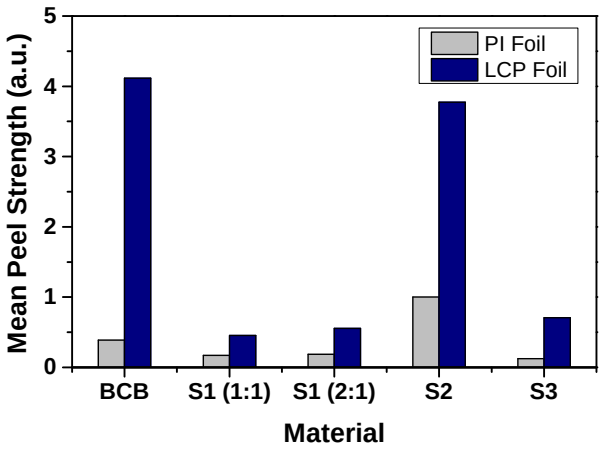

Figure 11.9: Mean peel strength of mold materials on PI and LCP foils

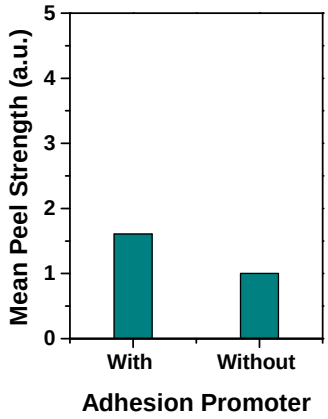

Figure 11.10: Mean peel strength of silicone 2 on PI foil with and without adhesion promoter

11.2.2 Finite Element Analysis

Mismatch of coefficients of thermal expansion of materials and subsequent warpage of the system should be considered when embedding sensors into flexible molds. Due to the varying CTE in the board, silicon structures, and mold encapsulants, there is a stress and subsequent strain that occurs in the system through expansion and compression of the materials during gluing, molding and subsequent cooling processes. To account for the possible influence of the process on the MEMS core, the gluing of the CMA and ASIC, as well as molding the encapsulant, for the FlexLGA was simulated through ANSYS. The model consists of the foil, silicon components for the ASIC and CMA with the target thicknesses for cap and substrate, adhesive material, and the flexible mold. The ASIC and CMA are modeled inside the flexible mold as shown in fig. 11.11. The model is sliced to ensure uniform meshing and meshed as shown in fig. 11.12. Mesh convergence was achieved to ensure a balance between processing time and accuracy of results (see Appendix C).

As it can be seen in fig. 11.13, the model is simplified to exclude the structure of the accelerometer in the MEMS core. Referred to as submodeling, this is a method of FEM

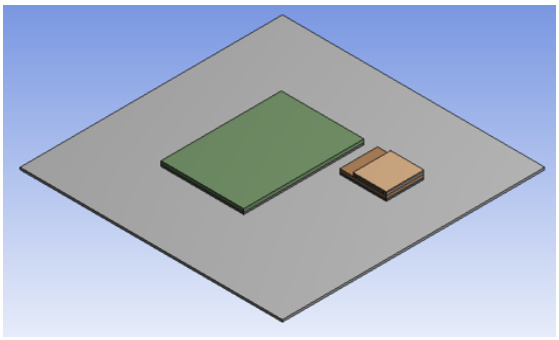

Figure 11.11: FEM model of assembled FlexLGA without mold

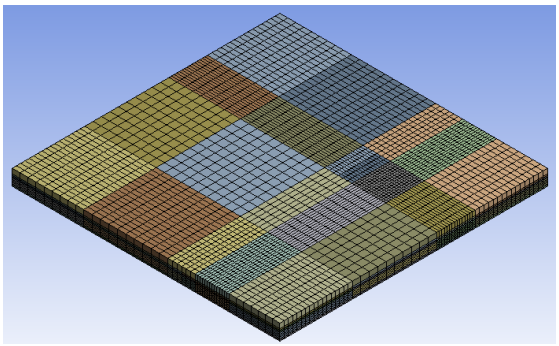

Figure 11.12: Meshed FEM model of FlexLGA

simulation which enables critical areas of a model to be viewed in a separate simulation with much finer mesh with the boundary conditions simulated from the global model. This is only applicable if the local geometry has little influence on the global stiffness. For the present case, the accelerometer structure has no influence on the elements in the MEMS core, but the deformation of the sensor core significantly influences the sensor structure. Therefore, the sensor structure is neglected in order to reduce complexity in the model. The results of the global simulation is utilized to analyze the submodel through a Bosch internal tool. A typical simulation process consists of the following steps:

1. The system is modeled through ANSYS with points of interest on the MEMS core.
2. A macro within the ANSYS postprocessing reads out the deformation of the sensor plane and writes it into a text file.
3. This deformation is polynomial fitted in the tool and multiplied by the vulnerability of the sensor.

The boundary conditions for the simulation include point A shown in fig. 11.13 at the center of the CMA core as a fixed point in all three spatial directions. Point B is free to move in the x-direction, but constrained in y and z-directions. This limits the rotation about the y- and z-axes. Point C is only fixed in the z-direction and prevents the system from rotating about the x-axis.

Fig. 11.14 outlines the process of the simulation from the gluing of the components

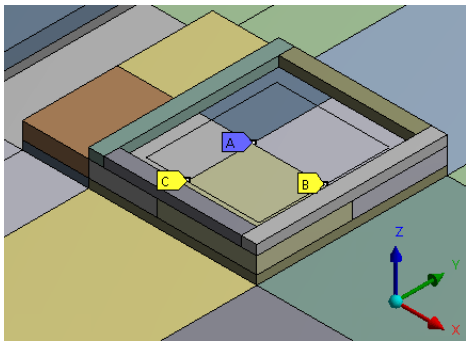

Figure 11.13: FEM model of the CMA structure with points for boundary conditions

onto the foil to the molding of the flexible encapsulant. Step 1 begins at room temperature with all materials having the same CTE as silicon. At this step, the foil and the silicon components are ”alive”, but the glue and the mold are ”killed”. This means that the elements are deactivated by multiplying their stiffness by a severe reduction factor, 1.0^{-6} by default [81]. Aiming to imitate the behavior of materials at higher temperatures where materials behave with low viscosity, there will be no change in stress or displacement in the killed elements. The temperature is then increased to the gluing temperature in step 2, but the reference temperature for the thermal expansion is also changed to the gluing temperature for the glue and the foil. The CTE of the glue is changed to its own CTE value. At step 3, the glue is alive. Only a minimal change in stress or displacement is seen here at the higher temperature of T_{glue} as expected. Step 4 begins the cooling down to the room temperature and the effect of thermal mismatch is finally seen here. It can be observed that as the temperature is decreased, there is a downwards warpage in the overall system due to the thermal mismatch between the silicon and the foil. Compared to the silicon and glue, the foils have higher CTE, as seen in tab. 11.2. Therefore, there is a warpage downwards as the foil contracts more than the silicon or glue.

Table 11.2: Young’s modulus and CTE of components in FlexLGA

	Silicon	**PI Foil**	**LCP Foil**	**Adhesive**
E (GPa)	169	7.10	4.15	0.300
CTE (ppm)	2.3	25 ($T < T_g$), 40 ($T > T_g$)	18	150

Starting from step 5, the process is repeated for molding. The applied temperature is increased to the molding temperature and the reference temperature for the foil, glue and mold is also changed to the higher molding temperature. The elements for the mold component are still killed at this step, but the CTE is changed to its designated property. At the next step, the mold material comes alive with the temperature still held at the molding temperature. It can be observed that the displacement of the system is decreased again as there is no thermal mismatch between the materials due to the reference temperature being held at the molding temperature. As the final step, the applied temperature is again decreased to room temperature to imitate the cooling of the system. There is an observable curvature upwards in the final solution, due to the higher CTE of the mold than the silicon or foil.

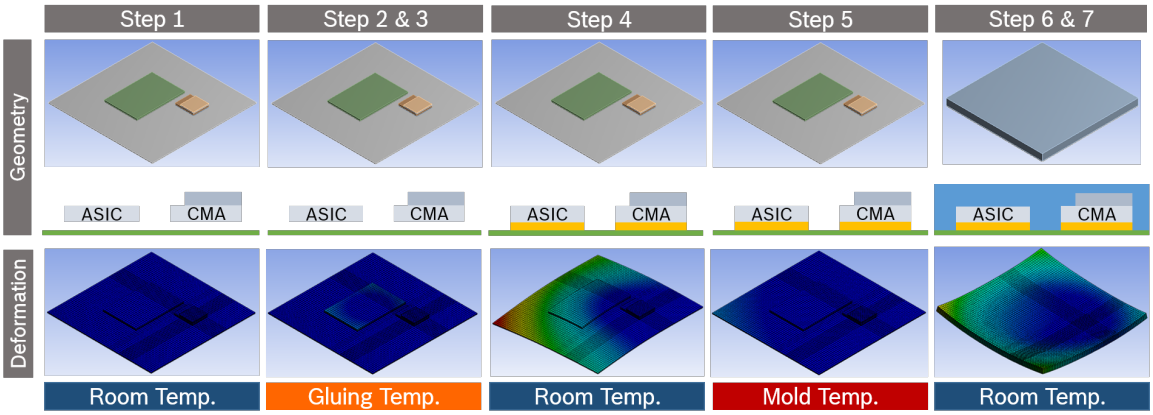

Figure 11.14: Simulation process for FlexLGA (2.1x scale)

The results of the simulation and the subsequent macros are utilized to analyze the sub-model, the sensor structure. The deformation of the CMA core is inputted into a Bosch internal tool, which was developed to calculate the output signal of an electrostatic accelerometer due to external loads, including packaging effects, solder drift, bending or aging. The output signal is calculated by obtaining the deformation coefficient through decomposition of the finite element results by 2D polynomial fitting and multiplying the coefficients with the vulnerability. Vulnerability here is defined as the output signal due to

a given deformation component, and is characteristic to the design. The results file includes the offsets in each axis for each processing step, which are used to calculate the mean offset in all axes.

After the gluing step, the maximum deformation in the z-direction of the system on PI foil is 167% greater than that of the system on LCP foil. The CMA component glued onto PI foil is simulated to have an offset that is 175% greater than that of the component glued onto LCP foil. This is as expected from the smaller CTE of the LCP foil being closer to that of the silicon components, as well as the lower Young's modulus that allows the absorption of the stress due to CTE mismatch.

For the molding step, three different silicone materials and BCB were simulated with varying thicknesses. The maximum z-deformation of the system is shown in fig. 11.15. It was expected that the deformation would increase as the mold thickness increases due to the increased effect of thermal mismatch from the mold. However, it was observed that the deformation for the system molded in BCB increases at first and decreases again. The results of this simulation was confirmed by an analytical solution of the bi-material behavior of BCB and PI foil adhered together.

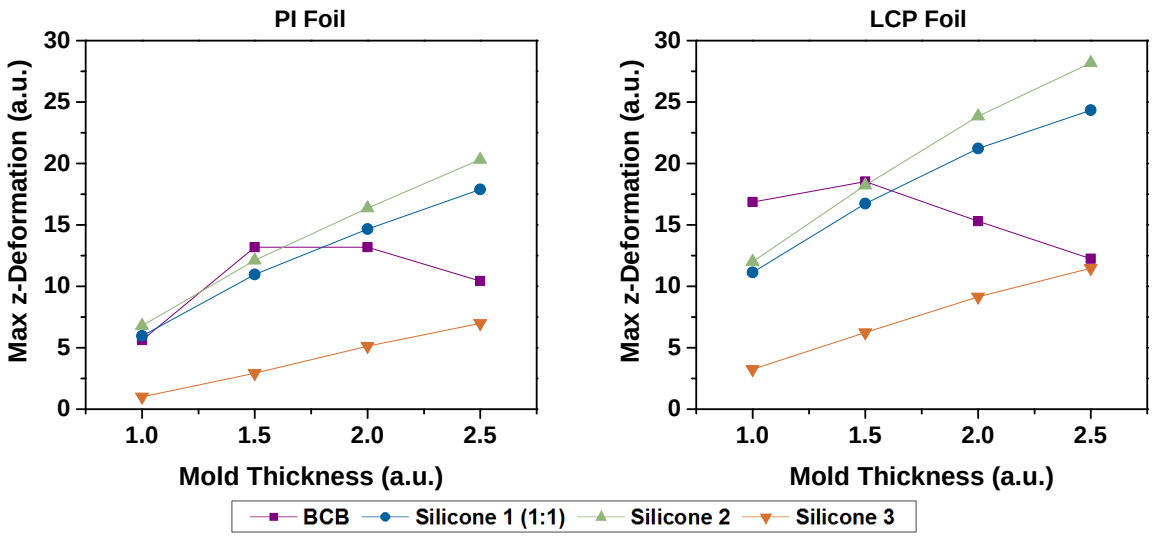

Figure 11.15: Simulated maximum deformation of flexLGA assembly in z-direction after molding process onto PI and LCP foil

When a component made up of two different materials bonded together is heated or cooled, a misfit is generated between the new dimensions each would adopt if they were isolated [82]. Curvature is defined by κ and the inverse $1/\kappa$ is the radius of curvature.

$$\kappa = \frac{6E_A E_B(h_A + h_B)h_A h_B \Delta\epsilon}{E_A^2 E_A^4 + 4E_A E_B h_A^3 h_B + 6E_A E_B h_A^2 h_B^2 + 4E_A E_B h_A h_B^3 + E_B^2 h_B^4} \tag{11.5}$$

$$\Delta\epsilon = (\alpha_A - \alpha_B)\Delta T \tag{11.6}$$

E_A and E_B are the Young's modulus of each material, and h_A and h_B are their respective thicknesses. The misfit strain $\Delta\epsilon$ is defined by the difference in CTE of each material, α_A and α_B, and the change in temperature, ΔT. As it can be observed in fig. 11.16, the radius of curvature initially decreases and increases after a certain thickness. As the BCB mold thickness increases, the stiffness effect of the mold takes over the CTE mismatch to lead to a lower curvature or a higher radius of curvature.

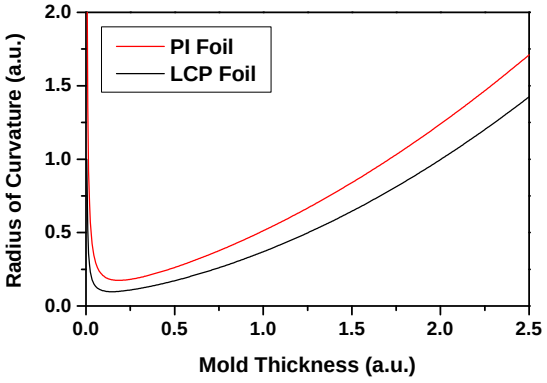

Figure 11.16: Analytical results of radius of curvature of BCB molded onto PI and LCP foil

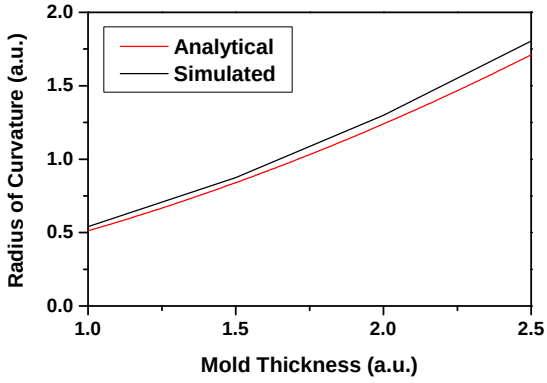

Figure 11.17: Comparison of analytical and simulated results of BCB molded onto PI foil

The resulting mean offsets for molded FlexLGA on PI foil and LCP foil are shown in fig. 11.18. As it was with the gluing step, there is a lower offset in the system when assembled onto LCP foil. The maximum warpage for each mold thickness, however, is higher for the LCP foil. This is attributed to the smaller CTE of LCP, leading to a higher

mismatch between the foil and the mold. BCB as the mold material leads to an offset that is an order of magnitude higher than for the silicones, even though it was seen that the warpage in the overall system for all materials was comparable.

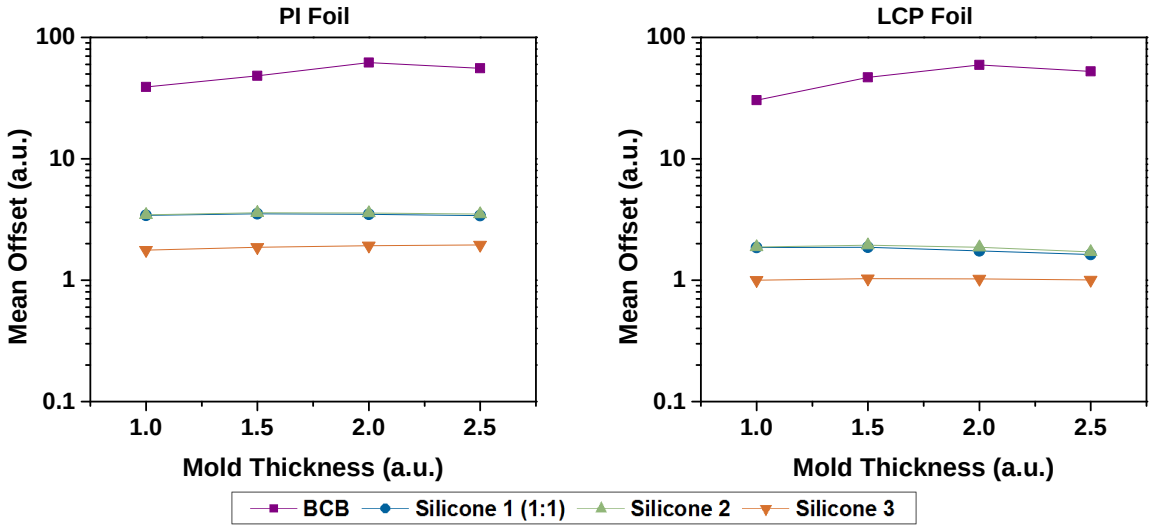

Figure 11.18: Simulated offset of CMA measurement after gluing and molding process of FlexLGA onto PI and LCP foil

Closing in on the CMA core, the maximum deformation at each thickness is shown in fig. 11.19 and the maximum stress in fig. 11.20. Although the warpage of the total assembly is comparable for all mold materials, it can be observed that the maximum stress in the core itself, and its subsequent deformation, is almost an order of magnitude higher for BCB than for the silicone encapsulants.

This is attributed to the high stiffness of the material. Even though the CTE mismatch is much lower for BCB than for the silicones, the significantly higher Young's modulus does not allow for the mold to compensate for any stress due to the warpage, directly applying the resulting stress to the MEMS core and causing deformation. This shows that the total warpage of the system is not a good measure of the sensor performance or the resulting offset, but the stress and deformation of the CMA core itself must be taken into account.

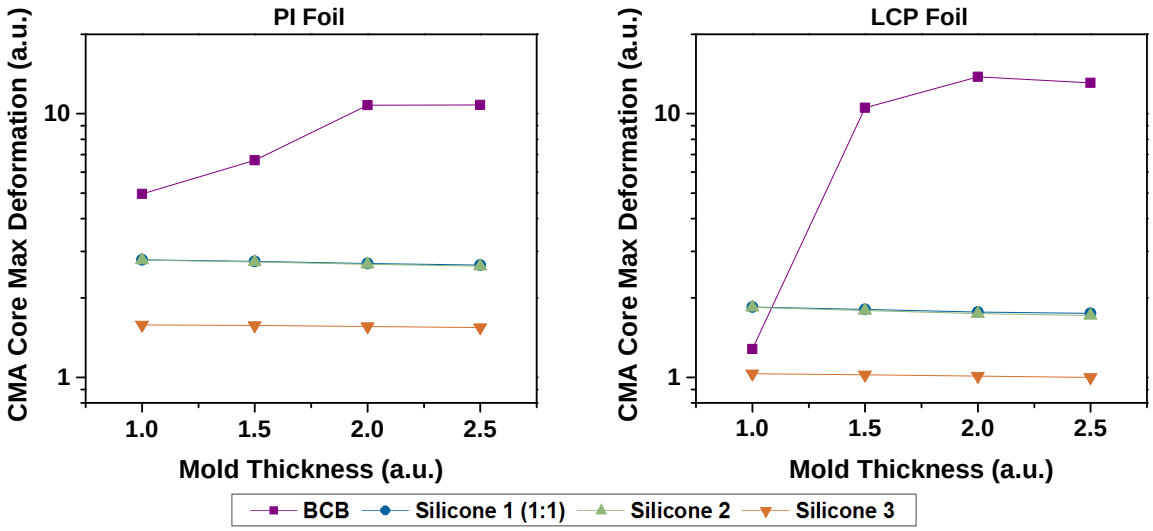

Figure 11.19: Simulated maximum deformation of CMA core after gluing and molding process of FlexLGA onto PI and LCP foil

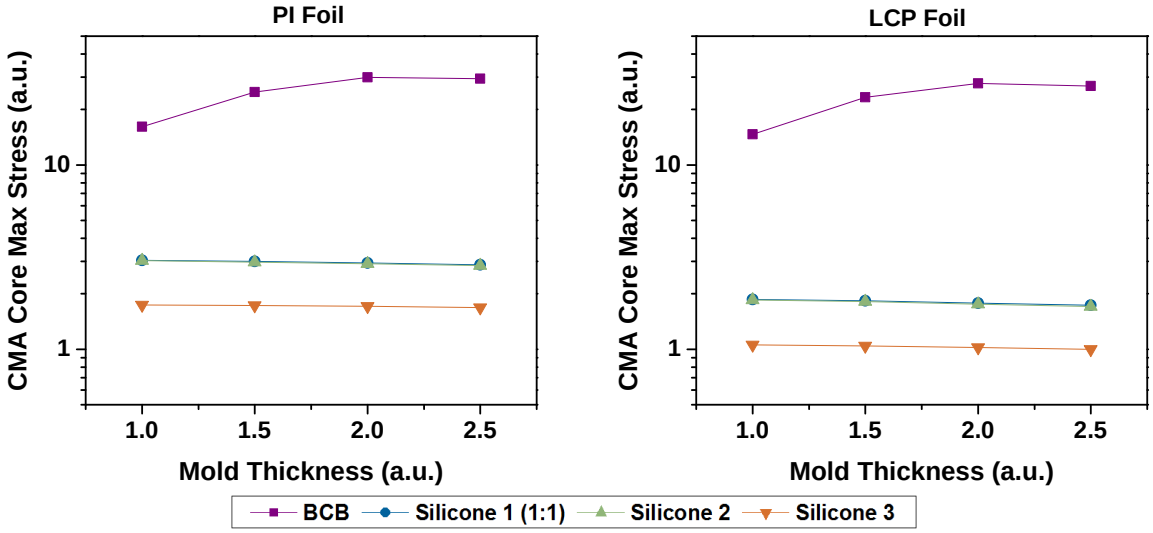

Figure 11.20: Simulated maximum stress of CMA core after gluing and molding process of FlexLGA onto PI and LCP foil

11.2.3 Process Development

Several issues arose during developing an assembly process, including wire bonding. Due to the flexibility of the foil as well as the close proximity of the pads and small pad areas, the wire bonding process proved to be immensely difficult. A thermosonic method was used for wire bonding, which combines ultrasonic energy, heat and force to bond wires

[83]. This process requires ultrasonic vibrations at the pads with the wires in contact, but the flexibility of the foil made it difficult for the vibrations to transfer and for the wires to be held stably at one position. It was determined that the process is easier if the wire bond height is higher to allow for the wires to adhere correctly to the pads. This value is higher than the target total assembly thickness, but it was necessary to bond the wires properly and an ICA was applied at the pads of the wire bonds to ensure electrical connection.

In developing the process for FlexLGA assembly, there were issues in properly dispensing and curing the mold materials due to the seepage of the material into the vias of the substrate foils. If placed onto a flat ceramic to dispense and cure, the materials bled through the vias in between the bottom surface and ceramic. It was determined that the best method of ensuring that the material does not seep through is to place the foil on another dam and avoid the bottom surface from touching any other surface to reduce the capillary effect of the material to travel through the vias and towards another surface (see fig. 11.21). Another observation to note is that if a tool is used after dispensing to flatten the material surface, it forces the material through the vias easily, therefore it is recommended to dispense without any additional handling of the material. Moreover, the adhesion promoter was best found to be applied with a Q-tip.

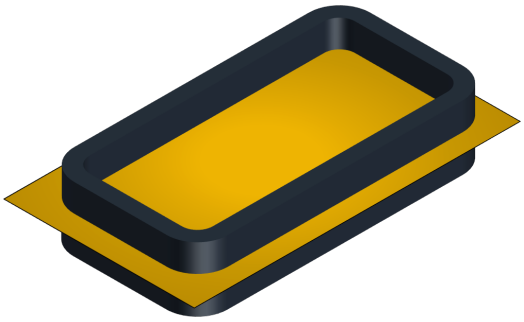

Figure 11.21: Foil placed in between two dams to avoid seepage of material through vias

Various dam and mold materials for the dam and fill process have been explored, as seen in tab. 11.3. Multiple dam adhesives were tested to ensure proper adhesion of the dam to the foil. The first adhesive led to an adhesion failure on Teflon. It was seen that

the second adhesive is prone to becoming liquid again during the mold curing process in the oven, leading to the glue running through the vias of the foil. Therefore, placement of a dam underneath the foil, as seen in fig. 11.21 is vital for the adhesive as well. BCB as the mold material was found to lead to fracture in the mold if Aluminum was used as the dam, as seen in fig. 11.22. Using Teflon as the dam material, BCB mold led to delamination or significant warpage due to the dam not being stiff enough to hold the foil to be flat. Using silicone as the dam material, BCB mold led to an even higher warpage, as seen in fig. 11.23. This was not as expected from the simulation results, but it should be taken into account that the simulation did not include any shrinkage effect. The silicones utilize platinum-catalyzed addition curing, meaning that there is no byproduct released and the silicones cure without shrinkage [84]. However, BCB possesses up to 5% shrinkage, meaning that the mold will inevitably shrink during the curing process, causing a higher warpage upwards.

Table 11.3: Development of FlexLGA embedding process

Foil Material	**Dam Adhesive**	**Dam Material**	**Mold Material**	**Result**
PI	Adhesive 1	Aluminum	BCB	BCB fracture
			Silicone 1	Low warpage
		Teflon	BCB	Adhesion failure
			Silicone 1	Adhesion failure
	Adhesive 2	Aluminum	BCB	BCB fracture
			Silicone 1	Low warpage
			Silicone 2	Low warpage
		Teflon	BCB	High warpage, dam delamination
			Silicone 1	Medium warpage
			Silicone 2	Medium warpage
	Silicone	Silicone	BCB	Extremely high warpage

Silicones as the mold material gave the most reliable results with the lowest warpage when used with Al dam. Silicones in Teflon dams resulted in a noticeable warpage, as can be observed in fig. 11.24. Silicone 3 proved to be too soft to touch with the consistency

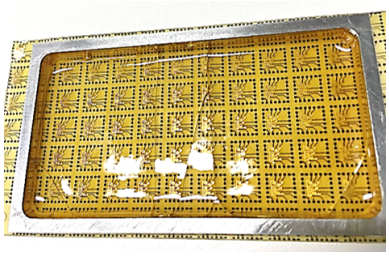

Figure 11.22: BCB mold cured in Al dam, resulted in fracture in mold

Figure 11.23: BCB mold cured in silicone dam, resulted in high warpage

being more of a gel rather than a solid. Out of the two remaining silicones, silicone 2 is a more attractive choice due to its performance in the peel test and low moisture absorption.

Figure 11.24: Silicone mold cured in Teflon dam

11.3 Evaluation of Samples

FlexLGAs with PI foil as substrate and silicone 2 as mold were assembled as shown in figs. 11.25. It can be observed that there is a noticeable warpage in the system with the corners pointing upwards, as shown in the simulations. The glue under the ASIC and CMA can be observed in white in fig. 11.26 and fig. 11.27. Air bubbles within the mold material are visible, due to air getting trapped under the small crevices near the wire bonds. Better de-airing process is required to prevent this. Around the edges of the FlexLGA, dust from lasering the assembly is visible in the close-up view of fig. 11.28. Although most of the dust has been removed through cleaning after lasering, some dust remains.

The radius of curvature resulting from the warpage of FlexLGA was calculated by measuring the displacement of the edges, as seen in fig. 11.29. The radius of curvature, given three points on the curvature $(x_1, y_1), (x_2, y_2)$ and (x_3, y_3), is given as eq.11.11. Fig. 11.30

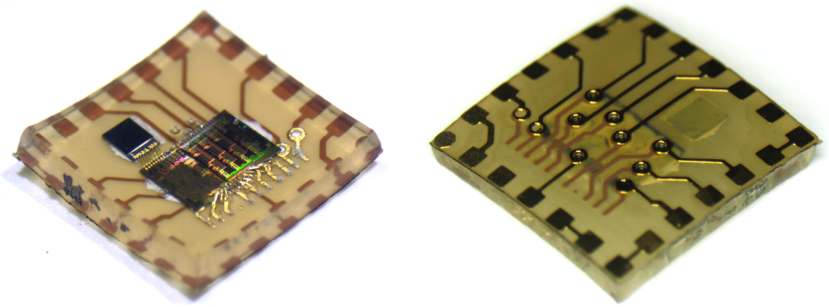

Figure 11.25: Side views of the molded FlexLGA on PI foil with silicone 2

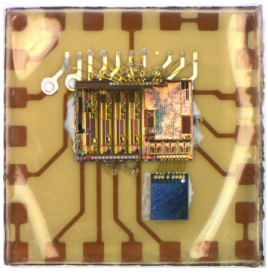

Figure 11.26: Top view of FlexLGA

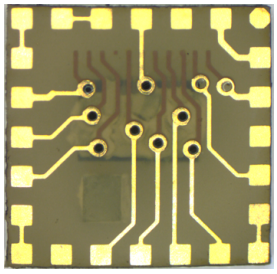

Figure 11.27: Bottom view of FlexLGA

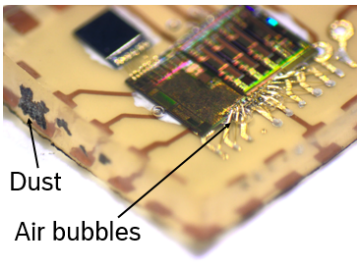

Figure 11.28: Close-up view of FlexLGA

is the radius of curvature according to the mold thickness for four FlexLGA samples. It can be observed that as the thickness increases, there is a decreases in radius of curvature or higher warpage, as seen in the simulations. Compared to a simulated model of FlexLGA with the same thickness, the measured radius of curvature was within 15.2% of the simulated value.

$$m_1 = \frac{\Delta y_{12}}{\Delta x_{12}} \tag{11.7}$$

$$m_2 = \frac{\Delta y_{23}}{\Delta y_{23}} \tag{11.8}$$

$$x_c = \frac{m_1 m_2 (y_1 - y_3) + m_2 (x_1 + x_2) - m_1 (x_2 + x_3)}{2(m_2 - m_1)} \tag{11.9}$$

$$y_c = -\frac{1}{m_1}(x_c - \frac{x_1 + x_2}{2}) + \frac{y_1 + y_2}{2} \tag{11.10}$$

$$R = \sqrt{(x_1 - x_c)^2 + (y_1 - y_c)^2} \tag{11.11}$$

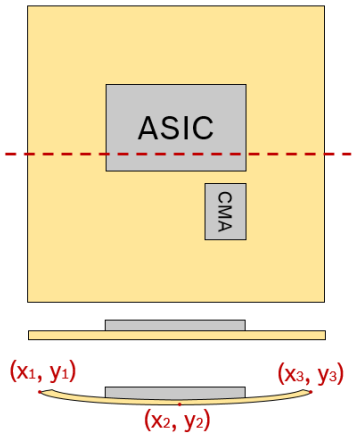

Figure 11.29: Measured points for radius of curvature calculation

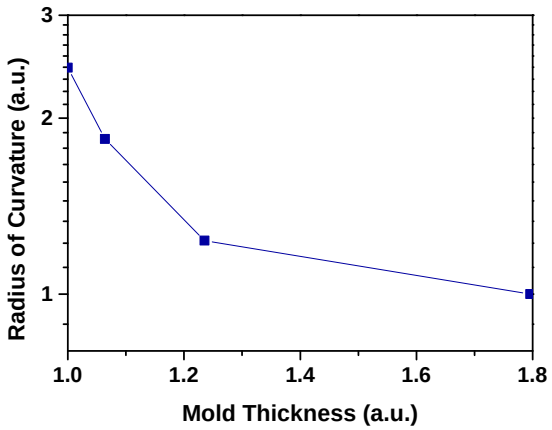

Figure 11.30: Radius of curvature of FlexLGA samples according to mold thickness

To evaluate the sensor performance, 19 sensors were placed into the RCMS with the sockets shown in fig. 11.31. Due to the sockets that close onto the sensors and apply pressure, the sensors were first trimmed to account for this pressure without thermal cycling.

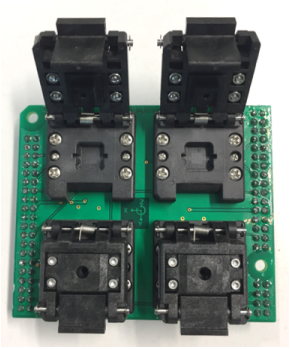

Figure 11.31: FlexLGA sockets used for placing the sensors into the RCMS

The sensors were again cycled from -40 to +85°C to evaluate the drift in offset and sensitivity due to temperature. The results shown in fig. 11.32 are normalized in the axis with the specified mean TCO and TCS values of a BMI160 as 1. It can be observed that all sensors are within the limits of the specified mean TCS and five sensors are within the specified value of mean TCO. The performance of the sensors are comparable to the BMI160, with the average TCO of all sensors being 34.0% greater than the specified value and the average TCS being 27.5% smaller than specified.

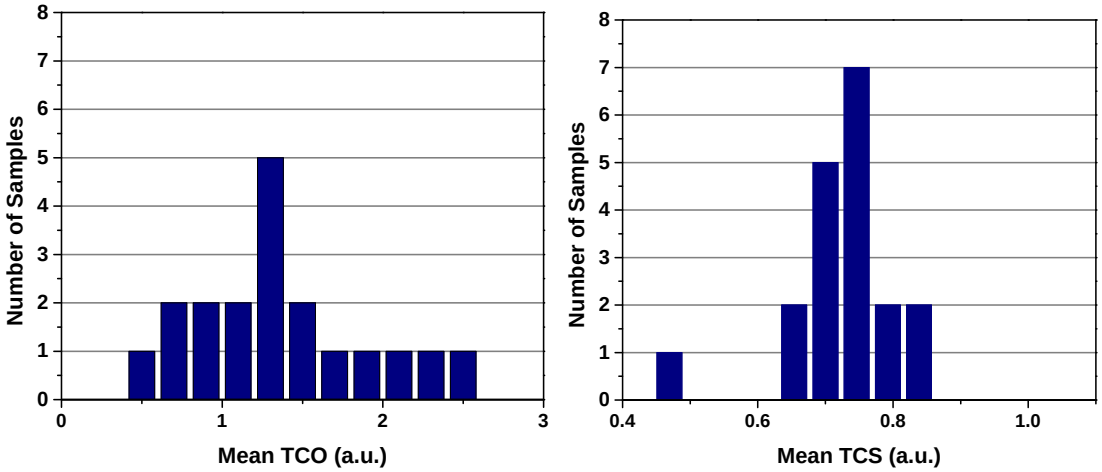

Figure 11.32: Histogram for the mean TCO and TCS values of FlexLGA samples on PI foil with silicone 2

CHAPTER 12
CONCLUSION

A short-term solution and a long-term resolution to the study of integration of MEMS accelerometers into flexible electronics were presented. The chip-on-flex technology aims to integrate silicon chips onto flexible boards through the use of advanced interconnect materials to mitigate the stress concentration at connection between foil and chip. The target interconnect materials were evaluated through electrical and mechanical characterization, to optimize the manufacturing process while ensuring performance reliability.

Chip-in-flex was presented to evaluate the possibility of integrating thin chips into flexible molds for further flexibility. The effect of grinding chips to thinner components was studied to ensure proper sensor performance. FlexLGA was developed as the system to integrate the thinned chips onto foils and molded with a flexible encapsulant. Geometry, material selection and manufacturing process were optimized through finite element analysis and experimental methods. FlexLGAs were assembled and tested to show comparable performance to a standard inertial sensor.

12.1 Future Research

FlexLGA assembly on LCP foil is still to be explored. The two technologies will be combined to test the effect of bending on offset and sensitivity measurements of the accelerometer in the FlexLGA. Further optimization of the manufacturing process, including reducing the processing time for wire bonds and minimizing warpage of the system, is necessary.

Appendices

APPENDIX A

PART I: MESH CONVERGENCE

The convergence parameters that are considered are electric potential and strain energy density for the single ceramic Y-poled case. It is assumed after careful observation of the mesh in ANSYS that if mesh convergence is achieved for the single ceramic Y-poled case that all other cases would follow similar trends for convergence.

The mesh convergence is achieved in two steps. The first is a line divide and the second is a refine mesh option. The whole system is meshed according to the line divide option and the piezoceramic elements, or the elements of interest, are refined in the mesh. In order to test the mesh convergence of each step, the line divisions are varied from 0.5 cm to 0.06 cm and the mesh refine options are evaluated at levels of 1 to 5.

The results of these processes can be seen in fig. A.1 and fig. A.2. It can be seen that the electric potential converges as well as the elastic strain energy density. Upon comparing the percent differences between the different refine mesh options it can be observed that refine 3 and refine 5 follow similar trends. Refine 3 is chosen as the optimal setting and mesh convergence is achieved at the 0.09 cm range.

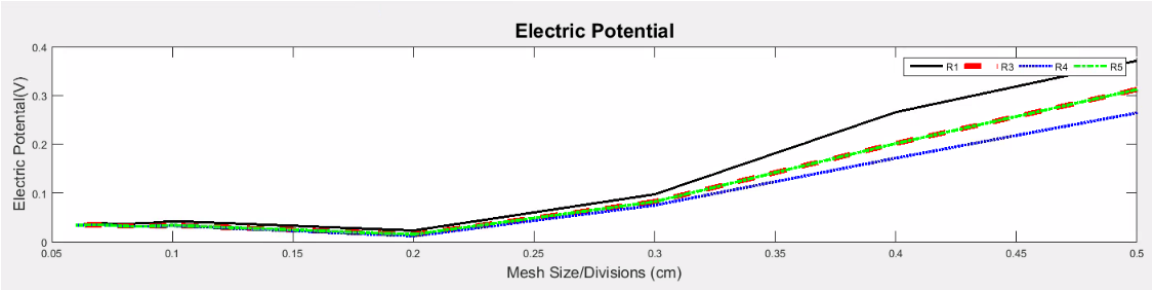

Figure A.1: Electric potential according to mesh size division and refinement

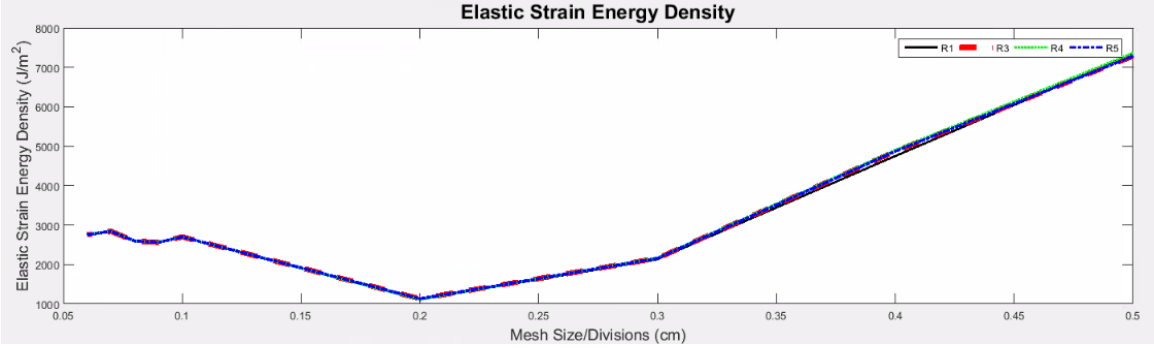

Figure A.2: Elastic strain energy according to mesh size division and refinement

APPENDIX B

PART II: LOAD ANGLE AND OFFSET

The offset of an accelerometer is strongly dependent on the sensor plane deformation. In addition, the CMA is not centered in BMI160, leading to a large influence of load angle on the sensor performance due to its asymmetrical design. To study this, a sensor is simulated to be placed centrally on a film substrate and rotated in 5° steps around the sensor axis, as shown in fig. B.1. The simulated offsets are shown in fig. B.2, with the highest offset values observed at approximately 45 and 135°.

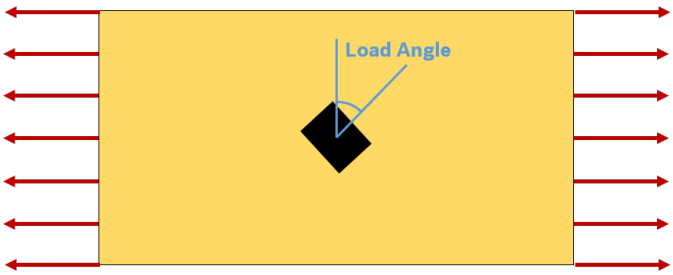

Figure B.1: Schematic of load angle variation for tensile force

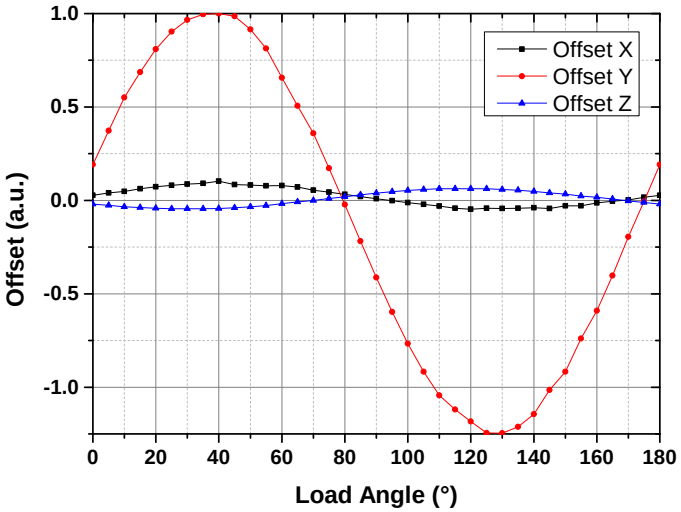

Figure B.2: Offset of each axis according to applied load angle of tensile force [85]

APPENDIX C

PART II: MESH CONVERGENCE

To ensure the mesh size of the simulation is small enough to achieve accurate results while minimizing the runtime, a mesh convergence study was performed. The mesh size was determined through element size of the bodies of CMA, ASIC, foil and mold, as well as the thickness edge sizing of each component, including the adhesive thickness. Fig. C.1 refers to the percentage difference from the values of the results from the smallest mesh size, referred to as mesh size 0. It was observed that the values reach a steady trend from mesh size 2 and on, therefore mesh size 2 was chosen as the optimal mesh size.

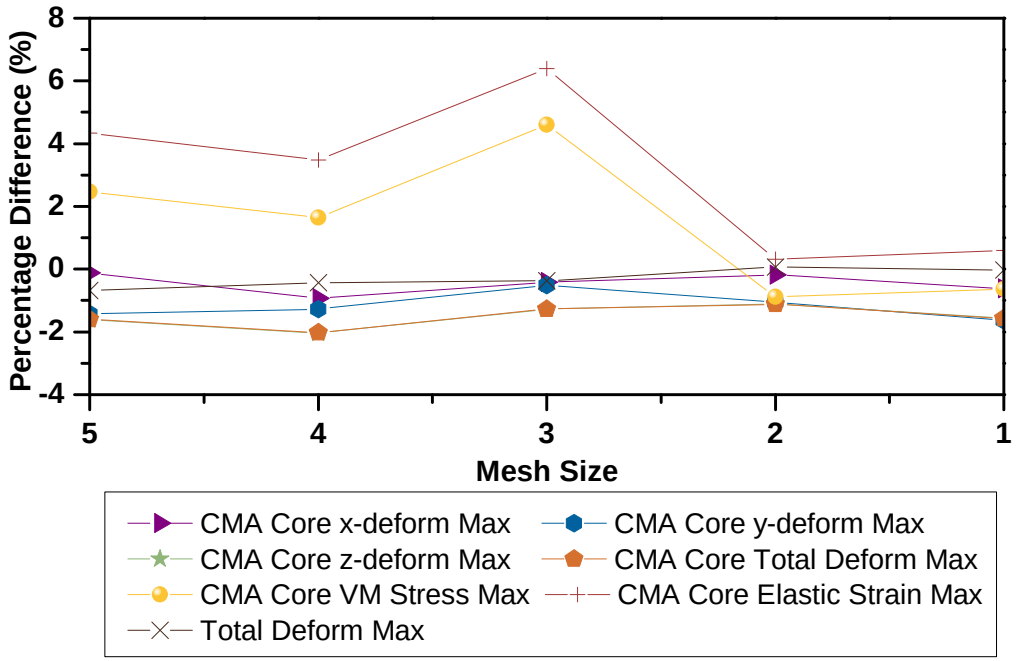

Figure C.1: Mesh convergence result for FlexLGA simulation

REFERENCES

[1] L. Kong, *Waste Energy Harvesting: Mechanical and Thermal Energies*. Springer Berlin Heidelberg, 2014.

[2] S. Beeby, M. Tudor, and N. White, "Energy harvesting vibration sources of microsystems applications," *Measurement Science and Technology*, vol. 17, R175–R195, Oct. 2006.

[3] T. Nguyen and M. Aiello, "Energy intelligent buildings based on user activity: A survey," *Energy and Buildings*, 2012.

[4] E. Park, N. Bassiri-Gharb, and I. Stern, "Coupling high resonant frequency piezoelectrics to human-scale frequencies for energy harvesting," *Procedia Computer Science*, vol. 109, pp. 771–776, 2017.

[5] C. Williams and R. Yates, "Analysis of a micro-electric generator for microsystems," *Sensors and Actuators*, vol. 52, pp. 8–11, 1996.

[6] Erturk, *Piezoelectric Energy Harvesting: Modeling and Application*. Wiley, John & Sons, 2011.

[7] Y. Jeon, R. Sood, J. Jeong, and S. Kim, "MEMS power generator with transverse mode thin film PZT," *Sensors and Actuators*, vol. 122, pp. 16–22, 2005.

[8] G. Lippmann, "Principe de la conservation de l'electricit," *Annales de chimie et de physique*, vol. 24, pp. 145–178, 1881.

[9] G. Haertling, "Ferroelectric ceramics: History and technology," *Journal of American Ceramics Society*, vol. 82, no. 4, pp. 797–818, 1999.

[10] W. Voigt, *Lehrbuch der Kristallphysik*. Teubner, 1910.

[11] B. Jaffe, W. Cook, and H. Jaffe, *Piezoelectric Ceramics*. Academic Press, 1971.

[12] K. Cook-Chennault, N. Thambi, and A. Sastry, "Powering MEMS portable devices," *Smart Materials and Structures*, vol. 17, p. 043 001, 2008.

[13] M. Vijaya, *Piezoelectric Materials and Devices*. CRC Press, 2012.

[14] E. Lefeuvre, M. Lallarrt, C. Richard, and D. Guyomar, "Piezoelectric ceramics," in, E. Gmez, Ed. Sciyo, 2010, ch. Piezoelectric Material-Based Energy Harvesting Devices: Advances of SSH Optimization Techniques (1999-2000).

[15] S. Sherrit and B. Mulkherjee, "Characterization of piezoelectric materials for transducers," *Dielectric and Ferroelectric Reviews*, 2007.

[16] *Dynamic behavior: Oscillation modes of piezoceramic elements*, Web.

[17] S. Butterworth, "On electrically maintained vibrations," *Proceedings of the Physical Society*, vol. 27, pp. 410–24, 1915.

[18] K. Cook-Chennault and N. Thami, "Powering mems portable devices: A review of non-regenerative and regenerative power supply systems with special emphasis on piezoelectric energy, harvesting systems.," *Smart Materials and Structures*, 2008.

[19] *IEEE standard on piezoelectricity*, New York: IEEE, 1987.

[20] R. Xu and S. Kim, "Figures of merit of piezoelectric materials in energy harvesters," in *PowerMEMS*, 2012.

[21] C. de Silva, *Sensors and Actuators: Engineering System Instrumentation*. CRC Press, 2015.

[22] T. Hehn and Y. Manoli, "Cmos circuits for piezoelectric energy harvesters," in. Springer, 2014, ch. Piezoelectricity and Energy Harvester Modelling, pp. 21–40.

[23] M. Pozzi, "Analytical modelling of a plucked piezoelectric bimorph for energy harvesting," *Classical Physics*, 2012.

[24] Y. Sugawara, K. Onitsuka, S. Yoshikawa, Q. Xu, R. Newnham, and K. Uchino, "Metal-ceramic composite actuators," *Journal of American Ceramic Society*, vol. 75, no. 4, pp. 996–98, 1992.

[25] H. Priya and S. Inman, *Energy Harvesting Technologies*. Springer, 2009, ISBN: 978-0-387-76464-1.

[26] N. Shenck and J. Paradiso, "Energy scavenging with shoe-mounted piezoelectrics," *IEEE Micro*, vol. 21, pp. 30–42, 2001.

[27] J. Rocha, L. Gocalves, P. Rocha, and S. Silva, "Energy harvesting from piezoelectric materials fully integrated in footware," *IEEE Trasducers Industry Electronics*, vol. 57, pp. 813–820, 2010.

[28] L. Moro and D. Benasciutti, "Harvested power and sensitivity analysis of vibrating shoe-mounted piezoelectric cantilevers," *Smart Materials Structures*, vol. 19, p. 115 011, 2010.

[29] N. Sharpes, D. Vuckovic, and S. Priya, "Floor tile energy harvester for self-powered wireless occupancy sensing," *Energy Harvesting and Systems*, vol. 3, pp. 43–60, 1 2015.

[30] M. Umeda, K. Nakamura, and S. Ueha, "Analysis of the transformation of mechanical impact energy to electric energy using piezoelectric vibrator," *Japanese Journal of Applied Physics*, vol. 35, pp. 3267–73, 1996.

[31] M. Pozzi and M. Zhu, "Plucked piezoelectric bimorphs for knee-joint energy harvesting: Modelling and experimental validation," *Smart Materials and Structures*, vol. 20, p. 055 007, 2011.

[32] B. Yang and K. Yun, "Piezoelectric shell structures as wearable energy harvesters for effective power generation at low-frequency movement," *Sensors and Actuators*, 2012.

[33] *Programmer's manual for mechanical APDL release 12.0*, ANSYS, Inc., Canonsburg, PA, 2016.

[34] D. Berlincourt and H. Kruger, "Technical publication TP-226 properties of piezoelectricity," Morgan Electroceramics, Tech. Rep., 2000.

[35] K. Uchion, *Introduction to Piezoelectric Actuators and Transducers*. Defense Technical Information Center, 2003.

[36] Y. Kuang and M. Zhu, "Design study of a mechanically plucked piezoelectric harvester using validated finite element modelling," *Sensors and Actuators A: Physical*, 2017.

[37] H. Shekhani and U. K., "Evaluation of the mechanical quality factor under high power conditions in piezoelectric ceramics from electrical power," *Journal of the European Ceramic Society*, 2014.

[38] W. Wong and A. Salleo, *Flexible Electronics*. Springer, 2009, ISBN: 978-0-387-74362-2.

[39] K. Ray, "Flexible solar cell arrays for increased space power," *IEEE Transactions on Aerospace and Electronic Systems*, vol. AES-3, no. 1, pp. 107–115, Jan. 1967.

[40] R. Rocheleau, P. Lutz, D. Brestovansky, B. Baron, and T. Russell, "Continuous deposition of photovolatic grade CdS sheet at the unit operations scale," in *Proceedings*

of the Fourth International Conference in Photovolatic Solar Energy, Stresa, Italy, May 1982.

[41] P. Nath and M. Izu, "Performance of large area amorphous Si based single and multiple junction solar cells," in *18th Photovoltaic Specialists Conference*, Las Vegas, NV, Oct. 1985.

[42] I. French, D. McCulloch, I. Boerefijn, and N. Kooyman, "Thin plastic electrophoretic displays fabricated by a novel process," *Society for Information Display*, vol. 36, no. 1, pp. 1634–1637, May 2005.

[43] R. Kwong, M. Hack, T. Zhou, J. Brown, and T. Ngo, *Highly stable and efficient OLEDs with a phosphorescent-doped mixed layer architecture*, Patent, Oct. 2004.

[44] D. Kim, H. Park, and S. Yoon, *Quantum dot sheet and light unit and liquid crystal display including the same*, US Patent 9,581,759, 2017.

[45] *Lg display to build world's first 5th generation OLED light panel plant*, Web, 2016.

[46] G. Giordano, "Active packing gets smarter," *Plastics Engineering*, 2015.

[47] T. De Chant, "In ten years, you wont even know youre wearing them," *NovaNext*, 2014.

[48] L. Diggelmann, *Lg produziert flexible displays*, Web, 2013.

[49] M. Koyuncu, E. Lorenz, and A. Zimmermann, "Handbook of flexible organic electronics," in. Woodhead Publishing, 2015, ch. Advanced Interconnection Technologies for Flexible Organic Electronic Systems, pp. 143 –169.

[50] J. Burghartz, *Ultra-thin Chip Technology and Applications*. Springer, 2011.

[51] J. W. Gardner, V. K. Varadan, and O. O. Awadelkarim, *Microsensors, MEMS, and Smart Devices*. John Wiley & Sons, Nov. 2013.

[52] V. Kaajakari, *Practical MEMS: Design of Microsystems, Accelerometers, Gyroscopes, RF MEMS, Optical MEMS, and Microfluidic Systems*. Small Gear, Mar. 2009, ISBN: 0982299109.

[53] H. Baltes, O. Brand, G. Feder, C. Hierold, J. Korvink, and O. Tabata, *CMOS-MEMS*. Wiley, 2013.

[54] A. Fischer, F. Forsberg, M. Lapisa, S. Bleiker, G. Stemme, N. Roxhed, and F. Niklaus, "Integrating MEMS and IC," *Microsystems and Nanoengineering*, vol. 1, no. 15005, 2015.

[55] *BMI160 data sheet*, Web, Feb. 2015.

[56] C. Nagel, F. Ante, M. Mahlich, and J. Mehner, "Flexible electronics: Requirements and challenges for MEMS," in *Be-Flexible Forum Mnchen*, 2016.

[57] N. Yazdi, F. Yazdi, and K. Najafi, "Mircomachined inertial sensors," in *Proceedings of the IEEE*, vol. 86, Aug. 1998, pp. 1640–1659.

[58] L. Song, "Sensortec technology: Accelerometer working principle," Bosch Sensortec, Internal Report, 2016.

[59] *Heterogenous components*, 2015.

[60] Y. Li, D. Lu, and C. Wong, *Electrical Conductive Adhesives with Nanotechnologies*. Springer, 2010.

[61] K. S.C. and K. Y.H., "Review paper: Flip chip bonding with anisotropic conductive film (ACF) and nonconductive adhesive (NCA)," *Current Applied Physics*, vol. 13, S14–S25, Jul. 2013.

[62] L. Frisk and E. Ristolainen, "Flip chip attachment on flexible LCP substrate using an ACF," *Microelectronics Reliability*, Dec. 2004.

[63] J. Liu, O. Salmela, J. Sarkka, J. Morris, P. Tegehall, and C. Andersson, *Reliability of Microtechnology: Interconnects, Devices and Systems*. Springer, 2011.

[64] G. R. and M. K.L., *Electrically Conductive Adhesives*. CRC Press, 2008.

[65] S. Logothetidis, *Handbook of Flexible Organic Electronics*, 68. Woodhead Publishing, Jan. 2015.

[66] Y. Xu, Y. Tai, A. Huang, and C. Ho, "IC-integrated flexible shear-stress sensor skin," *Journal of Microelectromechanical Systems*, vol. 12, no. 5, pp. 740–747, Oct. 2003.

[67] I. Gonenli, Z. Celik-Butler, and D. Bulter, "Surface micromachined MEMS accelerometers on flexible polyimide substrate," *IEEE Sensors Journal*, vol. 11, no. 10, pp. 2318–2326, Oct. 2011.

[68] N. Lee, *Reflow Soldering Processes and Troubleshooting*. Elsevier, 2002.

[69] D. Butler and C.-B. Z., "Encyclopedia of nanotechnology," in. Springer, 2012, ch. MEMS on Flexible Substrates, pp. 1343 –1351.

[70] S. Dayeh, Z. Celik-Butler, and D. Bulter, "Micromachined infrared bolometers on flexible polyimide substrates," *Sensors and Actuators*, pp. 49–56, 2005.

[71] A. Mahmood, D. Bulter, and Z. Celik-Butler, "Device-level vacuum-packaging scheme for microbolometers on rigid and flexible substrates," *IEEE Sensors*, vol. 7, pp. 1012–1019, 2007.

[72] M. Ahmed, I. Gonenli, G. Nadvi, R. Kilaru, D. Butler, and Z. Celik-Butler, "MEMS sensors on flexible substrates towards a smart skin," in *IEEE Sensors*, IEEE, Oct. 2012.

[73] D. Briand, F. Molina-Lopez, A. Quintero, C. Ataman, J. Courbat, and N. F. de Rooij, "Why going towards plastic and flexible sensors?" In *Eurosensors XXV*, Athens, Greece: Elsevier, Sep. 2011.

[74] Y. Wei, R. Torah, K. Yang, S. Beeby, and J. Tudor, "Screen printing of a capacitive cantilever-based motion sensor on fabric using a novel sacrificial layer process for smart fabric applications," *Measurement Science and Technology*, vol. 5, no. 7, p. 075 104, Jun. 2013.

[75] U. Altenberend, D. Molina-Lopez F.a nd Briand, A. Oprea, N. Barsan, N. De Rooij, and U. Weimar, "Inkjet printed capacitive transducers on flexible plastic substrates with increase stability: Ag on PET," in *The 14th International Meeting on Chemical Sensors*, 2012.

[76] F. Molina-Lopez, D. Brian, and N. de Rooij, "Large arrays of inkjet-printed MEMS microbridges on foil," in *MEMS*, IEEE, Jan. 2014.

[77] J. Burghartz, "Ultra-thin Si chips for flexible electronics: Technology, characterization, assembly and applications," in *2013 Symposium on Microelectronics Technology and Devices (SBMicro)*, 2013.

[78] G. Lippold, "Schliffe an flexboards bestckt mit BMI160," RoodMicrotec, Tech. Rep., 2017.

[79] J. Balde, *Foldable Flex and Thinned Silicon Multichip Packaging Technology*. Springer, 2013.

[80] *Standard test method for peel resistance of adhesives (T-peel test)*, ASTM.

[81] *Ansys advanced analysis guide*, 5.5, ANSYS, Inc.

[82] A. Abawi, "The bending of bonded layers due to thermal stress," *HLS Research*, 2004.

[83] H. K. Charles, "Advanced wire bonding technology: Materials, methods, and testing," in *Materials for Advanced Packaging*, D. Lu and C. Wong, Eds. Boston, MA: Springer US, 2009, pp. 113–179, ISBN: 978-0-387-78219-5.

[84] B. Ratner, S. Hoffman, F. Schoen, and J. Lemons, *Biomaterials Science: An Introduction to Materials in Medicine*. Academic Press, 2012.

[85] J. Lintz, "Thermomechanische stresssimulation zur optimierung der aufbau- und verbindungstechnik von inertialsensoren auf foliensubstraten," Master's thesis, University of Stuttgart, 2016.